



VACUUM DEPOSITION OF ORGANIC MOLECULES FOR PHOTOVOLTAIC APPLICATIONS

Peter Kovacik

Oriel College

A thesis submitted for the degree of DPhil in Materials

University of Oxford

ABSTRACT

The vacuum thermal evaporation of conjugated polymers is presented and their application in organic photovoltaic devices studied.

Poly(3-hexylthiophene) (P3HT) and poly(thiophene) (PTh), semiconducting polymers with and without side groups, are deposited by vacuum thermal evaporation. Thermal behaviour of the polymers is studied using DSC and TGA, and the structural changes before and after evaporation investigated by GPC, UV-Vis, NMR, and FT-IR. These studies show that the polymers largely retain their chemical structure, however, their molecular weight decreases. The inferred conjugation length of the evaporated PTh is larger than that of P3HT, as indicated by GPC. Finally, the topography of the polymer thin films is compared using MicroXAM and AFM, and their morphology analysed by TEM and XRD. In contrast to P3HT, evaporated PTh forms microscopically flat films with high molecular order.

Functional photovoltaic devices based on vacuum-deposited PTh and P3HT are presented. Different processing and device parameters are examined, and the influence side groups have on the electronic properties of the thin films is studied. Unlike P3HT, the greater crystallinity in PTh films results in significantly improved charge transport properties with relatively high hole mobilities ($10^{-4} \text{ cm}^2\text{V}^{-1}\text{s}^{-1}$). PTh/ C_{60} planar heterojunction devices exhibit an almost 70% increase in efficiency compared to P3HT/ C_{60} devices, demonstrating enhanced charge extraction in PTh films through improved molecular order. The photovoltaic performance is further related to morphology and optical absorption of the polymer thin films using MicroXAM and UV-Vis. The effect of incident illumination intensity

and post-production thermal annealing is investigated, complementing the detailed characterisation of the devices.

Co-deposited bulk heterojunctions with different PTh:C₆₀ volume ratios are fabricated and their response to post-production thermal annealing examined. Blend morphology is characterised by AFM and XRD and related to the photovoltaic performance. Post-annealing is shown to improve the interpenetrated polymer-fullerene network and enhance efficiency by as much as 80%. Moreover, the development of the PTh:C₆₀ blend morphology is found to be different from standard small-molecule systems. This is illustrated by comparing the morphology of the polymeric PTh:C₆₀ and oligomeric 6T:C₆₀ blends. Finally, a device architecture consisting of multiple alternating PTh/C₆₀ thin films is presented with performance exceeding that of its equivalent co-deposited bulk heterojunction.

ACKNOWLEDGEMENTS

I thank the Engineering and Physical Sciences Research Council and the John Fell Oxford University Press Research Fund for financially supporting my education at Oxford. I am grateful to Oriel College for providing me with a firm social base and repeatedly funding my conference travels. I also thank the Department of Materials for its financial generosity.

I thank Dr Andrew Watt for his guidance. I am grateful for our many stimulating debates, and for his enduring patience, his dependability, and particularly his targeted advice on research & life. I did follow most of it. I also believe my research is more punchy and sexy now.

I thank Dr Hazel Assender for her supervision. I am grateful for her fast and clever feedback, systematic approach, cooling but sober opinions, support, and encouragement. I want to believe my research is more accurate and truthful now.

I thank my officemates, Dr Shawn Willis for letting me have the desk with the only window in our office, for illustrating professionalism in all projects we have undertaken together, and of course for setting up high-productivity standards worth following; and Laura Droessler for taping yellow sunflowers on our walls. I think all our characters blended well on our postcard board.

I thank my lovely colleagues, Elva Zou for making the lab environment eccentric, Simon Fairclough friendly, Jenna Holder fairy, and Chris Cattley British. I thank Cheng Cheng for his drive towards endless lab improvements, for being a faithful co-experimentalist, and for cooperatively bouncing and shaping an infinite number of research ideas.

I thank Dr Gamal Abbas, Dr Andrew Cook, Dr Jonathan Moghal, Ziqian Ding, and Long Jiang for invaluable discussions, suggestions, and comments. I thank Dr Richard Beal and Dr Alexandros Stavrinnadis for demonstrating that even finishing postgraduates can be helpful

and nice. I thank all part two and summer students, Daniel Camp, Maria Nelson, Assia Kasdi, Miriam Hoener, Tom Walton, Lou Yeoh, Brienne Kugler, Simon Bowcock, Shek Li, and Kayla Nguyen, for making many bits of my DPhil time joyful.

I thank Dr John Topping for introducing me to the world of vacuum and for many, many inspiring and educational discussions. I thank Richard Turner for all his help with measurements and technical issues, Gabriella Chapman and Sverre Myhra for training me on microscopes, and Laurie Walton for help with fabricating the equipment. I thank Marion Beckett, Adrian Taylor, Lyn Richmond, Barry Fellows, Ian Sutton, and Paul Warren for various forms of assistance.

I thank Prof Harry Anderson, Dr Giuseppe Sforazzini, and Dr Jonathan Matichak, great organic chemists, for fruitful inter-departmental collaborations.

I thank my closest ones who turned my “outlab” life at Oxford into 51% of my overall growth.

Finally, I thank my family for their support and love. This work, which none of you will probably read, is unsurprisingly dedicated to you.

DECLARATION OF ORIGINALITY

This thesis is an account of work carried out by the author in the Materials Department, University of Oxford under the supervision of Dr Hazel Assender and Dr Andrew Watt. Where the work of others has been drawn upon this is duly acknowledged in the text, and a list of references is presented at the end of each chapter. No part of this thesis has been submitted towards the completion of another degree at the University of Oxford or elsewhere. Parts of this thesis have been submitted to or published in the following scientific journals or conference presentations:

Journal articles

Kovacik, P.; Sforazzini, G.; Cook, A. G.; Willis, S. M.; Grant, P. S.; Assender, H. E.; Watt, A. A. R., Vacuum-Deposited Planar Heterojunction Polymer Solar Cells. *ACS Applied Materials & Interfaces* **2011**, 3, (1), 11-15.

Kovacik, P.; Willis, S. M.; Matichak, J. D.; Assender, H. E.; Watt, A. A. R., Effect of Side Groups on the Vacuum Thermal Evaporation of Polythiophenes for Organic Electronics. *Organic Electronics* **2012**, 13, (4), 687-696.

Kovacik, P.; Assender, H. E.; Watt, A. A. R., Morphology Control in Co-evaporated Bulk Heterojunction Solar Cells. *Journal of Physical Chemistry C* **2012**, submitted.

Kovacik, P.; Assender, H. E.; Watt, A. A. R., Importance of Oligothiophene Conjugation Length in Phase-Separated Vacuum-Deposited Heterojunction Blends. **2012**, in preparation.

Kovacik, P.; Assender, H. E.; Watt, A. A. R., Enhancement of Charge Extraction in Polymer Bulk Heterojunctions through Alternating Thermal Deposition. **2012**, in preparation.

Conference proceedings

Kovacik, P.; Willis, S. M.; Sforazzini, G.; Assender, H. E.; Watt, A. A. R. In *Vacuum Deposition of Conjugated Polymers for Solar Cells*, 7th Photovoltaic Science Application and

Technology (PVSAT-7) Conference and Exhibition, Edinburgh, United Kingdom, 2011; Edinburgh, United Kingdom, 2011.

Kovacik, P.; Assender, H. E.; Watt, A. A. R. In *Vacuum Deposition of Conjugated Polymers for Organic Photovoltaics*, 55th Annual SVC Technical Conference, Santa Clara, USA, 2012; Society of Vacuum Coaters Santa Clara, USA, 2012.

Conference papers

Kovacik, P.; Sforazzini, G.; Assender, H. E.; Watt, A. A. R., Thermal Deposition of Large Organic Molecules for Photovoltaic Applications. In *2009 MRS Fall Meeting*, Boston, USA, 2009.

Kovacik, P.; Sforazzini, G.; Willis, S. M.; Assender, H. E.; Watt, A. A. R., Thermal Deposition of Large Organic Molecules for Photovoltaic Applications. In *UK Semiconductors 2010*, Sheffield, United Kingdom, 2010.

Kovacik, P.; Sforazzini, G.; Willis, S. M.; Assender, H. E.; Watt, A. A. R., Vacuum-Deposited Polythiophene Organic Solar Cells. In *ElecMol 2010, 5th International Meeting on Molecular Electronics*, Grenoble, France, 2010.

Kovacik, P.; Willis, S. M.; Matichak, J. D.; Sforazzini, G.; Assender, H. E.; Watt, A. A. R., Vacuum Deposition of Conjugated Polymers for Solar Cells. In *7th Photovoltaic Science Application and Technology (PVSAT-7) Conference and Exhibition*, Edinburgh, United Kingdom, 2011.

Kovacik, P.; Willis, S. M.; Assender, H. E.; Watt, A. A. R., Vacuum-Deposited Polythiophene Organic Solar Cells. In *IOP Advances in Photovoltaics*, London, United Kingdom, 2011.

Kovacik, P.; Matichak, J. D.; Willis, S. M.; Assender, H. E.; Watt, A. A. R., Vacuum Deposition of Conjugated Polymers for Organic Photovoltaics In *IOP Physical Aspects of Polymer Science*, Guildford, United Kingdom, 2011.

Kovacik, P.; Assender, H. E.; Watt, A. A. R., Vacuum-Deposited Polythiophene Organic Solar Cells. In *2012 MRS Spring Meeting*, San Francisco, USA, 2012.

Kovacik, P.; Assender, H. E.; Watt, A. A. R., Vacuum Deposition of Conjugated Polymers for Organic Photovoltaics. In *55th Annual SVC Technical Conference*, Santa Clara, USA, 2012.

TABLE OF CONTENTS

Abstract	i
Acknowledgements.....	iii
Declaration of Originality.....	v
Table of Contents	vii
List of Abbreviations.....	ix
Chapter 1 - Theoretical Review	1
1.1 Introduction.....	1
1.1.1 Motivation.....	1
1.1.2 Energy status-quo.....	2
1.1.3 Organic solar cells.....	3
1.2 Theory and realisation of solar cells.....	5
1.2.1 Organic semiconductors.....	5
1.2.2 Power generation	7
1.2.3 Band structure.....	10
1.2.4 Performance analysis	13
1.2.5 Device architectures and performance improvements	16
1.3 Organic materials for solar cells	18
1.3.1 Low molecular weight materials	18
1.3.2 High molecular weight materials.....	22
1.4 Deposition techniques.....	25
1.4.1 Laboratory vs. industrial processing.....	25
1.4.2 Vacuum deposition.....	27
1.4.3 Coating and printing techniques	33
1.5 References	34
Chapter 2 - Materials and Methods.....	43
2.1 Materials.....	43
2.2 Polymer evaporation	44
2.3 Polymer characterisation	46
2.4 Thin-film characterisation	49
2.5 Photovoltaic device fabrication.....	52
2.6 Photovoltaic device characterisation	54
2.7 References	55

Chapter 3 - Vacuum Thermal Deposition of Conjugated Polymers	57
3.1 Introduction	57
3.2 Thermal behaviour and vacuum deposition of P3HT	59
3.3 Thermal behaviour and vacuum deposition of PTh.....	66
3.4 Topography of P3HT and PTh thin films.....	71
3.5 Structural analysis of P3HT and PTh thin films	76
3.6 Conclusion	79
3.7 References.....	80
Chapter 4 - Planar Heterojunction Photovoltaic Devices.....	83
4.1 Introduction	83
4.2 Electronic properties of PTh and P3HT thin films	85
4.3 Polymer/Al Schottky photovoltaic devices	88
4.4 Polymer/fullerene planar heterojunction solar cells	89
4.5 Thickness-optimisation of planar heterojunction solar cells.....	93
4.6 Optical and morphological properties of planar heterojunction solar cells	97
4.7 Effect of illumination intensity on planar heterojunction solar cells	99
4.8 Effect of thermal annealing in planar heterojunction solar cells.....	102
4.9 Conclusion	104
4.10 References.....	105
Chapter 5 - Bulk Heterojunction Photovoltaic Devices.....	109
5.1 Introduction	109
5.2 Optimisation of annealing parameters in PTh:C ₆₀ blends.....	111
5.3 Effect of thermal annealing on different PTh:C ₆₀ blend compositions.....	113
5.4 Effect of thermal annealing on charge extraction processes	117
5.5 Development of morphology in annealed PTh:C ₆₀ blends	120
5.6 Morphological comparison of polymer and oligomer BHJs.....	124
5.7 Multiple-layer BHJs as an equivalent to co-deposited BHJs	129
5.8 Conclusions	131
5.9 References.....	131
Conclusions	135
Future Work	139

LIST OF ABBREVIATIONS

^1H	Hydrogen-1 (proton)
6T	Sexithiophene
AFM	Atomic force microscopy
Ag	Silver
AHJ	Alternating heterojunction
Al	Aluminium
AM 1.5	Air mass 1.5 coefficient
Ar	Argon
Au	Gold
BCP	Bathocuproine (2,9-Dimethyl-4,7-diphenyl-1,10-phenanthroline)
BHJ	Bulk heterojunction
C_{60}	Fullerene (buckminsterfullerene)
C_{70}	Fullerene molecule consisting of 70 carbon atoms
CuPc	Copper phthalocyanine
CVD	Chemical vapour deposition
D-A	Donor-acceptor
DC	Direct current
DSC	Differential scanning calorimetry
DTA	Differential thermal analysis
E_g	Electrical band gap energy
EL	Electroluminescence
EQE	External quantum efficiency
FF	Fill factor
FT-IR	Fourier transform infrared spectroscopy
GPC	Gel permeation chromatography
H_2O	Water
HOMO	Highest occupied molecular orbit
IQE	Internal quantum efficiency
$I-V$	Current-voltage
I_{sc}	Short circuit current
I_0	Reverse saturation current
IR	Infrared
ITO	Indium tin oxide
$J-V$	Current density-voltage
J_{sc}	Short circuit current density
LiF	Lithium fluoride
LUMO	Lowest unoccupied molecular orbit
μ_p	Hole mobility
Mg	Magnesium
MicroXAM	Phase-shift interferometric optical profilometry
M_p	Peak molecular weight
M_w	Molecular weight (weight average)

<i>n</i>	Ideality factor
NMR	Nuclear magnetic resonance spectroscopy
N₂	Nitrogen
ND	Neutral density
O₂	Oxygen
OFET	Organic field-effect transistor
OLED	Organic light emitting diode
OPV	Organic photovoltaics
OVPD	Organic vapour phase deposition
<i>P</i>₀	Incident light intensity
P3AT	Poly(3-alkylthiophene)
P3HT	Poly(3-hexylthiophene-2,5-diyl)
PCBM	[6,6]-Phenyl-C61 butyric acid methyl ester
PCDTBT	Poly[N-9''-hepta-decanyl-2,7-carbazole-alt-5,5-(4',7'-di-2-thienyl-2',1',3'-benzothiadiazole)]
PCE	Power conversion efficiency
PEDOT:PSS	Poly(3,4-ethylenedioxythiophene) poly(styrenesulfonate)
PHJ	Planar heterojunction
PL	Photoluminescence
PPP	Poly(p-phenylene)
PTh	Poly(thiophene)
PTh/C₆₀	Poly(thiophene)/fullerene planar heterojunction
PTh:C₆₀	Poly(thiophene)/fullerene bulk heterojunction
PV	Photovoltaic
PVK	Poly(N-vinylcarbazole)
R2R	Roll-to-roll
RMS	Root mean square
<i>R</i>_s	Series resistance
<i>R</i>_{sh}	Shunt (parallel) resistance
SCLC	Space charge limited current
Si	Silicon
<i>T</i>_e	Evaporation temperature
TEM	Transmission electron microscopy
THF	Tetrahydrofuran
<i>T</i>_g	Glass transition temperature
TGA	Thermogravimetric Analysis
<i>T</i>_m	Melting temperature
UV	Ultraviolet
Vis	Visible
<i>V</i>_{BI}	Built-in voltage
<i>V</i>_{oc}	Open circuit voltage
VTE	Vacuum thermal evaporation
XRD	X-ray diffraction
ZnPc	Zinc phthalocyanine

CHAPTER 1 - THEORETICAL REVIEW

1.1 Introduction

1.1.1 Motivation

Electronic products based on organic thin film semiconductors have a plethora of applications which take advantage of the mechanical flexibility and the ability to manufacture on a large scale at low cost. This has allowed technologies such as OFET (organic field-effect transistors), OLED (organic light emitting diodes) and OPV (organic photovoltaic cells) to become promising candidates for the next generation electronics.

Organic semiconductors used in solar cells fall into two main groups - low molecular weight 'molecular' materials which are usually vacuum deposited, and higher molecular weight polymers which are usually solution processed. Polymer photovoltaics take advantage of the efficient light absorption, good charge transport properties and preferable response to morphological control during or after deposition. Although some insulating polymers have been commonly deposited by physical vapour deposition techniques, there have been only a few attempts to deposit semiconductive polymers in the same way.

The review introduces context of the solar energy and fundamental principles under which the photovoltaic modules operate. The factors influencing the power conversion are discussed followed by an evaluation of organic materials and device architectures

commonly used. Finally, the deposition techniques are summarised with emphasis on their large-scale capabilities.

1.1.2 Energy status-quo

Energy remains one of the most essential components of our society. Its generation, distribution and consumption determines the quality of everyday life in the 21st century¹. In particular, the impact of energy generation on *environment* needs to be considered as it has a potential to affect the stability of our climate. The annual world's energy consumption is approximately 500 EJ/yr (equivalent to an average consumption of 15 TW) and is projected to grow by more than 50% over the next three decades. About 30 billion metric tons carbon equivalent of *greenhouse gas emission* are released in the atmosphere to meet this demand. This is largely due to 81% of the generated energy being of fossil origin². Increasingly limited access to fossil fuels is imposing still higher costs on energy generation which in turn affects political and economic stability of countries.

Renewable energy systems such as solar power, wind power, hydropower, biomass or geothermal power, represent a way of extracting energy from abundant and sustainable sources³. They account for about 16% of the world's energy and close to 20% of the world's electricity generation⁴. Of this, more than 80% of the electricity generation is attributed to hydropower. There has been a rapid growth in the global renewable energy market in the last few years, with renewables representing about 25% of added power generation capacity in USA and China, and more than 40% in Europe⁴.

In comparison to any other sources, *solar energy* is by far the most abundant one. The Earth's surface receives annually almost 4 million EJ of energy, which is a power exceeding our current rate of consumption by 10 000 times³. Solar heating, solar thermal electricity and solar photovoltaics (PV) are the main technologies for direct conversion of the sunlight into heat and electricity. However, *photovoltaics* stands out as the most technologically elegant and thus very attractive⁵. Grid-connected solar PV have been recently the fastest growing power generation technology with the average annual growth rate exceeding 60% over the 2005-2010 five-year period². The PV market has been driven mainly by falling production costs, new applications and stronger policy support.

1.1.3 Organic solar cells

The development of solar cells has largely focused on *silicon technologies* (predominantly monocrystalline silicon) which have become a mature and suitable option for many applications. Unfortunately, complicated manufacturing process and high price has limited their production and deep energy-market penetration⁶. Introduction of polycrystalline and amorphous silicon has reduced the costs, however, on account of lower power conversion efficiency.

Multijunction photovoltaics based on GaInAs (gallium indium arsenide) are one alternative to silicon technology. By utilising complex device architectures and extreme light concentration, high efficiencies (>40%) can be reached⁷. Nevertheless, scarcity of materials (e.g. indium) and high processing costs question their wider application. Another alternative, thin-film photovoltaics were the first to lower the manufacturing costs below US 1\$/W⁸. Recent intensive development of CdTe (cadmium telluride) and CIGS (copper,

indium, gallium, selenium) solar cells has rapidly increased their competitiveness as a low-cost technology and lead to large-scale utilisation⁹.

Efficient or feasible conversion of solar energy into electricity is not the only necessity to make a technology attractive. For example, high specific power (the power per mass of a module or array) is essential for portable as well as many standard static power needs⁶. This can severely limit photovoltaics made on bulk and massive substrates. Modules which are light and flexible would often be advantageous as they could be moulded onto non-rigid or non-uniform surfaces¹⁰. Such electronic systems would allow diversification of applications and better integration of the technology in everyday life¹¹.

Organic electronics have significant potential to match these ambitions. Organic semiconductor materials can be deposited on flexible substrates using low-cost processing techniques, such as roll-to-roll solution printing or vacuum deposition^{12, 13}. Moreover, manufacturing technology for flexible electronics is already established in the OLED industry where the fundamental issues, including molecular design, thin-film deposition or device encapsulation, have already been confronted¹⁴. This has helped the organic photovoltaics to make the first steps not only in the laboratory but also industrial environment.

The certified power conversion efficiency of state-of-the-art organic solar cells has already exceeded 10%^{7, 15}. The performance has almost doubled over the past 5 years and is now approaching other competitive thin-film technologies (such as amorphous silicon and dye-sensitised photovoltaics). Moreover, stability measurements of the encapsulated devices have shown promising extrapolated lifetimes of almost 7 years¹⁶. Following manufacturing trials the large-scale production facilities were introduced in past by Konarka¹⁷ and recently

by Heliatek GmbH¹⁸. Organic photovoltaics have successfully illustrated their unique potential and with continuous improvements in performance and reduction in processing costs they are on the way to fulfil their promise to harness the vast energy from the Sun.

1.2 Theory and realisation of solar cells

1.2.1 Organic semiconductors

The electronic properties of organic molecules depend on *bonds* between the atoms. The character and position of these inter-atomic bonds define the way molecule absorbs light and transports charge. Central to this are the double bonds and the way they are joined together within the molecule (i.e. way they are conjugated). Systems with alternating single and double bonds are known as *conjugated*¹⁹, meaning that the electrons in the bonds are able to delocalise along a segment of the molecule.

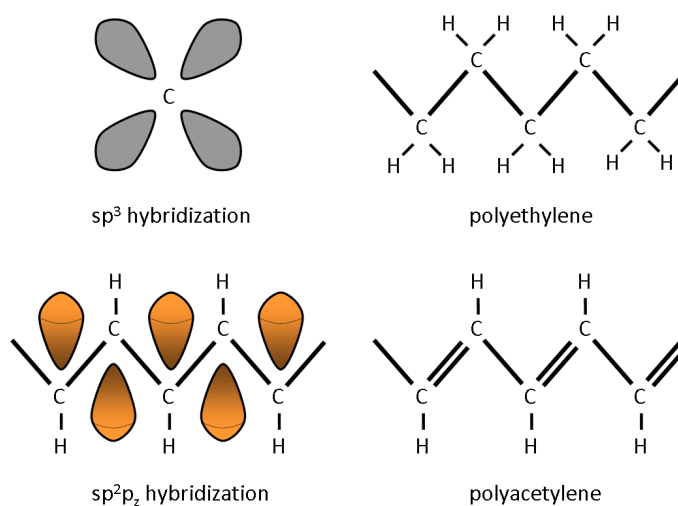


Figure 1. Electronic and molecular structure of (top) polyethylene and (bottom) polyacetylene.

In non-conductive molecules (e.g. polyethylene shown in Figure 1), each carbon atom is bound to four other atoms by σ bonds. All its electrons are used for bonding, having their orbitals hybridised in sp^3 configuration. The chemical bonds are fully saturated and the valence band is empty because there are no free electrons in the molecule to conduct. Hence, saturated molecules are insulators which do not conduct²⁰. By contrast, conjugated molecules contain unsaturated bonds (e.g. polyacetylene shown in Figure 1) with one unpaired electron per carbon atom. Electronic orbitals are in sp^2p_z configuration - three σ -bonding electrons forming sp^2 orbitals and one π electron forming a p_z orbital usually perpendicular to the plane of the molecule. As p_z orbitals of the adjacent atoms overlap, delocalised π electrons create together a π bond. This bond is a pair of electron clouds spread on each side of the molecular plane²¹, i.e. two molecular orbitals resulting from a combination of two atomic orbitals. These are either in-phase or out-of-phase, the former creates bonding molecular orbital π and the latter anti-bonding orbital π^* .

In larger molecules, such as *polymers*, the delocalised π bonds extend over the length of the *conjugated backbone* and form π bands. Conductive and semiconductive properties of the molecule then depend on whether the bands are filled or partially filled. The number of π bands is determined by the number of carbon atoms in the elementary unit. Their position has also a direct influence on the molecular *band-gap*. As such, it is defined as the energy difference (π - π^*) between the highest occupied π sub-band and the lowest unoccupied π^* sub-band²⁰. The energy band-gap, as well as many other physical properties (e.g. conductivity or solubility) can be modified by changing the structure of the molecule.

Impurities in organic materials often disrupt molecular stacking order and act as traps and recombination sites for charge carriers²². This can reduce charge carrier mobility of the

material. Most common impurities in conjugated systems come from the environment. Oxygen and water molecules cause degradation of organic semiconductors and thus severely limit their functional lifetimes. Protection from air and moisture is therefore essential for stable operation and further application.

1.2.2 Power generation

The bonding in organic semiconductors fundamentally differs from their inorganic counterparts. While the former are held together by weak van der Waals bonds and have quasi-isolated character, stronger covalent bonds dominate in the latter case. This has a direct influence on the properties of organic materials (e.g. decreased hardness, lower melting point, reduced charge carrier transport²²). The poor mobilities are, however, to some degree compensated by high absorption coefficients (usually $\geq 10^5 \text{ cm}^{-1}$) allowing materials to effectively absorb light even at thicknesses less than 100 nm²³.

The weak *electronic delocalisation* gives organic semiconductors two distinct features – the existence of singlet and triplet spin states, as found in isolated molecules, and formation of *excitons*, photo-excited bound states of an electron and a hole. Excitons arise from the interaction of light with the photoactive conjugated molecule. An incoming photon excites a valence electron to a higher energy state and forms a Coulomb-attracted electron-hole pair. The energy of the photon must be equal or higher than the material's band-gap. The excitonic pair is charge-neutral and is usually localised on one molecule (thus having a substantial binding energy, typically 0.5 to 1 eV²²). In order to separate a positive and a negative charge and thus deliver a current, this binding energy has to be overcome by an external field. Formation and dissociation of excitons are among the main processes

occurring in organic solar cells. For this reason, the devices are often referred to as excitonic solar cells.

Excitonic lifetime is indirectly defined by its *diffusion length* (L_D) – a distance, through which an exciton migrates along the structure before it recombines. The diffusion length is usually very short in organic materials (on the order of 1-10 nm²⁴). As with the charge conduction, it largely depends both on structural (inhomogeneities, impurities, differences in materials) and dielectric qualities of the environment.

Dissociation of excitons into free charges is a fundamental step in converting energy of photons into electricity. This can be achieved by an applied electric field. The potential difference between the standard cathode and the anode materials is, however, not sufficient to break up the electron-hole Coulomb attraction. Instead, the exciton migrates to the material/electrode interface where it is dissociated. Often it recombines on the way due to its short diffusion length (excitonic recombination is called *geminate*, monomolecular or trap-assisted recombination²⁵). If there is a contact of two materials, of which one has a sufficiently higher electron affinity and ionisation potential (acceptor) than the other (donor), the electrical field of such interface allows the dissociation²⁶. This happens only when the energy difference is bigger than the exciton binding energy. The interfacial design of the donor and acceptor materials therefore plays an important role in organic photovoltaics.

Once the charges are separated, they are transferred (under the influence of the potential difference of the electrodes) to respective electrodes to deliver current to the external circuit. Before their *extraction* at the electrodes, trapping and recombination at localised

states may occur (recombination of charges of different origin at the donor-acceptor interface is called *non-geminate*, bimolecular or Langevin recombination²⁷). This happens mostly due to discontinuity of the conductive molecular paths. There are two transport processes for the charge propagating through the medium – transport along the conjugated backbone (*band* transport) and transport between the molecules (*hopping* transport)²¹. The first one includes formation of various quasi-particles, such as solitons and polarons, which are localised but mobile excitations of the conjugated bonds. The transport is thus represented by a set of different ionic molecular states^{22, 28}. In highly ordered molecular crystals, however, it can be described by the band theory and conduction through delocalised π and π^* bands²⁸. The second process, hopping, is a movement of such quasi-particles from one molecule to another. Hopping is accompanied by the tunnelling through the ‘gaps’ between the adjacent molecules^{29, 30}.

Charge carrier *mobility* is an important parameter of each material and is determined by the processes mentioned above²¹. Its value varies according to type of the carrier. High and/or as close to equal as possible electron and hole mobilities result in enhanced charge transport and extraction, and hence better performance of the solar cell. Low and/or unequal electron and hole mobilities, generally lead to undesired *space charge* effects. These arise from accumulation of the carriers either due to their slow extraction or large distance to the collecting electrodes³¹. *Morphology* and molecular order are therefore crucial qualities of the photoactive films. Lastly, multilayer interfaces near the electrode represent additional potential barriers for the charge to overcome. This decreases the probability that the carrier will contribute to the generated current³².

1.2.3 Band structure

A *photovoltaic device* is realised when a layer of organic semiconductor is sandwiched between two electrodes with asymmetrical work-functions, as shown in Figure 2. The front electrode (*anode*) must be transparent in order to allow the sunlight to reach the active layer. Most commonly it is based on sputter-coated ITO (tin-doped indium oxide), but cheaper alternatives have recently emerged, such as Al-doped ZnO³³ (zinc oxide). The back electrode (*cathode*) is usually evaporated aluminium film, alternatively Ca or Mg (calcium or magnesium)¹¹. Due to work-function difference between the electrodes (ITO having a high work-function, Al having a low work-function), the electric field is created to drive the separated charges towards the contacts. This also causes the forward bias current to be several orders of magnitude higher than the reverse bias current. Such diode behaviour is characteristic for solar cells. It can be quantified by the diode equation as a parameter called *ideality factor*²⁶.

A semiconductor/metal interface (homojunction) is the simplest design able to generate photocurrent (Figure 2). A thin layer of organic *p*-semiconductor deposited between the electrodes forms a *Schottky junction* with the low work-function electrode and the semiconductor. As the Fermi levels align, the potential difference induces bending of the energy bands. The difference in permittivities is significant ($\epsilon_{\text{metal}} \ll \epsilon_{\text{semiconductor}}$) and thus the drop of the potential occurs almost purely within the semiconductor in the immediate vicinity of the junction. This region is called space charge region, or *depletion region*²⁶, and this is where the exciton dissociation takes place. The width of the region is defined as *depletion width* (W). As the diffusion length of excitons is of the order of 10 nm in organic semiconductors³⁴, only excitons generated near the junction can contribute to the

photocurrent which severely limits the performance of homojunction solar cells. Internal quantum efficiency of such Schottky devices is very poor (less than 1%) and reported power conversion efficiencies are usually on the order of 10^{-3} to $10^{-2}\%$ ³⁵.

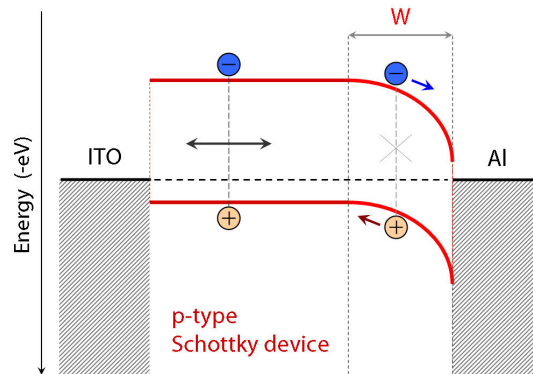


Figure 2. Energy bands in a *p*-type Schottky photovoltaic device.

Significant improvement can be achieved when the donor and acceptor materials are put together to form a heterojunction, as shown in Figure 3. A *bilayer heterojunction* consists of a planar interface of two organic semiconductors with different electron affinities and ionisation potentials (as mentioned before, the donor having higher electron affinity and ionisation potential than the acceptor).

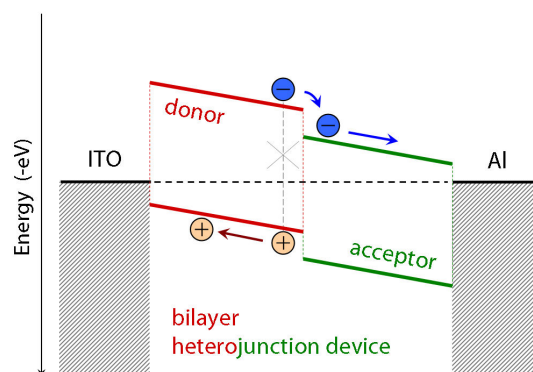


Figure 3. Energy bands of the donor and acceptor in a bilayer heterojunction.

The work-function of the sandwiching cathode should match the lowest unoccupied molecular orbital (LUMO) of the acceptor and the work-function of the anode highest occupied molecular orbital (HOMO) of the donor to minimise resistance at the contacts. The efficiency of the charge separation at the donor-acceptor interface greatly exceeds that of the semiconductor/metal contact. The architecture also reduces bimolecular recombination by allowing the transport of electrons through the *n*-type acceptor and holes through the *p*-type donor. As a result, power conversion efficiencies of the bilayer devices exceed those of Schottky junctions, reaching as much as 3.6% under standard AM 1.5 illumination^{36, 37}.

A major step in the development of organic solar cells came from the introduction of a *bulk heterojunction*, shown in Figure 4. The donor and acceptor are blended together to form a bi-continuous interpenetrated system.

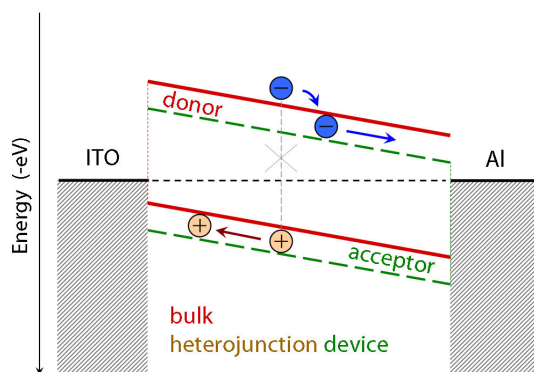


Figure 4. Energy bands of the donor and acceptor in a bulk heterojunction.

The concept of charge separation remains the same as for bilayers, however, the donor-acceptor interface is enormously enlarged. If the interface always lies within a distance smaller than the exciton diffusion length, each absorbed photon can theoretically be converted into separated charge carriers. Furthermore, if there is a continuous path from the interface to the

respective electrode for each material, the separated charge carriers can contribute to the external circuit current³⁵. *Internal quantum efficiency* (IQE, the ratio of the number of charge carriers collected by the cell to the number of absorbed photons) approaching 100% has already been achieved for polymer/fullerene solar cells³⁶, implying that such design is very efficient way of converting light into electricity. The highest power conversion efficiency reported for single bulk heterojunction-based device is a remarkable 9.2%³⁷.

1.2.4 Performance analysis

A solar cell's function in a circuit is similar to that of a battery. Its qualities are given by the current-voltage characteristics in the dark and under illumination, as shown in Figure 5. The potential difference present across the disconnected electrodes is called the *open circuit voltage* (V_{oc}). The current passing through the connected circuit without a load is called *short circuit current* (I_{sc}). If a resistance is present (R), the cell develops a voltage V ($0-V_{oc}$) and delivers a current I ($0-I_{sc}$) determined by the Ohm's law $V = RI$. Therefore, both operating voltage V and current I are dependent on the load and on the amount of illumination.

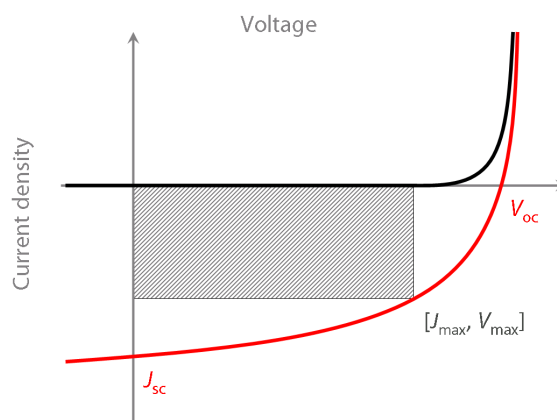


Figure 5. Dark (black line) and light (red line) I - V curve of a photovoltaic cell.

The origin of the V_{oc} in organic solar cells has been the matter of intensive studies and discussions for many years³⁸⁻⁴¹. It has been established that the value of V_{oc} directly corresponds to the energy difference of the donor's HOMO and the acceptor's LUMO and the influence of the electrode work-functions is only minor. As the photo-generated current I_{sc} is proportional to the illuminated area, J_{sc} (short-circuit current density) is usually taken as the main current-generation characteristic of the solar cell. Among others, J_{sc} depends on the incoming photon flux density, the absorption and *external quantum efficiency* of the device (EQE, the ratio of the number of charge carriers collected by the cell to the number of all incoming photons; EQE is reciprocal to the optical band-gap) and the charge carrier mobility⁴². V_{oc} and J_{sc} are complemented by the quality parameter *fill factor* (FF). Its value is derived from the maximum operating power point of the device (corresponding to V_m and J_m , see Figure 5) and it is defined as $FF = J_m V_m / J_{sc} V_{oc}$ ²⁶. The FF is a measure of the *J-V* curve's shape-optimality. Finally, each solar cell is characterised by the most common and practically the most important property – the *power conversion efficiency* (PCE, i.e. how efficiently it is able to convert the sun energy into the electrical energy). By combining the V_{oc} , J_{sc} and FF, one can obtain the relation $PCE = J_{sc} V_{oc} FF / P_0$, where P_0 is the incident power light density²⁶.

All the aforementioned parameters (V_{oc} , J_{sc} , FF and PCE) are dependent on the amount of illumination^{45, 46}, therefore standard test conditions are followed in order to achieve the data comparability⁴³. The reference illumination spectrum is the *Air Mass 1.5 spectrum* (or AM1.5) and it corresponds to the spectrum of sunlight reaching the Earth's surface for mid-latitudes⁴⁴. The standard illumination power density is 100 mWcm^{-2} .

Parasitic resistances, namely series and shunt resistance, influence the performance of every photovoltaic cell (see Figure 6). *Series resistance* (R_s) results from the device resistance to the current flow, including resistance of the active material, top and bottom electrode contacts and the electrodes themselves. High values of the series resistance are related to poor solar cell design and can significantly reduce FF and J_{sc} . *Shunt resistance* (R_{sh} , also called parallel resistance) inhibits leakage of the current through/around the edges of the cell. Low shunt resistance results from various manufacturing defects and leads to reduced FF and V_{oc} ²⁶. Ideally, the series resistance should be as small whereas the parallel (shunt) resistance as big as possible.

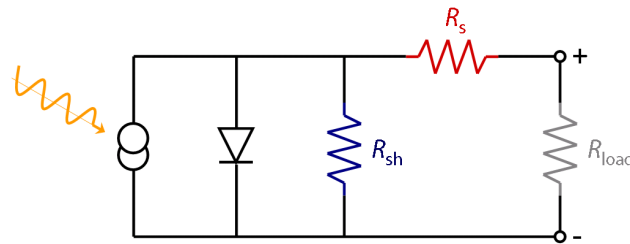


Figure 6. Series and shunt resistance in the equivalent circuit of a solar cell.

One other phenomenon influencing the performance of organic solar cells is the presence of space charge effects. Spatial accumulation of carriers within a phase leads to build up of a net charge. The net charge creates an electric field which opposes the built-in field and limits the carrier flow. This results in an increased monomolecular and bimolecular recombination. The effects of space charge are most significant in planar heterojunctions where the photo-generated carriers are concentrated near the donor-acceptor interface. As the electrons are confined exclusively to the acceptor and the holes to the donor, a substantial net charge density exists in the respective bulk phases even when the carrier mobilities are matched. Such net charge is minimised in bulk heterojunctions where the

interfaces are enlarged and distributed within the bulk. In bulk heterojunctions, any accumulation of the carriers can be prevented by matching electron and hole mobilities³¹.

1.2.5 Device architectures and performance improvements

Enhancement of light absorption has been one of the major factors driving the development of solar cell architecture³⁵. In bilayer heterojunction, the exciton diffusion length is short in comparison to its optical absorption length. Thus devices suffer from reduced absorption as they require thin photoactive layers to utilise the excitons. Bulk heterojunction geometry overcomes this to an extent, but is limited by carrier mobilities and charge extraction. This has stimulated many attempts to optimise the nanoscale morphology of phase-separated donor-acceptor blends⁴⁹⁻⁵¹ (discussed in section 1.3.2) and introduced device modifications to improve performance^{52, 53}.

Better charge carrier collection can be achieved using *exciton blocking layers*⁴⁵⁻⁴⁸. The function of these 'buffer' layers is to prevent exciton quenching at the organic semiconductor/cathode interface⁴⁹, lower the electron injection barrier⁵⁰, and additionally to protect organics during the cathode evaporation⁵¹. Their application often results in FF and V_{oc} improvements. The main material requirements are transparency and good electron conductivity. The contact resistance at the anode interface can be decreased by insertion of a conductive polymer (often PEDOT:PSS, poly(3,4-ethylene dioxathiophene) doped with poly(styrene sulfonate)⁵²), or various metal-oxide thin films^{56, 61-63}. Finally, photoabsorption of the device can be increased by aligning position of the active layer with the maximum intensity of illumination. Due to optical interference of the incoming waves and the waves reflected from the back metal electrode, spatial distribution of the light intensity varies

over the device thickness⁵³. Transparent *optical spacer* layers thus can be employed to shift the active area towards the intensity peak of some favourable wavelengths^{53, 65}.

The use of structures with multiple active layers has long been another way of improving photovoltaic performance. This includes *p-i-n* solar cells, obtained by sandwiching of the blended photoactive layer between *p*-type and *n*-type materials^{54, 55}, and *tandem cells*, obtained by stacking of two heterojunctions in series or parallel⁵⁶. While the former leads mainly to enhanced photocurrent, the latter can be designed to increase either photovoltage (when connected in series) or photocurrent (when connected in parallel). A typical tandem solar cell combines two subcells with a different spectral range of absorption – the top cell (or front cell) with a high band-gap material and the bottom cell (or rear cell) with a low band-gap material. As illustrated in Figure 7, the complementary absorption spectra of the subcells allow more effective use of the incoming light, and their connection in series the addition of their individual photovoltages⁵⁷. A transparent and conducting interconnection layer is introduced between the cells to align the Fermi levels of the subcells⁵⁸. Tandem architectures have reached the highest power conversion efficiencies in organic photovoltaics to date (10.7%)⁵⁹⁻⁶².

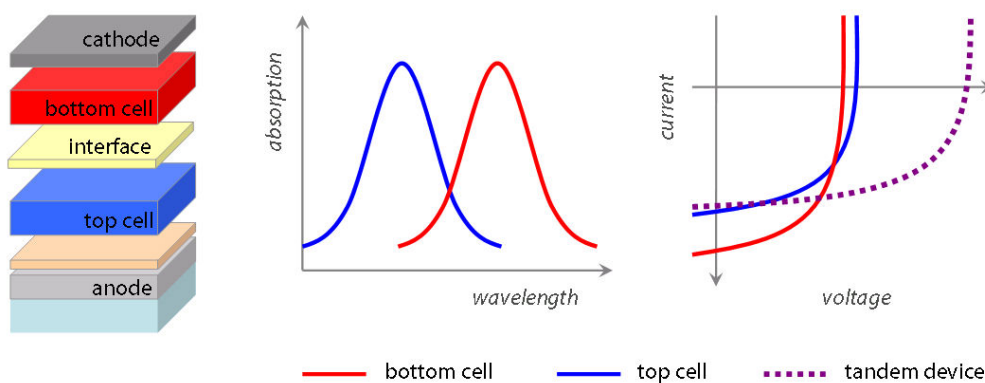


Figure 7. Schematic illustration of possible absorption spectra and *I-V* characteristics of a tandem solar cell.

As it is in inorganic photovoltaics⁶³, the best performing architectures for future organic photovoltaics needs to be based on advanced combination of multilayered structures. *Multijunction solar cell* design is the effective way to overcome the Shockley-Queisser limit⁶⁴ (stating thermodynamic limitations of the energy conversion efficiency in a solar cell) and achieve significantly better performance⁶⁵. In contrast to the maximum efficiency of a single junction (30%), a tandem solar cell with two subcells (band-gaps of photoactive layers 1.9 and 1.0 eV) can theoretically reach PCE of 42%, while a three-subcell tandem (band-gaps 2.3, 1.4, and 0.8 eV) as much as 49%⁶⁶.

The *deposition process* itself has a crucial role in the development of multijunction solar cells. Molecular junctions connected by numerous interface layers can be stacked on top of each other almost without any limitations when a dry deposition process is involved⁶⁷. It would, however, be a challenge to achieve similar complexity in solution-processed polymer devices (these material groups will be discussed later in section 1.3.2). Fabrication of efficient polymer tandem cells has long been constrained by issues with orthogonality of the solvents and it is still rare, that these devices show competitive performance to their single-junction counterparts^{60, 61, 68}.

1.3 Organic materials for solar cells

1.3.1 Low molecular weight materials

Organic semiconductors for solar cells generally fall into main two categories – *low molecular weight* ‘molecular’ materials and *high molecular weight* materials. The former have usually well-defined dimensions and molecular weight, and are often deposited by

vacuum evaporation. Examples include oligomers, fullerenes and phthalocyanines⁶⁹. Due to their simple processing, molecular semiconductors have played a major role in the development of OLEDs²⁰ and also pioneered the field of organic photovoltaics⁷⁰⁻⁷².

The photovoltaic physics of small molecules follows the same principles as described above for general organic semiconductors. Similar state-of-the-art performances have been reported for both low and high molecular weight solar cells^{15, 68}. Improvements in chemical design of the small-molecule donors have recently enhanced their absorption in the near-infrared region^{85, 86} and the molecular solar cells, processed either in vacuum or solution, have once again become competitive with polymer-based photovoltaics⁷³⁻⁷⁵.

In particular, the use of solvent-free *vacuum processing* allows these materials to be applied in complex multilayered structures^{62, 67}. The active layers can be easily deposited in the form of *p-i-n* junctions or as gradient blends with precise manipulation of horizontal as well as vertical donor-acceptor composition^{76, 77}. Control of the nanoscale phase morphology in vacuum-deposited active blends, however, remains a challenge. Co-evaporation does not lead to bi-continuous interpenetrated donor-acceptor network, but rather a uniform mixture of the two materials with minimal evidence of phase separation. The resulting isolated islands of individual materials inhibit efficient charge transport and collection⁶⁹. Heating of the substrate during the deposition^{78, 79}, use of evaporation additives⁸⁰, and thermal annealing of the device after the fabrication⁸¹ have been shown to improve the heterojunction morphology only to a certain degree.

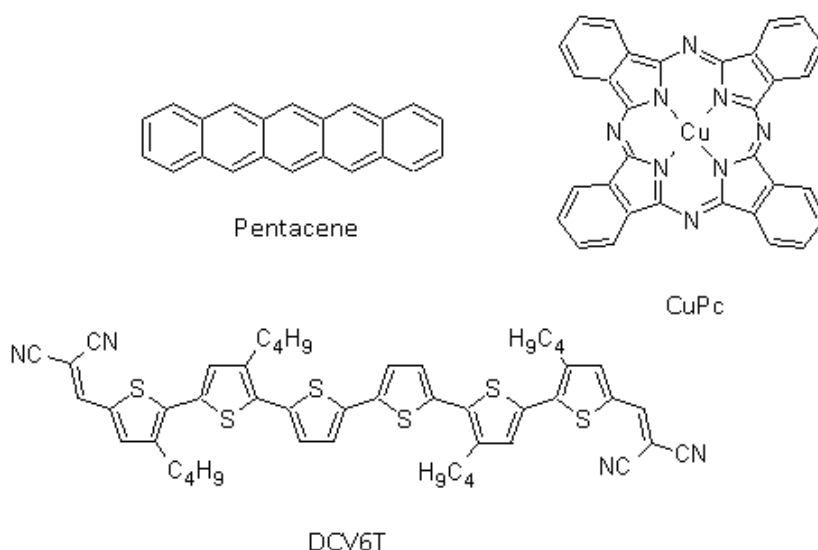


Figure 8. Chemical structure of typical small molecular donors.

Common molecular *donors* are metal *phthalocyanines*³⁴ (primarily CuPc and ZnPc), *oligothiophenes*⁹⁶ and *squaraines*⁸². Older molecular donor materials include porphyrins, oligoacenes and perylene derivatives^{24, 69, 83}. CuPc has been used in organic photovoltaics for several decades. Its strong absorption, good molecular order and stability made it standard material for vacuum-deposited photovoltaics. The highest single junction PCE of 4.2% under concentrated sunlight was achieved by Xue *et al*⁸⁴.

Novel chemically-modified donor-acceptor (D is electron rich and A is electron deficient) molecular compounds have recently emerged as promising absorbers and electron donors⁸⁵⁻⁹⁰. Optimisation of HOMO and LUMO levels through attachment of various D and A groups minimises energy losses during exciton separation and ‘customises’ the molecule for coupling with an electron acceptor. D-A substituted oligothiophene derivatives (such as dicyanovinyl-substituted oligothiophenes, DCVnT) have reached single-junction efficiencies of 6.9%⁷³. Significant development of small molecule donors has taken place also in

solution-processed molecular photovoltaics^{74, 75, 91}. Again, a D-A 'push-pull' approach has led to rapid improvement in performance and to PCE as high as 7.0%⁷⁵.

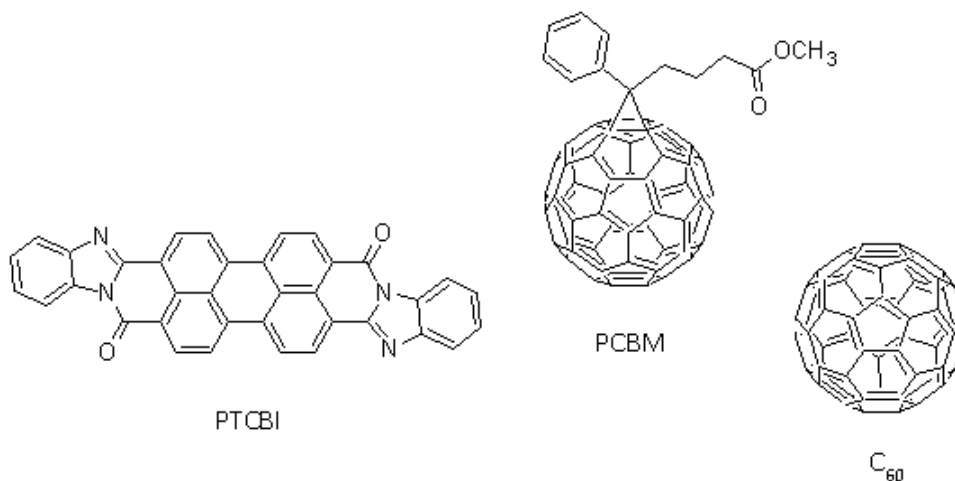


Figure 9. Chemical structure of typical small molecular acceptors.

The most prominent low molecular weight *acceptors* are *fullerenes* C₆₀, C₇₀ and their derivatives⁹². Non-fullerene acceptors include perylenes (mainly perylene diimides, PDIs), and a plethora of recently reported D-A compounds^{93, 94} (such as vinazenes, diketopyrrolopyrroles, bifluorenilidenes, etc.). Fullerene-based acceptors keep a long-term dominant position in organic photovoltaics due to their high electron affinity, excellent charge transport properties, beneficial molecular shape and easy accessibility^{69, 95, 96}. For example, [6,6]-phenyl-C₆₁-butyric acid methyl ester (PCBM) is a soluble version of C₆₀ which has been greatly investigated over the last decade. Its combination with polymeric donor poly(3-hexylthiophene) (P3HT) was long a basis for state-of-the-art device performance⁹⁷. Modified fullerenes, such as endohedral metallofullerenes and C₆₀/PCBM bisadducts, have tackled poor light absorption of C₆₀ as well as its V_{oc} -limiting low LUMO level^{96, 98-100}.

1.3.2 High molecular weight materials

High molecular weight materials for organic solar cells are represented predominantly by *conjugated polymers*. Since the discovery of conductivity in doped poly(acetylene)¹⁰¹, the field of conjugated polymers has expanded enormously¹⁰². Freedom in molecular design (e.g. using multiple D-A groups to tune position of HOMO and LUMO energy levels) and relative simplicity of modifications have allowed polymers to obtain almost optimal donor properties¹¹⁸⁻¹²⁰. Moreover, natural phase separation in polymer-fullerene blends has led to good morphology control and thus efficient charge extraction^{38, 121}.

Polymers are long-chain molecules consisting of a large number of repeating units (monomers)¹⁰³. Their molecular weight usually ranges between 1000 and 100 000 gmol⁻¹ and their processing for electronics is entirely solution-based. The physical and chemical properties are determined by the molecular structure, such as architecture of the conjugated backbone, chain length and character of side groups¹⁰⁴. Their specific 1-dimensional character has a strong influence on their electronic behaviour. As described previously for organic semiconductors, *sp*² hybridised orbitals of individual carbon (nitrogen, oxygen or sulphur) atoms overlap along the backbone to form long electron π and π^* -bands. The quality of this orbital overlap (as well as of the orbital overlap between the adjacent molecules) is a crucial parameter for the transport of the charge carriers⁴². Convoluted conformation, chain defects or molecular disorder often lead to charge recombination. In addition, due to weak inter-molecular interactions and low resistance of the polymer towards torsion, the planarity of the conjugated backbone (consequently orbital overlap and mobility) can be affected by non-structural factors, such as temperature²⁰.

The vast majority of un-doped conjugated polymers are *electron donors* upon photo-excitation. Most of them have better hole mobility than electron mobility¹⁰⁵. Well-established representatives of such hole-conductors are *phenylenevinylenes* (poly[2-methoxy-5-(3,7-dimethyloctyloxy)-1,4-phenylenevinylene], MDMO-PPV, poly[2-methoxy-5-(2'-ethylhexoxy)-1,4-phenylenevinylene], MEH-PPV) and *polythiophenes* (mainly poly(3-hexylthiophene-2,5-diyl), P3HT)^{35, 106}, as illustrated in Figure 10.

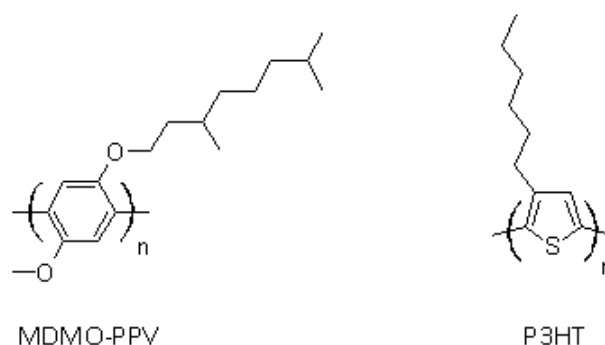


Figure 10. Chemical structure of MDMO-PPV and P3HT donors.

Polythiophenes (mostly poly(3-alkylthiophenes), P3AT) in organic electronics have been the subject of intensive studies for a several decades¹²⁶⁻¹²⁸. These materials have a high mobility (up to $0.1 \text{ cm}^2 \text{V}^{-1} \text{s}^{-1}$)¹⁰⁷ and owing to the side chains they are easily processable in common organic solvents. Their excellent electronic properties arise from the ability to crystallise into layered structures (*lamellae*)¹⁰⁸ where the neighbouring backbones are closely packed on the top of each other in a face-to-face arrangement (so-called π -stacking)¹⁰⁹. The π -stacking is facilitated by the planarity of the monomers (as such, it can be observed mainly in alkylthiophenes and alkylthiazoles)¹¹⁰. In each plane, the conductive backbones are separated by isolating alkyl side groups. Better structural order increases carrier delocalisation which results in improved mobility. The charge carrier mobility has been shown to depend additionally on regioregularity of the P3ATs' backbones^{111, 112}

(regioregular polythiophenes having orders of magnitude higher mobility than regiorandom polymers), the direction of π -stacking relative to the substrate¹¹³, and the polymer's molecular weight¹¹⁴.

The poly(thiophene) with the best performance in photovoltaic devices has been poly(3-hexylthiophene) (P3HT)¹¹⁵. Schilinsky *et al.* was the first one to combine it with PCBM into a blended heterojunction¹¹⁶. Efficient exciton dissociation and charge extraction were soon achieved by precise control of the blend morphology. A substantial step forward was an introduction of *post-production thermal annealing*¹¹⁷. Polymer crystallisation lead to both greatly improved nanoscale organisation of the materials' phases and better charge transport^{139, 140}. The influence of annealing on the morphological development in polymer-fullerene blends became a subject of extensive studies and a driving factor towards a better performance^{112, 141}. The complex morphology-performance relationship has been revealed only recently¹¹⁸⁻¹²³, describing the annealed blend as intercalated PCBM aggregates and P3HT crystallites immersed in the matrix of P3HT amorphous chains and dispersed PCBM molecules. The highest power conversion efficiencies of P3HT:PCBM devices reached 5%. Although limited absorption of P3HT (~1.9 eV band-gap) and small V_{oc} of the P3HT-PCBM combination (0.6 V) have narrowed their commercialisation, they have remained a standard platform for fundamental research in organic photovoltaics¹²⁴.

Various low band-gap polymers have been recently synthesised using D-A push-pull approach. These copolymers are mostly based on a combination of *benzothiadiazole*, *carbazole* and *cyclopentadithiophene* units^{68, 125}, as shown in Figure 11. Modification of the energy levels allowed their HOMO levels to be lowered (yielding high V_{oc} in combination with PCBM) while extending the band-gaps to 800-900 nm.

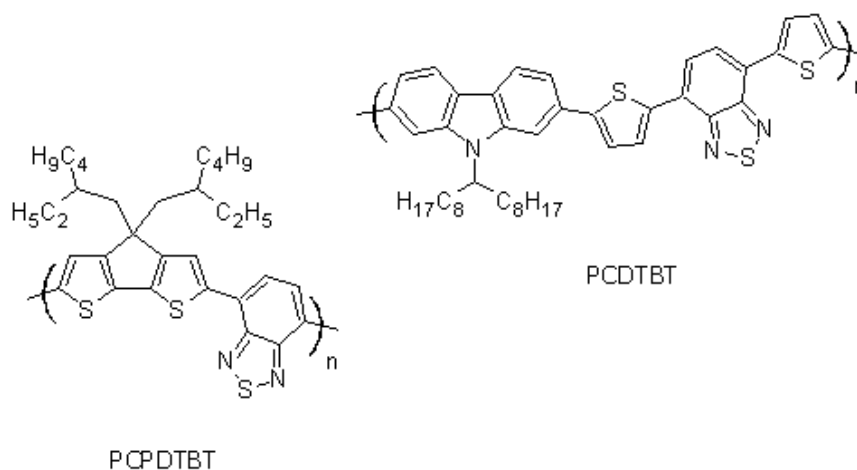


Figure 11. PCPDTBT and PCDTBT as examples of copolymers based on a carbazole unit.

The most representative of these copolymers are poly[N-9'-hepta-decanyl-2,7-carbazole-alt-5,5-(4',7'-di-2-thienyl-2',1',3'-benzothiadiazole)] (PCDTBT)^{38, 149} and poly[2,6-(4,4-bis-(2-ethylhexyl) -4H-cyclopenta[2,1-b;3,4-b']-dithiophene) -alt-4,7-(2,1,3-benzothiadiazole)] (PCPDTBT)^{150, 151}, both exceeding 5.5% PCE when combined with PCBM. Series of novel copolymers introduced by Yu *et al.* are based on alternating units of *thieno[3,4-b]-thiophene* and *benzodithiophene* and have demonstrated impressive single-junction efficiencies of 9.2%^{39, 152-155}.

1.4 Deposition techniques

1.4.1 Laboratory vs. industrial processing

Materials for organic electronics are deposited by various 'wet' or 'dry' methods (individually discussed in the following sections). The wet methods make use of solvents in which the molecules are dissolved to be applied on a substrate by *coating* or *printing*. The solvent is removed during/after the deposition. Despite several advantages, such as simple

small-scale laboratory application, the *solution processing* suffers from the processing medium itself - *solvent*. The organic solvents have low specificity, therefore they tend to interact with (and damage) previously deposited layers. This problem is intrinsic and substantially limits the complexity of the device that can be obtained by the wet methods⁶⁵. Sophisticated material sequences soluble in incompatible solvents have to be chosen, or one or more inner layers need to be deposited in vacuum to overcome this issue. In either case, compromises are made which sacrifice the production simplicity or performance parameters.

Dry processing is another means of organic molecule deposition. It is conducted under vacuum using thermal heating or focused beam of particles (e.g. ions or electrons). As there are no solvents used, the processing allows for an unlimited number of layers to be grown, all with precise control of the film thickness. *Vacuum thermal evaporation* is an example of inexpensive and commonly used method widely exploited, for example, in the packaging industry^{13, 126}. It has been applied to large-scale production of OLEDs²⁰ and serves as the technology platform in the Heliatek's production facility for organic solar cells¹⁸.

The capability and complexity of the process influence the price and scale of the product. $Costs/m^2$ is a crucial ratio which defines a potential of the method to be transferred from laboratory to industrial use. It is important to note, that the organic photovoltaics do not aim to challenge the performance and stability of inorganic solar cells (based on Si or GaAs) but rather offers a low-cost alternative. That means that lower efficiencies and shorter lifetimes would be compensated by lower production costs. The calculations of Dennler *et al.*⁹⁷ show considerable relationship between *efficiency/lifetime/cost* – the lower is the module cost, the less important lifetime and efficiency become. The thin-film organic

electronics has an advantageous potential to be applied on *flexible substrates* and thus involve low-cost roll-to-roll (R2R) processes. Explicit comparison done by Brabec *et al.*¹²⁷ states that the equivalent annual m² output of a typical Si wafer production plant (cca 90 000 m² of Ø30 cm wafers) is processable by a standard R2R web printer within a few hours. This illustrates that it is great speed and capacity which make R2R such powerful large-scale manufacturing option. Finally, cheap and flexible electronics can stimulate new design opportunities due to their light weight, mechanical flexibility and semitransparency.

Technically, *roll-to-roll processing* involves a deposition of the source material onto a flexible substrate (so-called web) which is being rewound from one roll to another. Webs several meters wide and 10s of km long can be rolled with speeds exceeding 10 m/s¹³. Multiple sources can be used for the sequential deposition of different active/interface layers and various treatments (such as heating, drying or UV-curing) can be applied in-situ. The following sections aim to summarise some of the major techniques for the deposition of organic molecules, their main principles, pros/cons and potential to contribute to low-cost organic photovoltaics.

1.4.2 Vacuum deposition

Vacuum thermal evaporation (VTE). Vacuum thermal evaporation is the simplest and most commonly used vacuum deposition technique. The source material is placed in a conductive boat which is heated under vacuum by a large DC current (the boat is made of a high melting point metal – e.g. tungsten, molybdenum or tantalum), as shown in Figure 12. The evaporated/sublimed material is deposited on the substrate placed above the source. The VTE process is advantageous for its simplicity (i.e. evaporation of numerous

layers or co-evaporation of various different compounds), homogeneity of the deposited films, high speed deposition, and its precise film-thickness control ($\pm 0.5 \text{ nm}$)¹²⁸. The wasteful consumption of the material and non-uniformity of the deposition rate are the main drawbacks. The technique is R2R compatible and is widely used for the deposition of small organic molecular films (OLED, OPV) as well as semiconductor nanostructures for inorganic electronics. On a larger scale it is employed in the packaging industry (e.g. aluminium coating of plastic substrates - the technology routinely processes 4 m wide and 60 000 m long webs with speeds of more than 16 m/s¹²⁹).

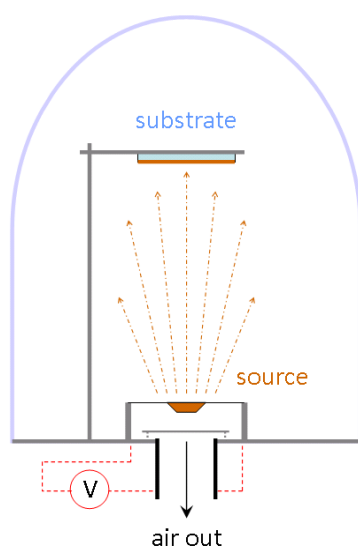


Figure 12. Schematic drawing of vacuum thermal evaporation.

Thermal evaporation of organics is fundamentally limited by their thermodynamic stability. Heating above certain temperatures leads to degradation (such as breaking of the backbone bonds, cleavage of the side groups/atoms) and hence, in polymers, a rapid molecular weight decrease¹³⁰. The size of the polymer defines its conformational entropy and an increased temperature is needed to transfer the molecule from the solid to the gaseous state as the molecular weight increases. Such thermal energy is, however, often

sufficient to overcome some of the bonding energies within the molecule. The resulting thermal dissociation is thus an unavoidable physical phenomenon. It determines the maximum size of the polymer fragment capable of such phase change¹³⁰ (e.g. for polyethylene it is around 1500-2000 gmol⁻¹).

When heated-up, polymers usually go through a *glass transition point* (T_g) and a *melting point* (T_m , if semicrystalline) before reaching the *evaporation temperature* (T_e). The smallest fragments are evaporated first, followed by bigger oligomers and short-chain polymers. The angular distribution of the gaseous material flow emitted from a point source follows a cosine law¹³⁰. Vacuum, in which the deposition process takes place, increases the probability of the gas molecules reaching the substrate by reducing the number of inter-molecular collisions and hence increasing the mean free path. It also provides better control over the process reactivity and minimises impurities¹³.

The *surface conditions* are another influential factor of the thin-film growth. These include mainly the character of the substrate and its temperature, as well as the chemical activity, flux density and velocity of the depositing molecules themselves. Higher substrate temperature promotes a greater surface migration as the molecules have more energy to find a position minimizing their potential. Sufficient mobility of the molecules leads to ordered film growth and can even result in a partial reconstruction of the polymer at the surface¹³⁰. Enhancement of the surface molecular order can be achieved when depositing molecules with better structural regularity.

VTE of polymers for organic electronics has been investigated since the late 1980s. Initial structural, morphological and fluorescent studies of vacuum-deposited poly(p-phenylene)

(PPP) thin films¹³¹⁻¹³³ quickly lead to the successful assembly of the first polymer organic electroluminescent devices processed in vacuum^{134, 135}. Kobayashi *et al.* characterised their electroluminescence (EL) in terms of the thickness of individual hole-/electron-transporting layers and the substrate temperature during the deposition. However, only basic electronic and optical characterisation was performed. They found that heating of the condensation surface improves the material's crystallinity and luminance. Supported by XRD and electroluminescence measurements, the work suggested that it is molecular orientation which increases luminance by positively affecting charge transport (no comparison of the relevant quantities, e.g. charge carrier mobilities, was performed). This corrected the previous observation of Masui *et al.*¹³⁶, who attributed enhanced EL properties of OLEDs to an amorphous film structure. The Kobayashi's conclusion had more convincing theoretical reasoning and was later approved by other studies¹³⁷.

Although the report referred to limitations regarding the thermal decomposition of the polymer¹³⁸, it was Song *et al.*¹³⁹ and Lee *et al.*¹⁴⁰ who actually identified and compared molecular weight of the starting and evaporated PPP materials. Moreover, they conducted evaporation at a well-defined temperature that allowed consistency and reproducibility to be achieved. They calculated that the degree of conjugation of the evaporated polymer (according to the IR peak intensity ratios) was reduced, being only about $\frac{1}{3}$ of the starting PPP. Additional structural information was shown in photoluminescent (PL) spectra of the compounds. The dispersion of conjugated lengths narrowed in evaporated PPP. In agreement with the IR spectroscopy, the PL intensities implied that the vacuum-deposited polymer had smaller molecular weight than the starting one (higher peak intensity at shorter wavelengths) whereas the PPP remaining in the boat consisted of more stable and longer chains (higher peak intensity at longer wavelengths). The latter was further supported by

TGA. More systematic electrical characterisation of PPP-based monolayers and bilayers appeared in two consecutive works of Lee *et al*^{165, 170}. Findings included values of EQE, calculation of charge carrier mobilities and the dynamics of charge carrier recombination.

Bilayer OLEDs fabricated by Lee *et al.* combined PPP with a spin-coated poly(N-vinylcarbazole) (PVK)¹³⁵. However, an earlier report had already shown that PVK can be vacuum-deposited as well¹⁴¹. There, Touihri *et al.* studied different doping techniques of evaporated PVK films. Based on TGA, IR and optical absorption analyses, he suggested that PVK is not destroyed, but rather decreased in terms of molecular weight. This can be partially reverted by post-production annealing in iodine atmosphere. Despite successful application of PVK in emitting devices^{142, 143}, no additional attempts have been reported to produce purely vacuum-processed PPP/PVK polymer-polymer OLED.

Improved performance of electroluminescent diodes can be achieved by insertion of a thin insulated layer at the organic semiconductor interface/anode¹⁴⁴. D'Almeida *et al.*¹⁴⁵ demonstrated deposition of such layer by VTE (using insulating poly(tetrabromo-p-phenylenediselenide) (PBrPDSe)). The study revealed that the PBrPDSe film was amorphous (XRD) and the material was not decomposed during the evaporation (IR spectroscopy). Based on a rather weak and non-quantitative solubility test, the authors suggested that the conjugation length was strongly decreased.

The first of several studies of vacuum-deposited polymer field effect transistors (OFET) was recently reported by Irimia-Vladu *et al*¹⁴⁶. Polyaniline was evaporated as an insulating gate layer, followed by deposition of the active semiconductor C₆₀. Again, FT-IR and UV-vis characterisation indicated a decrease in molecular weight and small structural

changes (oxidation state). The work was a good evidence that OFETs can be processed purely in vacuum without the use of any solution steps. This certainly leads to better production consistency and versatility. Nevertheless, it would be interesting to see an example of OFET based only on polyaniline which itself can be doped to achieve different conductive states^{177, 178}.

In summary, several attempts to apply VTE in the deposition of polymers for organic electronics have been reported. It is unfortunate, however, that despite certain success this research has not been further developed. No semiconducting polymers have been vacuum-applied in OFETs or organic solar cells. Considering the strengths of the processing method in the deposition of multilayered structures, many new challengers and opportunities could have been explored if wider attention was brought to polymer vacuum deposition.

Organic vapour phase deposition (OVPD). Organic vapour phase deposition was developed by Forrest *et al.* as a more controlled alternative to VTE¹⁴⁷. The technology relies on an inert carrier gas (N₂ or Ar) heated at the temperature sufficiently high to induce evaporation of the material with which it is in the contact. The gas and evaporated compound are further carried through the hot-wall reactor vessel towards a cooled substrate. Deposited films are uniform with well defined thickness. There are no material losses during the process. The rate of the deposition as well as the crystalline morphology¹⁴⁸ is fully controlled by the pressure and temperature in the reactor. Although OVPD has already been used for fabrication of OLEDs^{181, 182} and organic photovoltaic cells^{183, 184}, its deposition speed and compatibility with R2R still need to be addressed.

Chemical vapour deposition (CVD). Chemical vapour deposition falls into the category of chemical processing. Hence, molecules are not 'physically' transferred from the target onto the substrate but, rather, are chemically formed at the substrate surface from different precursors. Thin polymer layers are polymerised from deposited monomers (e.g. by VTE or OVPD¹⁴⁹) under ultra-high vacuum. The polymerisation can further be promoted in the presence of free electrons, a technique called plasma-enhanced CVD. Such polymers, however, lack regularity and are randomly terminated or cross-linked. It is also questionable at the moment whether CVD can provide competitive cost/m² to VTE or solution-based printing/coating techniques.

Another recognized techniques for polymer deposition, *matrix assisted pulsed laser evaporation* and the *ion beam-assisted deposition*, are variations of the standard pulsed laser deposition^{150, 151}. The processing occurs under ultra-high vacuum by the use of laser/ion beam focused onto the solid polymer target. The material is ablated and molecular fragments deposit onto the adjacent substrate. These techniques are relevant research tools, but their application in industry is unlikely.

1.4.3 Coating and printing techniques

Solution processing is currently the preferred method for fabrication/production of organic photovoltaics^{12, 68, 91}. The most prolific representative, *spin coating*, has played a dominant role in the development of organic photovoltaics. Although it is a technique highly suitable for laboratory research, it has no potential to be scaled-up and only remotely represents real device-processing conditions. This means that a great amount of work is still ongoing on transferring these materials to larger industrial processing.

The development of suitable ink technology is one of the primary issues¹². To obtain an appropriate ink 'printability', a number of properties need to be considered and adjusted - e.g. viscosity, surface tension, surface energy or volatility. Moreover, the ink optimisation varies for each particular printing or coating technique. Additives are generally employed to achieve such modifications, however, they can be applied only with a limited freedom as they affect the electronic properties of the films. The role of engineering in the scale-up is also of a great importance. Since many printing/coating processes are contact-based, advanced design and precision of the equipment are required (mechanical accuracy, uniform web and liquid supply, substrate consistency, etc.). This poses serious challenges especially for some of the more complex techniques required for multilayer deposition.

Numerous steps to scale-up and transfer the wet processing into large-scale production have been undertaken by Krebs *et al*¹⁵²⁻¹⁵⁴. Substantial progress has been done especially to make the deposition of polymer solar cell compatible with R2R methods^{12, 152}. This involves techniques such as *doctor blading*, *slot-die coating* and *screen printing*¹⁵⁵⁻¹⁵⁷. *Ink-jet printing* remains the dominant technology for patterned device fabrication^{158, 159}. Several companies (e.g. Konarka and Solarmer) have already focused on the development of printed of organic solar cells¹⁶⁰. Only next stages will show if these efforts will successfully bridge the gap between small-scale laboratory fabrication and large-scale plant production of solution-based photovoltaics.

1.5 References

1. Fanchi, J. R., *Energy in the 21st Century*. World Scientific Publishing Co Pte Ltd: 2005; p 243

2. *International Energy Outlook 2011* U.S. Energy Information Administration: Washington D.C., 2011.
3. Boyle, G.; Everett, B.; Ramage, J., *Energy Systems and Sustainability* OUP Oxford 2003; p 640
4. *Renewables 2011: Global Status Report*; REN21: Paris, 2011.
5. Wengenmayr, R.; Bührke, T., *Renewable Energy: Sustainable Energy Concepts for the Future* Wiley VCH 2008; p 120.
6. Jha, A. R., *Solar Cell Technology and Applications*. CRC Press: 2009; p 280.
7. Green, M. A.; Emery, K.; Hishikawa, Y.; Warta, W.; Dunlop, E. D. *Progress in Photovoltaics* **2012**, 20, (1), 12-20.
8. Osborne, M., First Solar first to US\$1 per watt manufacturing cost. *PV-Tech* 2009.
9. *Thin-Film Photovoltaic Cells Market Analysis to 2020*; GBI Research: 2010.
10. Pagliaro, M.; Palmisano, G.; Ciriminna, R., *Flexible Solar Cells* Wiley VCH: 2008; p 202.
11. Sun, S.-S.; Sariciftci, N. S., *Organic Photovoltaics: Mechanism, Materials, and Devices*. 1 ed.; CRC Press: 2005; p 664
12. Krebs, F. C. *Solar Energy Materials and Solar Cells* **2009**, 93, (4), 394-412.
13. Bishop, C., *Vacuum Deposition Onto Webs, Films and Foils* William Andrew 2007; p 495
14. Klauk, H., *Organic Electronics: Materials, Manufacturing, and Applications*. John Wiley & Sons: 2007; p 446.
15. Heliatek sets new world record efficiency of 10.7% for its organic tandem cell. <http://www.heliatek.com>
16. Peters, C. H.; Sachs-Quintana, I. T.; Kastrop, J. P.; Beaupre, S.; Leclerc, M.; McGehee, M. D. *Advanced Energy Materials* **2011**, 1, (4), 491-494.
17. Konarka, Konarka Opens World's Largest Roll-to-Roll Thin Film Solar Manufacturing Facility with One Gigawatt Nameplate Capacity. In 2008.
18. Heliatek, Heliatek opens groundbreaking production facility for the manufacture of organic solar filmsorganic based photovoltaics. In 2012.
19. Clayden, J.; Greeves, N.; Warren, S.; Wothers, P., *Organic Chemistry* OUP Oxford 2001; p 1536
20. Li, Z.; Meng, H., *Organic Light-Emitting Materials and Devices* CRC Press: 2006; p 673
21. Bower, D. I., *An Introduction to Polymer Physics* Cambridge University Press 2002; p 468
22. Brütting, W., *Physics of Organic Semiconductors* Wiley VCH 2005; p 554.
23. Gunes, S.; Neugebauer, H.; Sariciftci, N. S. *Chemical Reviews* **2007**, 107, (4), 1324-1338.
24. Peumans, P.; Yakimov, A.; Forrest, S. R. *Journal of Applied Physics* **2003**, 93, (7), 3693-3723.
25. Pal, S. K.; Kesti, T.; Maiti, M.; Zhang, F. L.; Inganas, O.; Hellstrom, S.; Andersson, M. R.; Oswald, F.; Langa, F.; Osterman, T.; Pascher, T.; Yartsev, A.; Sundstrom, V. *Journal of the American Chemical Society* **2010**, 132, (35), 12440-12451.
26. Nelson, J., *The Physics of Solar Cells*. Imperial College Press 2003; p 384

27. Koster, L. J. A.; Mihailetchi, V. D.; Blom, P. W. M. *Applied Physics Letters* **2006**, 88, (5).
28. Warta, W.; Stehle, R.; Karl, N. *Applied Physics a-Materials Science & Processing* **1985**, 36, (3), 163-170.
29. Pope, M.; Swenberg, C. E., *Electronic Processes in Organic Crystals and Polymers* OUP USA: 1999; p 1328
30. Tessler, N.; Preezant, Y.; Rappaport, N.; Roichman, Y. *Advanced Materials* **2009**, 21, (27), 2741-2761.
31. Scully, S. R., *Exciton Transport, Charge Extraction, and Loss Mechanisms in Organic Photovoltaics*. ProQuest: 2009; p 133
32. Brabec, C. J., *Organic photovoltaics: concepts and realization*. Springer: 2003; p 297.
33. Litton, C. W.; Collins, T. C.; Reynolds, D. C.; Capper, P.; Kasap, S.; Willoughby, A., *Zinc Oxide Materials for Electronic and Optoelectronic Device Applications*. John Wiley and Sons: 2011; p 386.
34. Hains, A. W.; Liang, Z. Q.; Woodhouse, M. A.; Gregg, B. A. *Chemical Reviews* **2010**, 110, (11), 6689-6735.
35. Hoppe, H.; Sariciftci, N. S. *Journal of Materials Research* **2004**, 19, (7), 1924-1945.
36. Park, S. H.; Roy, A.; Beaupre, S.; Cho, S.; Coates, N.; Moon, J. S.; Moses, D.; Leclerc, M.; Lee, K.; Heeger, A. J. *Nature Photonics* **2009**, 3, (5), 297-U5.
37. He, Z.; Zhong, C.; Su, S.; Xu, M.; Wu, H.; Cao, Y. *Nature Photonics* **2012**, 6, (9), 593-597.
38. Brabec, C. J.; Cravino, A.; Meissner, D.; Sariciftci, N. S.; Rispiens, M. T.; Sanchez, L.; Hummelen, J. C.; Fromherz, T. *Thin Solid Films* **2002**, 403, 368-372.
39. Potscavage, W. J.; Sharma, A.; Kippelen, B. *Accounts of Chemical Research* **2009**, 42, (11), 1758-1767.
40. Vandewal, K.; Tvingstedt, K.; Gadisa, A.; Inganäs, O.; Manca, J. V. *Nature Materials* **2009**, 8, (11), 904-909.
41. Credgington, D.; Hamilton, R.; Atienzar, P.; Nelson, J.; Durrant, J. R. *Advanced Functional Materials* **2011**, 21, (14), 2744-2753.
42. Kippelen, B.; Bredas, J. L. *Energy & Environmental Science* **2009**, 2, (3), 251-261.
43. Snaith, H. J. *Nature Photonics* **2012**, 6, (6), 337-340.
44. <http://rredc.nrel.gov/solar/spectra/am1.5>
45. Vogel, M.; Doka, S.; Breyer, C.; Lux-Steiner, M. C.; Fostiropoulos, K. *Applied Physics Letters* **2006**, 89, (16), -.
46. Brabec, C. J.; Shaheen, S. E.; Winder, C.; Sariciftci, N. S.; Denk, P. *Applied Physics Letters* **2002**, 80, (7), 1288-1290.
47. Chang, C. C.; Lin, C. F.; Chiou, J. M.; Ho, T. H.; Tai, Y.; Lee, J. H.; Chen, Y. F.; Wang, J. K.; Chen, L. C.; Chen, K. H. *Applied Physics Letters* **2010**, 96, (26).

48. Steim, R.; Kogler, F. R.; Brabec, C. J. *Journal of Materials Chemistry* **2010**, 20, (13), 2499-2512.
49. Kuhnke, K.; Becker, R.; Epple, M.; Kern, R. *Physical Review Letters* **1997**, 79, (17), 3246-3249.
50. Hung, L. S.; Tang, C. W.; Mason, M. G. *Applied Physics Letters* **1997**, 70, (2), 152-154.
51. Peumans, P.; Bulovic, V.; Forrest, S. R. *Applied Physics Letters* **2000**, 76, (19), 2650-2652.
52. Cao, Y.; Yu, G.; Zhang, C.; Menon, R.; Heeger, A. J. *Synthetic Metals* **1997**, 87, (2), 171-174.
53. Pettersson, L. A. A.; Roman, L. S.; Inganas, O. *Journal of Applied Physics* **1999**, 86, (1), 487-496.
54. Hiramoto, M.; Fujiwara, H.; Yokoyama, M. *Applied Physics Letters* **1991**, 58, (10), 1062-1064.
55. Hiramoto, M.; Fujiwara, H.; Yokoyama, M. *Journal of Applied Physics* **1992**, 72, (8), 3781-3787.
56. Hiramoto, M.; Suezaki, M.; Yokoyama, M. *Chemistry Letters* **1990**, (3), 327-330.
57. Sista, S.; Hong, Z. R.; Chen, L. M.; Yang, Y. *Energy & Environmental Science* **2011**, 4, (5), 1606-1620.
58. Yakimov, A.; Forrest, S. R. *Applied Physics Letters* **2002**, 80, (9), 1667-1669.
59. Heliatek achieves new world record for organic solar cells with certified 9.8% cell efficiency.
<http://www.heliatek.com>
60. Dou, L.; You, J.; Yang, J.; Chen, C.-C.; He, Y.; Murase, S.; Moriarty, T.; Emery, K.; Li, G.; Yang, Y. *Nature Photonics* **2012**, 6, (3), 180-185.
61. Kim, J. Y.; Lee, K.; Coates, N. E.; Moses, D.; Nguyen, T. Q.; Dante, M.; Heeger, A. J. *Science* **2007**, 317, (5835), 222-225.
62. Xue, J. G.; Uchida, S.; Rand, B. P.; Forrest, S. R. *Applied Physics Letters* **2004**, 85, (23), 5757-5759.
63. King, R. R. *Nature Photonics* **2008**, 2, (5), 284-286.
64. Shockley, W.; Queisser, H. J. *Journal of Applied Physics* **1961**, 32, (3), 510-&.
65. Ameri, T.; Dennler, G.; Lungenschmied, C.; Brabec, C. J. *Energy & Environmental Science* **2009**, 2, (4), 347-363.
66. Devos, A. *Journal of Physics D-Applied Physics* **1980**, 13, (5), 839-846.
67. Riede, M.; Uhrich, C.; Widmer, J.; Timmreck, R.; Wynands, D.; Schwartz, G.; Gnehr, W. M.; Hildebrandt, D.; Weiss, A.; Hwang, J.; Sundarraj, S.; Erk, P.; Pfeiffer, M.; Leo, K. *Advanced Functional Materials* **2011**, 21, (16), 3019-3028.
68. Li, G.; Zhu, R.; Yang, Y. *Nature Photonics* **2012**, 6, (3), 153-161.
69. Rand, B. P.; Genoe, J.; Heremans, P.; Poortmans, J. *Progress in Photovoltaics* **2007**, 15, (8), 659-676.
70. Spanggaard, H.; Krebs, F. C. *Solar Energy Materials and Solar Cells* **2004**, 83, (2-3), 125-146.
71. Kearns, D.; Calvin, M. *Journal of Chemical Physics* **1958**, 29, (4), 950-951.
72. Delacote, G.; Schott, M. *Physica Status Solidi* **1962**, 2, (11), 1460-1465.
73. Fitzner, R.; Mena-Osteritz, E.; Mishra, A.; Schulz, G.; Reinold, E.; Weil, M.; Korner, C.; Ziehlke, H.; Elschner, C.; Leo, K.; Riede, M.; Pfeiffer, M.; Uhrich, C.; Bauerle, P. *Journal of the American Chemical Society* **2012**, 134, (27), 11064-11067.

74. Sun, Y. M.; Welch, G. C.; Leong, W. L.; Takacs, C. J.; Bazan, G. C.; Heeger, A. J. *Nature Materials* **2012**, 11, (1), 44-48.
75. van der Poll, T. S.; Love, J. A.; Nguyen, T. Q.; Bazan, G. C. *Advanced Materials* **2012**, 24, (27), 3646-3649.
76. Heutz, S.; Sullivan, P.; Sanderson, B. M.; Schultes, S. M.; Jones, T. S. *Solar Energy Materials and Solar Cells* **2004**, 83, (2-3), 229-245.
77. Pandey, R.; Holmes, R. J. *Advanced Materials* **2010**, 22, (46), 5301-5305.
78. Pfuetzner, S.; Meiss, J.; Petrich, A.; Riede, M.; Leo, K. *Applied Physics Letters* **2009**, 94, (25), -.
79. Wynands, D.; Levichkova, M.; Leo, K.; Uhrich, C.; Schwartz, G.; Hildebrandt, D.; Pfeiffer, M.; Riede, M. *Applied Physics Letters* **2010**, 97, (7).
80. Kaji, T.; Zhang, M. L.; Nakao, S.; Iketaki, K.; Yokoyama, K.; Tang, C. W.; Hiramoto, M. *Advanced Materials* **2011**, 23, (29), 3320-+.
81. Peumans, P.; Uchida, S.; Forrest, S. R. *Nature* **2003**, 425, (6954), 158-162.
82. Beverina, L.; Salice, P. *European Journal of Organic Chemistry* **2010**, (7), 1207-1225.
83. Riede, M.; Mueller, T.; Tress, W.; Schueppel, R.; Leo, K. *Nanotechnology* **2008**, 19, (42), -.
84. Xue, J. G.; Uchida, S.; Rand, B. P.; Forrest, S. R. *Applied Physics Letters* **2004**, 84, (16), 3013-3015.
85. Chiu, S. W.; Lin, L. Y.; Lin, H. W.; Chen, Y. H.; Huang, Z. Y.; Lin, Y. T.; Lin, F.; Liu, Y. H.; Wong, K. T. *Chemical Communications* **2012**, 48, (13), 1857-1859.
86. Fitzner, R.; Reinold, E.; Mishra, A.; Mena-Osteritz, E.; Ziehlke, H.; Korner, C.; Leo, K.; Riede, M.; Weil, M.; Tsaryova, O.; Weiss, A.; Uhrich, C.; Pfeiffer, M.; Bauerle, P. *Advanced Functional Materials* **2011**, 21, (5), 897-910.
87. Lin, L. Y.; Chen, Y. H.; Huang, Z. Y.; Lin, H. W.; Chou, S. H.; Lin, F.; Chen, C. W.; Liu, Y. H.; Wong, K. T. *Journal of the American Chemical Society* **2011**, 133, (40), 15822-15825.
88. Steinmann, V.; Kronenberg, N. M.; Lenze, M. R.; Graf, S. M.; Hertel, D.; Meerholz, K.; Burckstummer, H.; Tulyakova, E. V.; Wurthner, F. *Advanced Energy Materials* **2011**, 1, (5), 888-893.
89. Lin, L. Y.; Lu, C. W.; Huang, W. C.; Chen, Y. H.; Lin, H. W.; Wong, K. T. *Organic Letters* **2011**, 13, (18), 4962-4965.
90. Steinberger, S.; Mishra, A.; Reinold, E.; Muller, C. M.; Uhrich, C.; Pfeiffer, M.; Bauerle, P. *Organic Letters* **2011**, 13, (1), 90-93.
91. Walker, B.; Kim, C.; Nguyen, T. Q. *Chemistry of Materials* **2011**, 23, (3), 470-482.
92. Brabec, C. J.; Gowrisanker, S.; Halls, J. J. M.; Laird, D.; Jia, S. J.; Williams, S. P. *Advanced Materials* **2010**, 22, (34), 3839-3856.
93. Anthony, J. E. *Chemistry of Materials* **2011**, 23, (3), 583-590.
94. Zhou, Y.; Ding, L.; Shi, K.; Dai, Y. Z.; Ai, N.; Wang, J.; Pei, J. *Advanced Materials* **2012**, 24, (7), 957.

95. Benning, P. J.; Poirier, D. M.; Ohno, T. R.; Chen, Y.; Jost, M. B.; Stepniak, F.; Kroll, G. H.; Weaver, J. H.; Fure, J.; Smalley, R. E. *Physical Review B* **1992**, 45, (12), 6899-6913.
96. He, Y.; Li, Y. *Physical Chemistry Chemical Physics* **2011**, 13, (6), 1970-1983.
97. Dennler, G.; Scharber, M. C.; Brabec, C. J. *Advanced Materials* **2009**, 21, (13), 1323-1338.
98. Cardona, C. M.; Elliott, B.; Echegoyen, L. *Journal of the American Chemical Society* **2006**, 128, (19), 6480-6485.
99. Dunsch, L.; Yang, S. *Small* **2007**, 3, (8), 1298-1320.
100. Ross, R. B.; Cardona, C. M.; Guldi, D. M.; Sankaranarayanan, S. G.; Reese, M. O.; Kopidakis, N.; Peet, J.; Walker, B.; Bazan, G. C.; Van Keuren, E.; Holloway, B. C.; Drees, M. *Nature Materials* **2009**, 8, (3), 208-212.
101. Shirakawa, H.; Louis, E. J.; Macdiarmid, A. G.; Chiang, C. K.; Heeger, A. J. *Journal of the Chemical Society-Chemical Communications* **1977**, (16), 578-580.
102. Facchetti, A. *Chemistry of Materials* **2011**, 23, (3), 733-758.
103. Cowie, J. M. G.; Arrighi, V., *Polymers: Chemistry and Physics of Modern Materials*. CRC Press: 2008; p 499.
104. Rubinstein, M.; Colby, R. H., *Polymer Physics* Oxford University Press, USA 2003; p 454.
105. Chua, L. L.; Zaumseil, J.; Chang, J. F.; Ou, E. C. W.; Ho, P. K. H.; Sirringhaus, H.; Friend, R. H. *Nature* **2005**, 434, (7030), 194-199.
106. Fichou, D., *Handbook of Oligo- and Polythiophenes*. John Wiley & Sons: 2008; p 558.
107. Sirringhaus, H.; Tessler, N.; Friend, R. H. *Synthetic Metals* **1999**, 102, (1-3), 857-860.
108. Prosa, T. J.; Winokur, M. J.; Moulton, J.; Smith, P.; Heeger, A. J. *Macromolecules* **1992**, 25, (17), 4364-4372.
109. Mccullough, R. D.; Tristramnagle, S.; Williams, S. P.; Lowe, R. D.; Jayaraman, M. *Journal of the American Chemical Society* **1993**, 115, (11), 4910-4911.
110. Yamamoto, T.; Komarudin, D.; Arai, M.; Lee, B. L.; Suganuma, H.; Asakawa, N.; Inoue, Y.; Kubota, K.; Sasaki, S.; Fukuda, T.; Matsuda, H. *Journal of the American Chemical Society* **1998**, 120, (9), 2047-2058.
111. Yang, C.; Orfino, F. P.; Holdcroft, S. *Macromolecules* **1996**, 29, (20), 6510-6517.
112. Kim, Y.; Cook, S.; Tuladhar, S. M.; Choulis, S. A.; Nelson, J.; Durrant, J. R.; Bradley, D. D. C.; Giles, M.; McCulloch, I.; Ha, C. S.; Ree, M. *Nature Materials* **2006**, 5, (3), 197-203.
113. Sirringhaus, H.; Brown, P. J.; Friend, R. H.; Nielsen, M. M.; Bechgaard, K.; Langeveld-Voss, B. M. W.; Spiering, A. J. H.; Janssen, R. A. J.; Meijer, E. W.; Herwig, P.; de Leeuw, D. M. *Nature* **1999**, 401, (6754), 685-688.
114. Kline, R. J.; McGehee, M. D.; Kadnikova, E. N.; Liu, J. S.; Frechet, J. M. J. *Advanced Materials* **2003**, 15, (18), 1519-+.

115. Gadisa, A.; Oosterbaan, W. D.; Vandewal, K.; Bolsee, J. C.; Bertho, S.; D'Haen, J.; Lutsen, L.; Vanderzande, D.; Manca, J. V. *Advanced Functional Materials* **2009**, 19, (20), 3300-3306.
116. Schilinsky, P.; Waldauf, C.; Brabec, C. J. *Applied Physics Letters* **2002**, 81, (20), 3885-3887.
117. Padinger, F.; Rittberger, R. S.; Sariciftci, N. S. *Advanced Functional Materials* **2003**, 13, (1), 85-88.
118. Wu, W. R.; Jeng, U. S.; Su, C. J.; Wei, K. H.; Su, M. S.; Chiu, M. Y.; Chen, C. Y.; Su, W. B.; Su, C. H.; Su, A. C. *Acs Nano* **2011**, 5, (8), 6233-6243.
119. Chen, D. A.; Nakahara, A.; Wei, D. G.; Nordlund, D.; Russell, T. P. *Nano Letters* **2011**, 11, (2), 561-567.
120. Chen, W.; Xu, T.; He, F.; Wang, W.; Wang, C.; Strzalka, J.; Liu, Y.; Wen, J. G.; Miller, D. J.; Chen, J. H.; Hong, K. L.; Yu, L. P.; Darling, S. B. *Nano Letters* **2011**, 11, (9), 3707-3713.
121. Schmidt-Hansberg, B.; Sanyal, M.; Klein, M. F. G.; Pfaff, M.; Schnabel, N.; Jaiser, S.; Vorobiev, A.; Muller, E.; Colsmann, A.; Scharfer, P.; Gerthsen, D.; Lemmer, U.; Barrena, E.; Schabel, W. *Acs Nano* **2011**, 5, (11), 8579-8590.
122. Vaynzof, Y.; Kabra, D.; Zhao, L. H.; Chua, L. L.; Steiner, U.; Friend, R. H. *Acs Nano* **2011**, 5, (1), 329-336.
123. Yin, W.; Dadmun, M. *Acs Nano* **2011**, 5, (6), 4756-4768.
124. Dang, M. T.; Hirsch, L.; Wantz, G. *Advanced Materials* **2011**, 23, (31), 3597-3602.
125. Liang, Y. Y.; Yu, L. P. *Polymer Reviews* **2010**, 50, (4), 454-473.
126. Bishop, C., *Roll-to-Roll Vacuum Deposition of Barrier Coatings*. Wiley-Scrivener: 2010; p 262.
127. Brabec, C. J. *Solar Energy Materials and Solar Cells* **2004**, 83, (2-3), 273-292.
128. Forrest, S. R. *Nature* **2004**, 428, (6986), 911-918.
129. Ludwig, R.; Kukla, R.; Josephson, E. *Proceedings of the Ieee* **2005**, 93, (8), 1483-1490.
130. Gritsenko, K. P.; Krasovsky, A. M. *Chemical Reviews* **2003**, 103, (9), 3607-3649.
131. Komakine, M.; Namikawa, T.; Yamazaki, Y. *Makromolekulare Chemie-Rapid Communications* **1986**, 7, (3), 139-142.
132. Yamamoto, T.; Wakayama, H.; Fukuda, T.; Kanbara, T. *Journal of Physical Chemistry* **1992**, 96, (22), 8677-8679.
133. Miyashita, K.; Kaneko, M. *Synthetic Metals* **1995**, 68, (2), 161-165.
134. Kobayashi, S.; Haga, Y. *Synthetic Metals* **1997**, 87, (1), 31-36.
135. Lee, C. H.; Kang, G. W.; Jeon, J. W.; Song, W. J.; Seoul, C. *Thin Solid Films* **2000**, 363, (1-2), 306-309.
136. Masui, H.; Takeuchi, M. *Japanese Journal of Applied Physics Part 2-Letters* **1991**, 30, (5A), L864-L866.
137. Roncali, J.; Leriche, P.; Cravino, A. *Advanced Materials* **2007**, 19, (16), 2045-2060.
138. Brown, C. E.; Kovacic, P.; Wilkie, C. A.; Cody, R. B.; Kinsinger, J. A. *Journal of Polymer Science Part C-Polymer Letters* **1985**, 23, (9), 453-463.

139. Song, W. J.; Seoul, C.; Kang, G. W.; Lee, C. *Synthetic Metals* **2000**, 114, (3), 355-359.
140. Lee, C. H.; Kang, G. W.; Jeon, J. W.; Song, W. J.; Kim, S. Y.; Seoul, C. *Synthetic Metals* **2001**, 117, (1-3), 75-79.
141. Touihri, S.; Safoula, G.; Bernede, J. C.; Leny, R.; Alimi, K. *Thin Solid Films* **1997**, 304, (1-2), 16-23.
142. Chen, B. J.; Liu, S. Y. *Japanese Journal of Applied Physics Part 1-Regular Papers Short Notes & Review Papers* **1998**, 37, (3B), 1665-1666.
143. Djobo, S. O.; Bernede, J. C.; Marsillac, S. *Synthetic Metals* **2001**, 122, (1), 131-133.
144. Yang, Y.; Westerweele, E.; Zhang, C.; Smith, P.; Heeger, A. J. *Journal of Applied Physics* **1995**, 77, (2), 694-698.
145. D'Almeida, K.; Bernede, J. C.; Marsillac, S.; Godoy, A.; Diaz, F. R. *Synthetic Metals* **2001**, 122, (1), 127-129.
146. Irimia-Vladu, M.; Marjanovic, N.; Vlad, A.; Ramil, A. M.; Hernandez-Sosa, G.; Schwodiauer, R.; Bauer, S.; Sariciftci, N. S. *Advanced Materials* **2008**, 20, (20), 3887-+.
147. Burrows, P. E.; Forrest, S. R.; Sapochak, L. S.; Schwartz, J.; Fenter, P.; Buma, T.; Ban, V. S.; Forrest, J. L. *Journal of Crystal Growth* **1995**, 156, (1-2), 91-98.
148. Rusu, M.; Gasiorowski, J.; Wiesner, S.; Meyer, N.; Heuken, M.; Fostiropoulos, K.; Lux-Steiner, M. C. *Thin Solid Films* **2008**, 516, (20), 7160-7166.
149. Vaeth, K. M.; Jensen, K. F. *Advanced Materials* **1997**, 9, (6), 490-&.
150. Eason, R., *Pulsed Laser Deposition of Thin Films: Applications-led Growth of Functional Materials*. WileyBlackwell 2006; p 682.
151. Antony, R.; Moliton, A.; Ratier, B. *Applied Physics B-Lasers and Optics* **2000**, 71, (1), 33-41.
152. Krebs, F. C.; Tromholt, T.; Jorgensen, M. *Nanoscale* **2010**, 2, (6), 873-886.
153. Dam, H. F.; Krebs, F. C. *Solar Energy Materials and Solar Cells* **2012**, 97, 191-196.
154. Espinosa, N.; Garcia-Valverde, R.; Urbina, A.; Krebs, F. C. *Solar Energy Materials and Solar Cells* **2011**, 95, (5), 1293-1302.
155. Krebs, F. C. *Solar Energy Materials and Solar Cells* **2009**, 93, (4), 465-475.
156. Larsen-Olsen, T. T.; Andreasen, B.; Andersen, T. R.; Bottiger, A. P. L.; Bundgaard, E.; Norrman, K.; Andreasen, J. W.; Jorgensen, M.; Krebs, F. C. *Solar Energy Materials and Solar Cells* **2012**, 97, 22-27.
157. Krebs, F. C.; Jorgensen, M.; Norrman, K.; Hagemann, O.; Alstrup, J.; Nielsen, T. D.; Fyenbo, J.; Larsen, K.; Kristensen, J. *Solar Energy Materials and Solar Cells* **2009**, 93, (4), 422-441.
158. Hoth, C. N.; Choulis, S. A.; Schilinsky, P.; Brabec, C. J. *Advanced Materials* **2007**, 19, (22), 3973.
159. Aernouts, T.; Aleksandrov, T.; Girotto, C.; Genoe, J.; Poortmans, J. *Applied Physics Letters* **2008**, 92, (3), -.
160. Nielsen, T. D.; Cruickshank, C.; Foged, S.; Thorsen, J.; Krebs, F. C. *Solar Energy Materials and Solar Cells* **2010**, 94, (10), 1553-1571.

CHAPTER 2 - MATERIALS AND METHODS

This section discusses the experimental methods used during the course of the research. More details on specific experiments are provided in the relevant chapters.

2.1 Materials

Poly(3-hexylthiophene) (P3HT) was purchased from Rieke Metals. The molecular weight (M_w) was measured using gel permeation chromatography (GPC) and was found to be approximately $M_w = 36300 \text{ gmol}^{-1}$ with respect to polystyrene standards. The regio-regularity of the polymer was reported by the manufacturer to be 90%.

Poly(thiophene) (PTh) was supplied by Sigma Aldrich and its M_w was not measured as it did not dissolve in chloroform or tetrahydrofuran, the mobile phases of the GPC. The value of M_w was not specified by the manufacturer either.

Poly(3,4-ethylenedioxythiophene)-poly(styrenesulfonate) (PEDOT:PSS, Baytron P dispersion) was supplied by H.C. Starck, and *Fullerene C₆₀* (99.9% pure) by MER Corporation.

All the materials were used as received.

2.2 Polymer evaporation

P3HT was deposited by vacuum thermal evaporation from a tungsten boat (7 x 32 mm, supplied by Leybold Optics) which was heated by a Xantrex XHR 7.5-80 DC Power Supply. The boat temperature was measured using a K-type exposed thermocouple mounted inside the boat. For chemical characterisation, P3HT was evaporated at a temperature of 370 ± 5 °C and 380 ± 5 °C at a rate of ~ 0.75 nm/min, and 420 ± 5 °C at a rate of 1.5-2 nm/min. For photovoltaic device fabrication, P3HT was evaporated at a temperature of 415 ± 10 °C at a rate of ~ 1.5 nm/min.

PTh deposition was conducted from a larger tungsten boat (13 x 51 mm, supplied by Testbourne Ltd) heated by a Xantrex XHR 7.5-80 DC Power Supply. An additional TDK-Lambda Genesys 8-300 DC Power Supply was used for co-evaporation of the polymer and C₆₀. For chemical characterisation, PTh was evaporated at a temperature of 275 ± 5 °C at a rate of 0.75-1 nm/min, and 300 ± 10 °C at a rate of ~ 1.5 nm/min. For photovoltaic device fabrication, PTh was evaporated at selected temperatures in the range $285-315 \pm 10$ °C at rates between 1-15 nm/min depending on the experiment. For sequential PTh and C₆₀ deposition, PTh was evaporated at a temperature of 300 ± 10 °C at a rate of 0.75-2 nm/min.

C₆₀ was sublimed at selected temperatures in the range $580-610 \pm 15$ °C at rates between 3-30 nm/min depending on the experiment. For sequential PTh and C₆₀ deposition, PTh was evaporated at a temperature of 590 ± 15 °C at a rate of ~ 5 nm/min. 6T was evaporated at a temperature of 220 ± 10 °C at a rate of 0.8-1.2 nm/min.

For PTh and C₆₀ co-deposition in *sections 5.2-5.6*, the evaporation rates and their relative ratio were fixed in each experiment which in turn determined the individual evaporation temperatures. Approximate evaporation/sublimation parameters were as follows:

blend	DR _{PTh} [nm/min]	T _{PTh} [°C]	DR _{C₆₀} [nm/min]	T _{C₆₀} [°C]
20% PTh : 80% C ₆₀	2 ± 1	280 ± 5	25 ± 6	610 ± 15
40% PTh : 60% C ₆₀	5 ± 2	290 ± 5	15 ± 5	600 ± 13
60% PTh : 40% C ₆₀	8 ± 4	300 ± 8	8 ± 3	590 ± 10
80% PTh : 20% C ₆₀	11 ± 5	310 ± 10	5 ± 2	580 ± 10

The material evaporation was conducted in high vacuum 10⁻⁴-10⁻⁵ Torr. The vacuum system was modified during the course of research. The main modifications involved change of the bell-jar sealing ring, removal of the sealing grease, and change of the vacuum pumps and various vacuum parts. Experiments conducted before the final modifications included: NMR studies of P3HT, GPC studies of P3HT (both *section 3.2*) and pinhole studies in P3HT thin films (*section 3.4*).

Schematic drawing of the experimental setup for vacuum thermal evaporation is identical to the one illustrated in Figure 12, *section 1.4.2*. Alternating heterojunctions (AHJ) in *section 5.7* were deposited by setting the deposition rates of PTh and C₆₀ constant, and alternatively shielding the individual sources by a shutter.

2.3 Polymer characterisation

Thermogravimetric Analysis (TGA)

TGA is a thermoanalytical technique that measures changes in weight of a sample as a function of temperature. It is commonly used to study thermal decomposition of polymeric materials. The stability of a polymer can be evaluated from the onset temperature of decomposition. Thermal stability of P3HT was measured by Perkin Elmer Pyris Diamond TG/DTA 6300 under N₂ atmosphere between 30-850 °C at a rate of 10 °C/min, and PTh between 25-800 °C at a rate of 10 °C/min. The onset of degradation was estimated as shown in Figure 1b (*section 3.2*) and Figure 5a (*section 3.3*). The measurements were performed with the help of Mr Richard Turner.

Differential Scanning Calorimetry (DSC)

DSC is a thermoanalytical technique that measures heat flow associated with thermal transitions in a material. It is widely used to characterise phase transitions of polymers, such as melting and crystallisation, or the glass transition. Endothermic processes (e.g. melting) require higher heat flow to increase the temperature of the polymer, while exothermic processes (e.g. crystallisation) require lower heat flow to increase the temperature of the polymer. DSC analysis of starting P3HT was measured by Perkin Elmer Diamond DSC between -60 °C and 280 °C at a rate of 300 °C/min. DSC of starting PTh was measured between -60 °C and 225 °C at rates of 100 °C and 300 °C/min. The phase transitions were estimated as shown in Figure 1a (*section 3.2*) and Figure 5b (*section 3.3*). The measurements were performed with the help of Mr Richard Turner.

Differential Thermal Analysis (DTA)

DTA is a thermoanalytical technique similar to DSC. It is often coupled with TGA in order to provide information on both mass loss and thermal transitions simultaneously. DTA analysis of P3HT was measured by Perkin Elmer Pyris Diamond TG/DTA 6300 under N₂ atmosphere between 30-850 °C at a rate of 10 °C/min, and PTh between 25-800 °C at a rate of 10 °C/min. The measurements were performed with the help of Mr Richard Turner.

Gel Permeation Chromatography (GPC)

GPC is a size exclusion chromatography that separates analytes based on their hydrodynamic volume. It is a technique regularly used for determination of the molecular weight (M_w) of polymers. The polymer dissolved in the mobile phase passes through a column packed with porous beads. Its molecular weight is estimated from comparison of its retention time against calibration standards. GPC of the starting and evaporated P3HT and PTh was carried out using PLgel 5 μ m Mixed-D columns (2 x 300 mm length, 7.5 mm diameter) from Polymer Laboratories. The calibration was performed using polystyrene narrow standards ($M_p = 1300$ to 11.2×10^6 g mol^{-1} for P3HT, and $M_p = 580$ to 3.7×10^5 g mol^{-1} for PTh) in tetrahydrofuran (THF) with toluene as the flow marker, detecting at 254 nm. The THF was degassed with helium and pumped at a rate of 1 mL/min at 40.0 °C. Solutions of the starting polymers were made by dissolving materials directly in THF. Solutions of the evaporated polymers were prepared by depositing P3HT/PTh onto a series of cleaned glass-slides and subsequent dissolution of the polymer films in THF. GPC characterisation was conducted in cooperation with the Chemistry Research Laboratory of the Department of Chemistry, University of Oxford (with the help of Dr Giuseppe Sforzini and Dr Jonathan Matichak).

UV-Vis Spectroscopy (UV-Vis)

UV-Vis is an absorption spectroscopy in ultraviolet-visible spectral region. Providing information about structural and electronic properties of a material, it can be used for determination of the band-gap, evidence of crystallinity, and estimation of the relative molecular weight of different polymer fractions. UV-Vis of the polymer samples was performed on an Agilent Cary 5000 spectrometer. Polymeric solutions were prepared in the same way as for GPC characterisation, with chloroform as a solvent (as with THF, PTh could only be partially dissolved in chloroform). All samples were measured against a chloroform solvent reference. Absorption of the polymer thin films deposited on ITO-on-glass was measured against an ITO-on glass reference.

Fourier Transform Infrared Spectroscopy (FT-IR)

The absorption spectrum of polymers in the infrared region can be obtained from FT-IR. This technique measures the fundamental vibrations of organic molecules. The chemical structure of the molecule can be identified based on absorption of infrared radiation by its chemical bonds. FT-IR can be used for quantitative analysis as the strength of the absorption is proportional to the concentration of the modes and can be used, for example, to give an estimation of the conjugation length of a polymer. FT-IR of P3HT and PTh was performed using a Varian UMA-600 spectrometer. Infrared spectra of the polymers were measured with an attenuated total reflectance extension on the spectrometer. Samples were prepared as chloroform solutions using methods described in the GPC section. The solutions were cast onto a diamond crystal window to yield a dry sample once the background solvent evaporated away.

Nuclear Magnetic Resonance Spectroscopy (NMR)

NMR is a technique widely used to determine the chemical structure of organic molecules. Its most common version, ^1H NMR, identifies position of hydrogen atoms contained in the molecule and thus describes its detailed structure. P3HT samples for proton NMR were prepared as described in the GPC section. Deuterated chloroform was used as a solvent. NMR spectra were recorded on a Bruker DPX 400 MHz at 298 K. This was done in cooperation with the Chemistry Research Laboratory of the Department of Chemistry, University of Oxford (with the help of Dr Giuseppe Sforazzini).

2.4 Thin-film characterisation

Phase-shift Interferometric Optical Profilometry (MicroXAM)

MicroXAM measures phase shifts of light reflected from the sample to provide non-contact mapping of its surface. The lateral resolution is $\sim 1\ \mu\text{m}$ and the vertical resolution $\sim 1\ \text{nm}$. The surface topography of the vacuum-deposited thin films was imaged by Omniscan MircoXAM 5000B ADE Phase Shift profiler.

Standard optical microscopy mode was used to determine the surface fraction of the spits in Figure 10, *section 3.4*. A number of optical images (>8) across each of two samples for each experiment was used. Image processing and the data calculation were done using ImageJ open source software.

Atomic Force Microscopy (AFM)

AFM is a high-resolution type of scanning probe microscopy which detects deflections of a laser beam reflected from the back surface of a cantilever moving over the sample surface. The lateral resolution is <10 nm and the vertical resolution <1 nm. Besides the surface topography, AFM provides information about the phase shift of the oscillating cantilever. This can be directly correlated with the viscoelastic response of the tip-surface interaction which can thus be spatially imaged. The scans of the thin films were obtained using a Park Scientific Instruments AutoProbe CP microscope in tapping mode (intermittent-contact mode).

Scans from several different locations were acquired for each sample and only representative images were used. RMS roughness data were obtained from specially conducted measurements of more than three $5 \times 5 \mu\text{m}$ areas. Since the presence of a 'capping' metal electrode is crucial in the development of bulk heterojunction morphology during annealing^{1, 2}, the topographic and phase AFM images in *section 5.5* were done on actual active pixels of the devices by carefully peeling the Al electrode off³⁻⁵. No cathode interface layer was used.

Processing and analysis of the MicroXAM and AFM surface images (including RMS, Peak-to-Peak distance and Kurtosis values) was done in Gwyddion open source software. The Peak-to-Peak distance in Figure 8b, *section 5.5*, was averaged from 20 different surface profiles across the shown AFM topographic scans.

DEKTAK Surface Profilometry

DEKTAK is a surface contact measurement technique in which a step height can be measured using a stylus dragged across the surface. Its vertical resolution is <1 nm and therefore it is commonly used for thickness measurements of thin films. The thickness of the vacuum-deposited thin films was measured using Veeco DEKTAK 6M Stylus Profiler. The scanning line ranged from top of the Al electrode to the ITO electrode. The thickness of the Al electrode film was used as a reference to the thickness of the organic thin film.

X-Ray Diffractometry (XRD)

XRD is used to determine crystal structure of materials. X-Ray radiation diffracted from the crystal lattice relates diffraction angle to the lattice spacing through the Bragg's law

$$n\lambda = 2d \sin \theta \quad (1)$$

where n is an integer, λ is the wavelength of incident wave, d is the spacing between the planes in the lattice, and θ is the angle between the incident beam and the scattering planes. The degree of crystallinity, size and orientation of crystals can be obtained. XRD of the organic thin films was performed on a Philips PW1820 system with PW1727 X-ray generator using Cu K α radiation ($\lambda = 1.5418 \text{ \AA}$). The scanning speed was approximately 15 min/1°. The thin films were deposited on silicon wafer substrates using the process described above. The evaporation temperatures were the same ones as for the device fabrication. The film thickness was approximately 0.2-0.5 μm for both PTh and P3HT, a thicker PTh film of $\sim 1 \mu\text{m}$ was used for the trace in the inset of Figure 3c, *section 5.2*.

Transmission Electron Microscopy (TEM)

TEM is a high-resolution microscopy technique in which a beam of electrons passes through a thin specimen to determine its structure. It can provide absorption contrast images (bright-field), phase contrast images (high-resolution mode) and diffraction patterns (on back focal plane) to determine morphology and crystalline structure of the material. TEM analysis of the polymer thin films was performed on a JEOL-JEM 4000EX LaB6 microscope with an information limit of 0.12 nm at an accelerating voltage of 100 keV. The microscope was calibrated using lead sulphide (PbS) nanocrystals with well-defined lattice spacings. Samples were prepared by taking a polymer film deposited on PEDOT and placing it in de-ionised water for 24 hours. Once the PEDOT was dissolved, the polymer film floated off and was mounted on 400 mesh copper TEM grid. The measurements were performed with the help of Dr Andrew Watt.

2.5 Photovoltaic device fabrication

Photovoltaic devices were prepared by deposition of an active layer in between an Al cathode and an ITO anode, as shown in Figure 2. The anode was obtained by etching a 2 mm wide stripe of ITO from a rectangular ITO-on-glass substrate (12 x 14 mm) with the thickness of ~100 nm and sheet resistance ~10 Ω /square. The ITO surface was cleaned with de-ionised water, and acetone and isopropanol both heated to ~50 °C. The substrate was then treated with oxygen plasma for 1 minute (Tegal Plasmod).

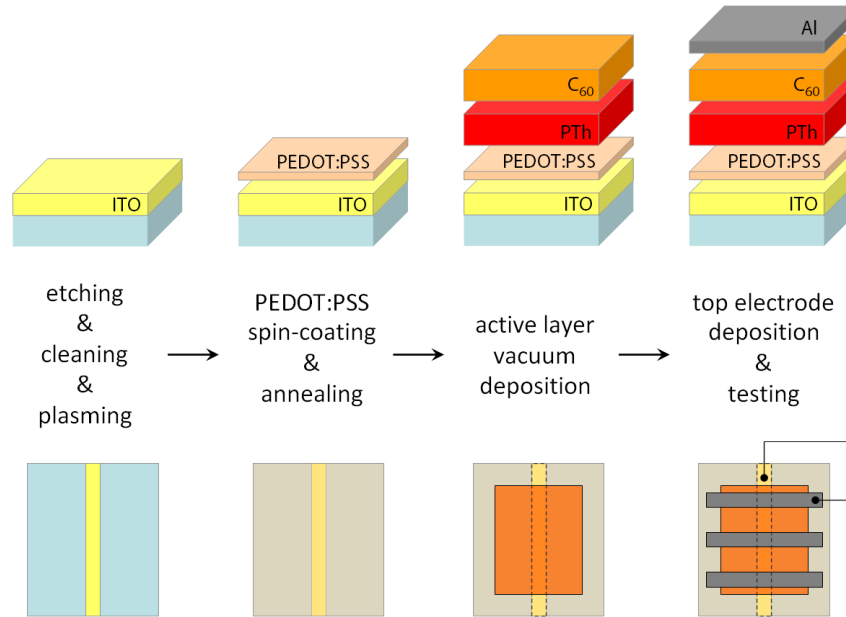


Figure 2. Procedure of the photovoltaic sample fabrication.

Next, a layer of PEDOT:PSS was spin coated at 5000 rpm for 30 seconds onto the prepared ITO surface and then heated for 5 min at 140 °C. The deposition of the active layer followed as described in the *section 2.2*. The active layer thickness was controlled in-situ using a quartz crystal microbalance (Q-Pod, Inficon) placed at the same distance from the source as the substrates (approximately 15 cm). A mechanical shutter was used to shield the substrate from evaporated material before the desired boat temperature was reached. After the deposition, the thickness value was further verified by DEKTAK surface profiler (Veeco Dektak 6M Stylus Profiler). Finally, a set of 80 nm thick and 1.1 mm wide Al electrodes was evaporated on top of the sandwich structure. The active cell area was 2.2 mm².

The thermal treatment was performed on fully completed devices (including the top electrode). The devices were annealed on a hotplate placed in a nitrogen glove-box operating at 20-100 ppm O₂ and 30-70 ppm H₂O. The annealing parameters varied according to experiments.

2.6 Photovoltaic device characterisation

Measurement of the current and voltage photo-generated by the solar cell leads to the essential J - V characteristic of the device. Photovoltaic characterisation was carried out under white light illumination (AM1.5, 100 mWcm⁻²) in an inert N₂ atmosphere. The incident light was generated by a Newport 67005 solar simulator and the light intensity at the sample position was determined with a microprocessor-based power meter Thermo-Oriel Instruments (calibrated according to ASTM standards). A set of neutral ND Melles Griot filters were used for varying the illumination intensity. Current-voltage characteristics were measured using a Keithley 2400 SourceMeter measurement unit.

The main photovoltaic parameters (J_{sc} , V_{oc} , FF and PCE) were obtained from the J - V curves using methods discussed in *section 1.2.4*. The series (R_s) and shunt (R_{sh}) resistances, as well as the reverse saturation current (I_0) and the ideality factor (n), were all extracted directly from the illuminated I - V characteristics using a method described by Ortiz-Conde *et al*⁶. Here, Lambert W function is used to obtain the explicit analytical solutions of the single-diode equation (for each variable I and V)

$$I = I_0 \left(\exp \left(\frac{q(V - R_s I)}{nk_B T} \right) - 1 \right) + \frac{V - R_s I}{R_{sh}} - I_{sc}, \quad (2)$$

where I_0 is the saturation current, R_s the series resistance, R_{sh} the shunt resistance, n the ideality factor, q the elementary charge, k_B the Boltzmann constant and T the temperature. As the resulting analytical expressions remain unsuitable for the purpose of extracting the device parameters, the Co-content function is derived from the expressions and fitted to the experimental I - V data. This eventually leads to the values of R_s , R_{sh} , n and I_0 . The

method is advantageous for its extraction of the parameters directly from the operational 4th quadrant of the illuminated I - V curve, and has a small relative error for a wide range of R_s and R_{sh} .

The external quantum efficiency (EQE) measures the amount of photocurrent generated by the solar cell at a certain wavelength. Therefore, the EQE response integrated over the whole spectrum of wavelengths leads to J_{sc} of the device. The EQE was measured using a halogen lamp and Oriel Cornerstone 130 monochromator. Harmonics were blocked by high-pass 400 and 610 nm cut off filters when illuminating at longer wavelengths. The light intensity was calibrated using a Newport 818-UV enhanced silicon photodetector. The photocurrent of the device was measured with a Keithley 6845 Picoammeter. Since the device active area was too small to focus the incident photons onto the cell, an overall correction factor was applied to the EQE measurements such that the J_{sc} determined from integration matched that of the determined from J - V curve. The correction factor was applied equally to all wavelengths so the shape of the EQE response remained unchanged.

The AM1.5 Spectrum data used in Figure 5b, *section 5.4*, was obtained from the National Renewable Energy Laboratory website (<http://rredc.nrel.gov/solar/spectra/am1.5>). The lower estimate of IQE was done by direct division of the EQE response by the absorption of the sample.

2.7 References

1. Kim, H. J.; Park, J. H.; Lee, H. H.; Lee, D. R.; Kim, J. J. *Organic Electronics* **2009**, 10, (8), 1505-1510.

2. Peumans, P.; Uchida, S.; Forrest, S. R. *Nature* **2003**, 425, (6954), 158-162.
3. Gevorgyan, S. A.; Krebs, F. C. *Chemistry of Materials* **2008**, 20, (13), 4386-4390.
4. Ma, W. L.; Yang, C. Y.; Gong, X.; Lee, K.; Heeger, A. J. *Advanced Functional Materials* **2005**, 15, (10), 1617-1622.
5. Xu, Z.; Chen, L. M.; Yang, G. W.; Huang, C. H.; Hou, J. H.; Wu, Y.; Li, G.; Hsu, C. S.; Yang, Y. *Advanced Functional Materials* **2009**, 19, (8), 1227-1234.
6. Ortiz-Conde, A.; Sanchez, F. J. G.; Muci, J. *Solar Energy Materials and Solar Cells* **2006**, 90, (3), 352-361.

3.1 Introduction

Roll-to-roll processing of conjugated polymers has largely focused upon solution-based printing and coating¹. Vacuum thermal processing of materials is advantageous for its ease of parallel and sequential film deposition², however the high temperature conditions have so far restricted its application to small molecular weight systems³. This chapter presents a simple method for the thermal deposition of polymeric semiconductors poly(3-hexylthiophene) (P3HT) and poly(thiophene) (PTh), examines how their chemical properties are modified on evaporation and explores the influence side groups have on the optical and morphological properties of thin films.

Organic semiconductors used in solar cells fall into two main groups - low molecular weight materials, which are usually deposited in vacuum, and higher molecular weight polymers, which are usually solution processed. Polymer photovoltaics benefit from the freedom of chemical design to produce good light absorbers and donors with adjustable energy levels⁴. In addition, the tendency of polymers to form a favourable phase morphology in heterojunctions with fullerene derivatives has made them key elements of the modern device architectures. The most prolific polymer used in photovoltaics in the past decade has been poly(3-hexylthiophene)⁵. It exhibits one of the best hole-transport properties and when blended with PCBM it has led to some of the highest efficiency organic solar cells^{6,7}.

Vacuum thermal evaporation of large organic molecules already has a long tradition^{8,9} and has been successfully applied to various polymers, mostly polytetrafluoroethylene (TeflonTM) and polyamide (NylonTM) in metal-polymer nanocomposite systems¹⁰⁻¹⁵. Although the main shortcoming is the decrease in molecular weight during the thermal heating, small polymers with up to several 1000s gmol⁻¹, equivalent to 10s of monomeric units, can be deposited⁸ and therefore still possess their long-chain character. This macromolecular character could be beneficial in achieving enhanced control over the phase-separation in vacuum-deposited bulk heterojunctions.

Structural analysis of a thermally evaporated organic polymer semiconductor has been reported by Wei *et al.*¹⁶ who successfully demonstrated that P3HT can withstand such treatment while largely retaining its chemical composition. This chapter examines the vacuum thermal deposition of P3HT and PTh, analyses their structural properties before and after deposition and makes an optical and morphological comparison of the respective polymer thin films. The polymer side groups are shown to have a strong influence on molecular packing in the vacuum-deposited films, as well as on the evaporation process itself. Similar molecular weight and thus higher equivalent degree of conjugation can be obtained for evaporated PTh compared with P3HT, and the deposited molecules are shown to assemble into ordered films with high crystallinity.

3.2 Thermal behaviour and vacuum deposition of P3HT

Thermal behaviour of P3HT was studied using Differential Scanning Calorimetry (DSC) and Thermo-Gravimetric Analysis (TGA) under an N₂ atmosphere at atmospheric pressure, as shown in Figure 1a. DSC identified the glass transition temperature (T_g) to be 130 °C and the melting temperature 230 °C. The melting temperature corresponds well with that determined by Differential Thermal Analysis (DTA), 227 °C. Both values are in agreement with previously published literature^{17, 18}. The onset temperature of polymer degradation is 442 °C and the degradation reaches a plateau of 28% at approximately 510 °C, as measured by TGA (Figure 1b).

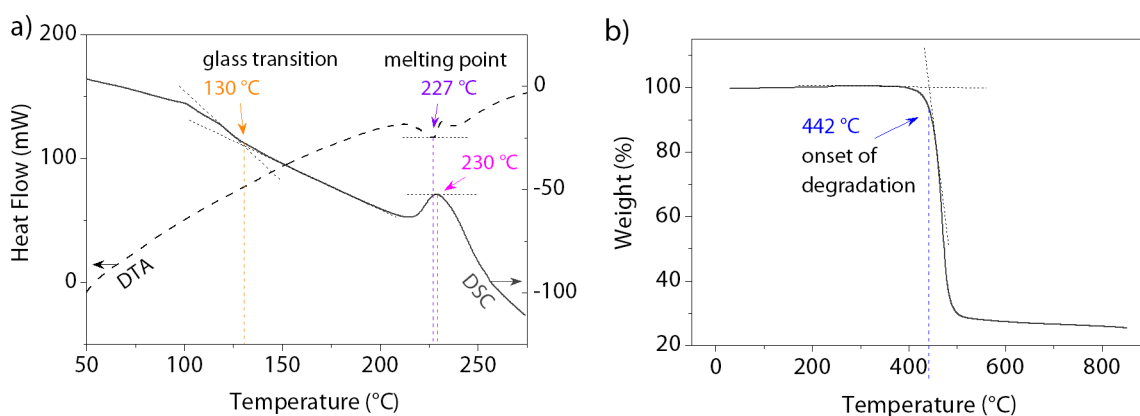


Figure 1. (a) DSC (solid line) and DTA (dotted line) measurements of P3HT thermal behaviour.

(b) Thermal degradation of P3HT as measured by TGA.

To study the influence of temperature on the polymer structure, chemical characterisation was performed on the following samples: P3HT before evaporation (starting) and P3HT evaporated at two different temperatures, 380 °C and 420 °C. It was found from Gel Permeation Chromatography (GPC) that the molecular weight (M_w) of the polymer was reduced during the thermal deposition process. The M_w of P3HT decreased from ~36300 gmol⁻¹ to about 1500 gmol⁻¹ for evaporation temperatures of 370 °C and 420 °C. This

corresponds to a weight of an oligomer with approximately 9 monomer units. The number is also consistent with molecular weight which evaporated polymer fractions of other materials retain during the evaporation process⁸.

Light absorption of P3HT is strongly dependent on its conjugation length and thus molecular weight^{19, 20}. UV-Vis spectroscopy was therefore used to compare absorption spectra of P3HT in solution before and after evaporation. The materials were dissolved in chloroform with respective spectra shown in Figure 2a. Essentially, the absorption peak of the evaporated polymer exhibits a blue shift indicative of molecular weight loss^{19, 20}. The absorption maximum shifts from 452 nm for the starting material to 427 nm and 395 nm for the polymers evaporated at 420 °C and 380 °C, respectively. In accordance with the previous study of P3HT made by Zen *et al.*¹⁹, this suggests that the M_w of the polymer evaporated at 420 °C is higher than that of evaporated at 380 °C. This means that rather than increased degradation at the higher temperature, an elevated temperature results in the evaporation of larger molecular fractions (i.e. those with greater vaporisation temperature). The decrease in the M_w observed from UV-Vis is consistent with the GPC measurements.

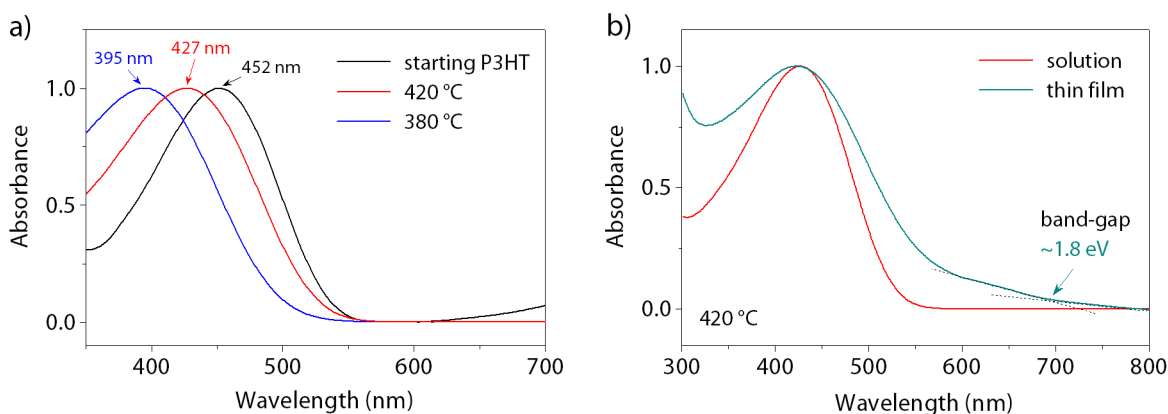


Figure 2. (a) UV-Vis absorption spectra of the polymer chloroform solutions. P3HT evaporated at 380 °C and 420 °C is compared with the starting material. The absorption peaks are normalised to the highest intensity. (b) Solution and thin-film absorption of P3HT evaporated at 420 °C. A band-gap of ~ 1.8 eV is estimated from the thin-film spectrum from the fits indicated on the figure.

The thin-film absorption spectrum of P3HT evaporated at 420 °C is shown in Figure 2b. Comparison of the solution and thin-film spectra does not indicate any red shift of the thin-film absorption in respect to the solution. This suggests poor molecular order in evaporated P3HT films²¹. The onset of polymer absorption is near 700 nm resulting in a solid-state band-gap of ~ 1.8 eV. The estimate is compromised by the background scattering, however, it is consistent with the band-gaps in solution-processed P3HT films reported in literature (1.7-2.1 eV²², the exact value depends on many variables, such as polymer regioregularity or deposition conditions). The weak shoulder near 600 nm can be attributed to interchain interactions in evaporated P3HT. This characteristic absorption feature suggests a presence of intermolecular π - π stacking^{21, 23} and its intensity correlates with the degree of interchain order. The shoulder can be found also in the EQE spectrum of P3HT/C₆₀ planar heterojunction (*section 4.4*, Figure 7d). Despite indications of amorphous nature of P3HT found in AFM (*section 3.4*, Figure 11) and XRD studies (*section 3.5*, Figure 14a), the evaporated P3HT appears to exhibit also a small degree of molecular order.

Infra-Red Spectroscopy (FT-IR) and Nuclear Magnetic Resonance (NMR) were used to investigate the chemical changes in the polymer structure. Figure 3 shows differences in FT-IR spectra between starting and evaporated P3HT. The band assignments and the changes in intensity observed on thermal evaporation are summarised in Table 1.

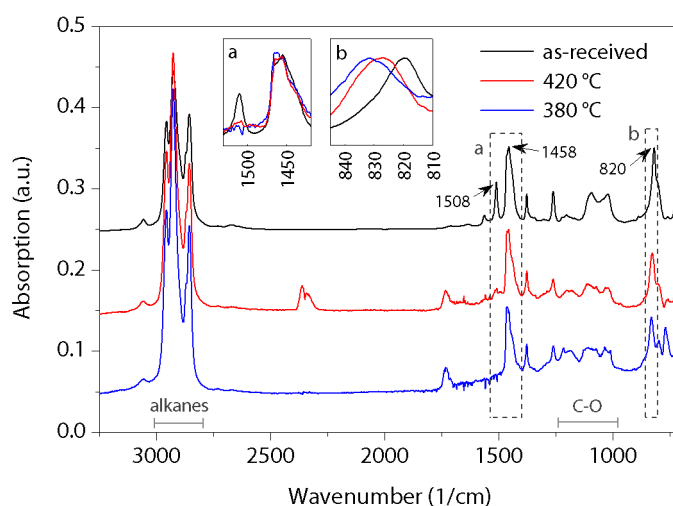


Figure 3. FT-IR spectra of starting P3HT and P3HT after evaporation at 380 °C and 420 °C.

The insets *a* and *b* show magnified details of the spectra.

The spectra of all three polymers look qualitatively similar. The most important changes take place in regions at 820-832 cm^{-1} and 1510-1430 cm^{-1} (*a* and *b* insets of Figure 3). These are directly related to P3HT thiophene ring vibrations and imply changes in conjugation. The bands at 1458 and 1508 cm^{-1} are associated with symmetric and asymmetric ring stretching vibrations, respectively, and their relative ratio indicates the conjugation length of the polymer²⁴. In evaporated samples, the intensity of the absorption peak at 1508 cm^{-1} is significantly reduced which implies a decrease in conjugation length linked to the decrease in molecular weight. This is consistent with a shift of the peak at 820 cm^{-1} . Similarly to what was suggested by the UV-Vis analysis, the conjugation length appears to be higher in P3HT evaporated at 420 °C than the one at

380 °C. The aromatic C-H stretching of the thiophene ring at 3056 cm⁻¹ remains unchanged. The region between 2800-2990 cm⁻¹ is assigned to alkane vibrations, therefore its increase in intensity suggests either a cleavage of side groups or partial decomposition of thiophene ring structures. Basic consideration of the bond-dissociation energies within the system confirms that it is C-C bonds in the alkyl side groups²⁵ (~350 kJmol⁻¹) and inter-ring C-C bonds²⁶ (~390 kJmol⁻¹) which are most susceptible^{27, 28} to excessive thermal energy.

Table 1. Summary of band assignments and intensity changes in the FT-IR spectra of P3HT.

Wavenumber	Vibration	On evaporation
726	Rocking vibrations of the methyl group -CH ₃ ¹⁶	Similar
820-832	Aromatic C-H out-of-plane vibration ¹⁶	Shifted and decreased
1015-1120	Oxidation ²⁹	Increased
1261	In-plane C-H bending of the thiophene ring moieties ³⁰	Similar
1377	Deformation vibrations of the methyl group -CH ₃ ¹⁶	Similar
1458	Symmetric ring stretching vibrations	Normalisation peak
1508	Asymmetric ring stretching vibrations	Decreased
2855	Symmetric C-H stretching vibrations of methylene -CH ₂ - moieties ^{31, 32}	Increased
2926	Asymmetric C-H stretching vibrations of methylene -CH ₂ - moieties ^{31, 32}	Increased
2957	Asymmetric C-H stretching of the methyl group -CH ₃ ¹⁶	Increased
3056	Aromatic C-H stretching vibration	Similar

As the samples were prepared and characterised in air, the unavoidable oxidation might have modified the spectra by giving rise to additional absorption bands, e.g. those at

1015-1120 cm^{-1} ²⁹. Overall, it can be concluded from FT-IR that the polymer undergoes several structural changes during the deposition process, the most pronounced being the decrease in conjugation length.

Structural studies by proton ^1H NMR showed similar results to those obtained from infrared spectroscopy. The polymer retains its conjugated character, however, several differences in the aromatic and alkyl signal regions are detected. Comparing the ^1H NMR spectra of starting and evaporated P3HT in Figure 4, new bands appear at 7.3-8, 1.8-2.7 and 3-6 ppm. The first band implies an increase in the number of protons in the thiophene ring environment and thus a loss of the side chains or conjugation length³³. The latter two bands indicate the presence of various small moieties consisting of single and double carbon bonds which are most likely due to dissociation of some of the ring structures or oxidation products²⁹. Strengthening of the alkyl band at 1.3-1.4 ppm and the methyl band at 0.9 ppm could come from the symmetry of the proton environments within the alkyl chain³⁴. This could be caused by breaking of the side groups away from the backbone.

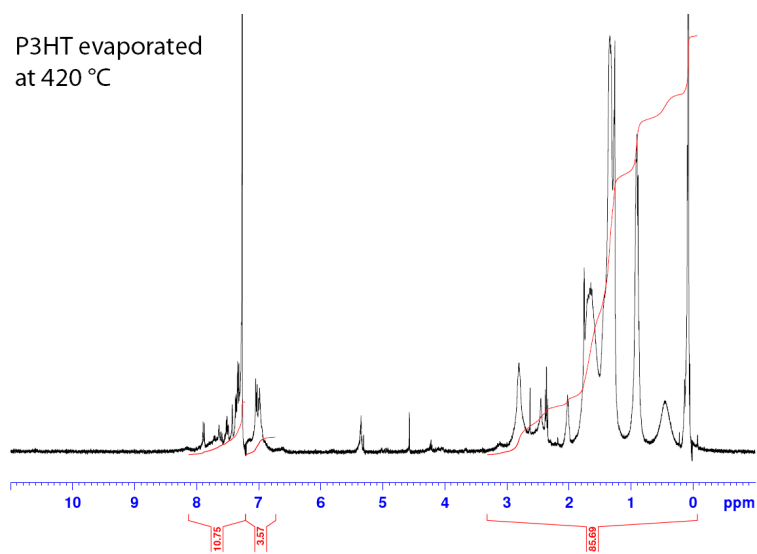
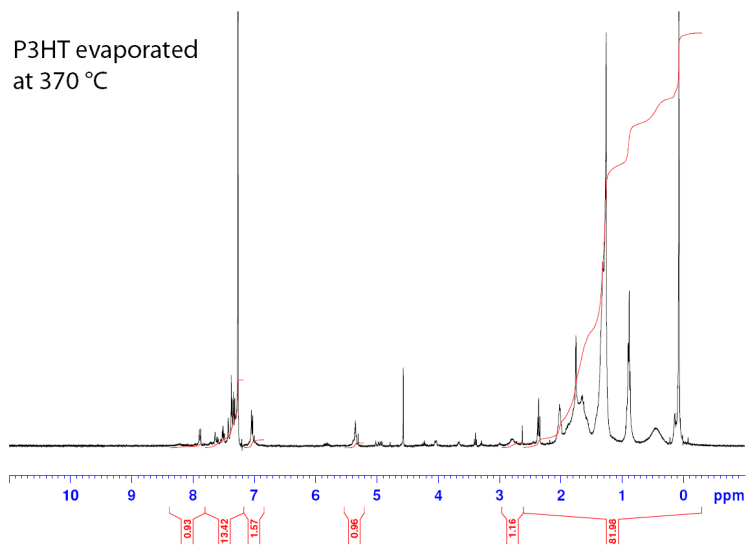
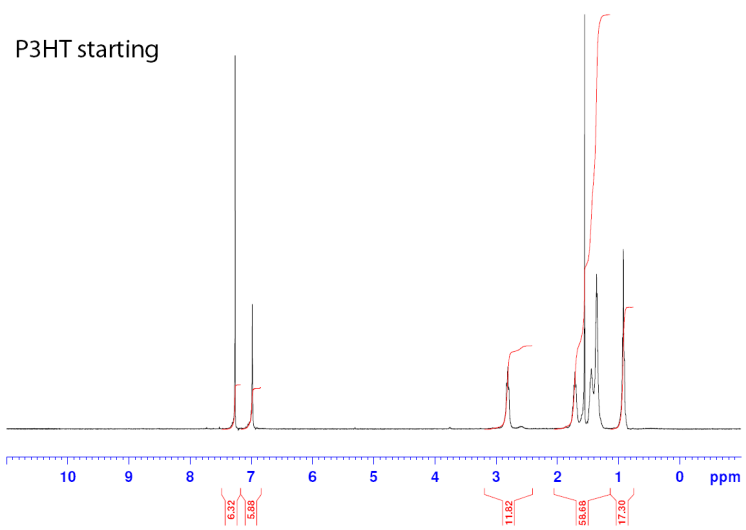


Figure 4. ^1H NMR spectra of starting P3HT and P3HT evaporated at 370 °C and 420 °C.

3.3 Thermal behaviour and vacuum deposition of PTh

The thermal stability of PTh was studied by TGA under an N₂ atmosphere at atmospheric pressure. PTh degradation starts at a much lower temperature than in P3HT. The onset of polymer degradation, as shown in Figure 5a, was identified at approximately 272 °C with weight loss of 5 wt % at 300 °C. This is in good agreement with the findings reported previously by Mo *et al*³⁵.

Thermal behaviour of the polymer was further analysed by DSC and DTA, however, no evident transition peaks were found. Similar thermal behaviour has been observed also by other groups^{36, 37}. The absence of an apparent glass-transition suggests a high level of crystallinity in the starting polymer. DSC and DTA plots are shown in Figure 5b.

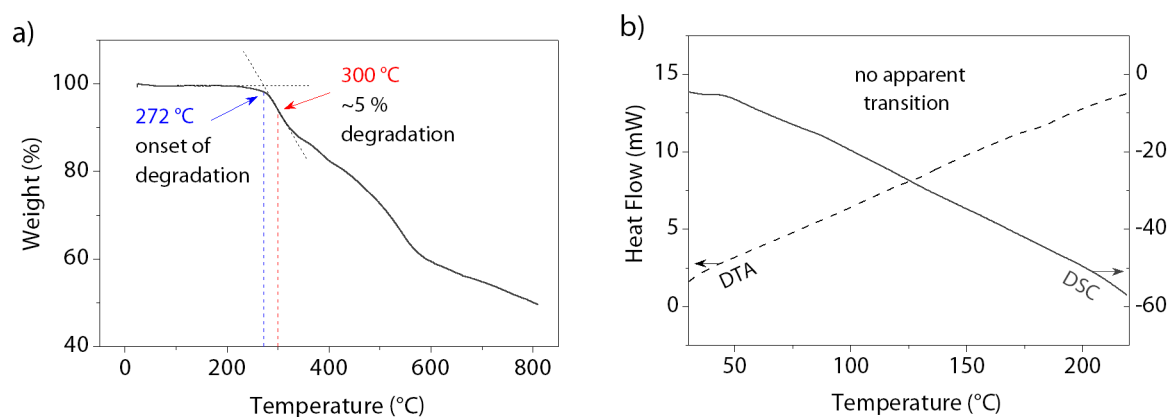


Figure 5. (a) Thermal decomposition of PTh measured by TGA, with the onset of polymer degradation starting at 272 °C. (b) DTA (dotted line) and DSC (solid line) curves of PTh.

Two different temperatures of evaporation, 275 °C and 300 °C, were chosen to determine the influence of heating on the chemical structure of PTh. At 275 °C, the onset of a measurable evaporation rate was detected at this pressure, and 300 °C was the temperature at which only a minor weight loss ($\approx 5\%$) was measured by TGA under nitrogen.

Figure 6a shows UV-vis spectra of chloroform solutions of the evaporated PTh and the starting material. The three curves are normalised to their maximum intensity. The position of the absorption maximum of PTh at 408 nm (corresponding to the intramolecular $\pi-\pi^*$ transition) remains almost unchanged by the evaporation process. Wider but symmetric peaks of the evaporated samples imply that the range of conjugation lengths is increased as a result of evaporation. The starting PTh has a shoulder peak at 614 nm, which likely comes from an intermolecular $\pi-\pi$ stacking and shows a presence of agglomerates^{21, 23}. The peak is shifted towards smaller wavelengths for PTh evaporated at 300 °C and disappears completely for the polymer evaporated at 275 °C. This suggests that the higher temperature process gives rise to greater crystal packing and agglomeration.

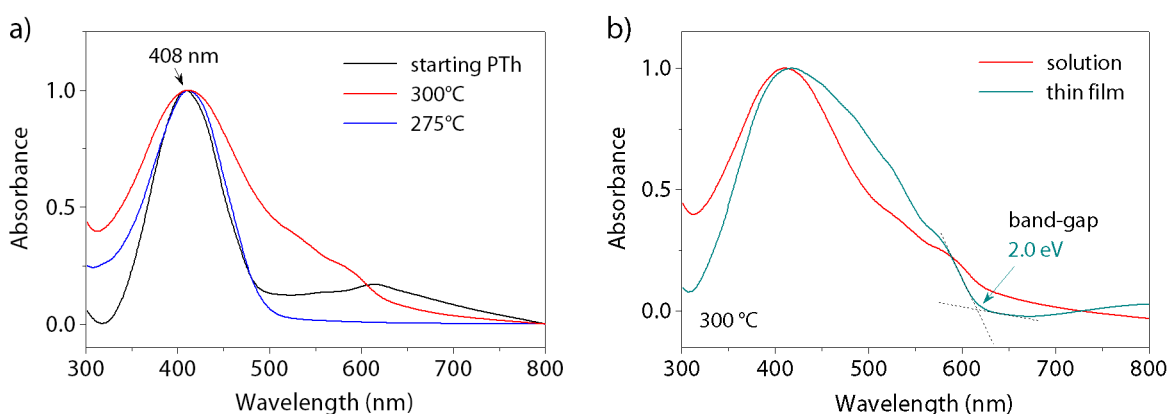


Figure 6. (a) UV-Vis absorption spectra of PTh evaporated at 275 °C and 300 °C in comparison with the starting material. The absorption peaks are normalised to the highest intensity. (b) UV-Vis absorbance spectra of PTh chloroform solution and thin film.

Solid-state absorption of PTh thin film (Figure 6b) displays a slight red shift and a peak broadening compared with the solution. This, as well as apparent spectral shoulders around 550 nm, suggests enhanced crystallinity in vacuum-deposited PTh films²¹. The measured band-gap of the polymer is 2.0 eV, a value approximately same as pristine PTh (2.0 eV acquired experimentally and 2.2-2.3 eV theoretically³⁸).

A comparison of optical properties of the evaporated PTh and P3HT is made in Figure 7 with the main characteristics depicted in Table 2. For PTh (300 °C), the thin film absorption spectrum is considerably more red-shifted with respect to the chloroform solution (7 nm) than it is in the case of P3HT (a blue shift of 2 nm, see Figure 7). Moreover, the band broadening is more significant in the PTh film compared to P3HT. Thus it can be concluded, that PTh molecules have better aggregation and stacking in solid films than those of P3HT. The XRD data (shown later in *section 3.5*, Figure 14a) confirms that the crystallinity of evaporated PTh is greater than in evaporated P3HT films.

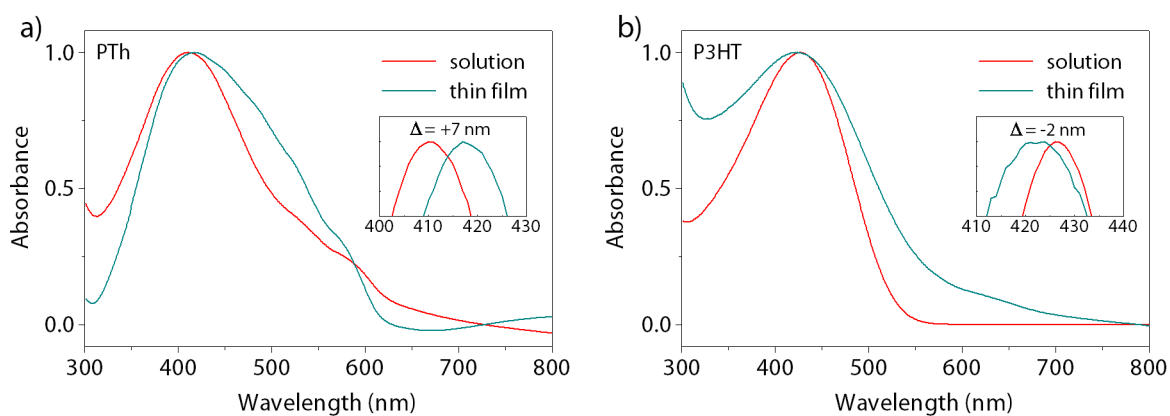


Figure 7. UV-Vis absorbance spectra of (a) PTh and (b) P3HT chloroform solutions and thin films.

Table 2. Comparison of optical parameters of P3HT and PTh.

Polymer	Measured band-gap [eV]	Literature band-gap [eV]	Peak absorption [nm]	Thin film-solution shift [nm]
P3HT	~1.8	1.7-2.1 ²²	427	-2
PTh	2.0	2.0 ³⁸	408	+7

Structural NMR and FT-IR studies of P3HT have shown that the polymer conjugation length decreases during the evaporation and side groups dissociate from the backbone. Due to the absence of side groups in PTh, a decrease in conjugation length is expected to be the only major structural change caused by thermal heating. FT-IR spectroscopy was used to characterise the evaporated PTh and study changes in conjugation, as shown in the Figure 8. As the ratio of symmetric (1439 cm^{-1}) to asymmetric (1489 cm^{-1}) C=C stretching vibrations refers to the conjugation length of polythiophene³⁹, all three spectra were normalised to the intensity of the 1439 cm^{-1} peak in order to directly compare the degree of conjugation. Table 3 summarises changes in positions and intensities of the peaks.

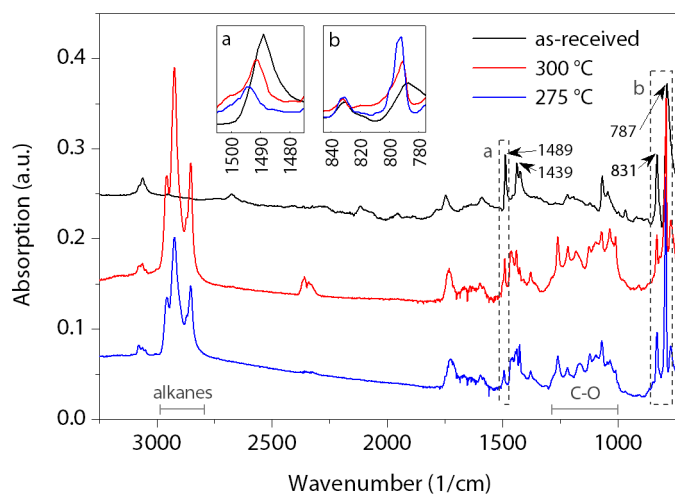


Figure 8. FT-IR spectra of as-received PTh and PTh after evaporation at 275 °C and 300 °C.

The insets *a* and *b* show magnified details of the spectra.

As regards the main PTh vibration ‘fingerprints’, the spectra of starting and evaporated materials are in good agreement for the majority of peaks. The differences at $1000\text{--}1310$ and 1748 cm^{-1} , both associated with oxygen bonds, are caused by oxidation during the sample preparation. We suspect the peaks at 1378 , 1460 and $2800\text{--}2990\text{ cm}^{-1}$, C-H vibrations, come either from the partial decomposition of the thiophene rings and

evaporation of alkane-containing moieties, or some secondary impurity appearing during the sample preparation.

Table 3. Summary of band assignments and intensity changes in the FTIR spectra of PTh.

Wavenumber	Vibration	On evaporation
737	Aromatic C-H out-of-plane vibration	Shifted
787	Thiophene ring vibration ⁴⁰	Shifted and increased
831	Terminal thiophene ring vibration ⁴⁰	Similar
1000-1310	Oxidation	Increased
1378	-CH ₂ and -CH ₃ vibrations	Increased
1439	Symmetric C=C stretching vibration ³⁹	Normalisation peak
1460	-CH ₂ and -CH ₃ vibrations	Increased
1489	Asymmetric C=C stretching vibration ³⁹	Shifted and decreased
1592	Aromatic C-C stretching vibration	Similar
1748	Oxidation	Similar
2800-2990	Alkane vibrations	Increased
3061	Aromatic C-H stretching vibration	Similar

The highlighted region 780-840 cm⁻¹ is related to the thiophene ring vibrations (see inset *a* of Figure 8). The shift and increase of the 787 cm⁻¹ peak indicates a decrease in conjugation length of the polymer⁴⁰. Similar trends can be seen in the range 1480-1500 cm⁻¹ (inset *b* of Figure 8), where the 1489 cm⁻¹ peak (normalised against 1439 cm⁻¹) decreases and consistently shifts to 1491 and 1494 cm⁻¹ for 300 °C and 275 °C, respectively. Both these changes imply loss in the polymer conjugation and hence molecular weight^{39, 41}. As in the case of P3HT, the higher evaporation temperature (300 °C) leads to a higher molecular weight being deposited.

GPC of evaporated and starting PTh was limited by poor solubility in tetrahydrofuran, the mobile phase of the GPC. The starting material could not be dissolved at all while only a small percentage of the evaporated sample could. The evaporated PTh that was dissolved had a $M_w \approx 900-1000 \text{ gmol}^{-1}$ corresponding to a degree of conjugation of about 11-12. The overall average molecular weight of the evaporated material would probably be much higher once the insoluble component is included.

In accordance with UV-Vis findings, GPC shows that the deposited PTh has a higher conjugation length than P3HT. The side groups in P3HT result in unnecessary increased conformational entropy and thus limit the phase transition of the polymer. Comparison of the main molecular weight parameters obtained from GPC is depicted below in Table 4.

Table 4. Comparison of GPC parameters of P3HT and PTh.

Polymer	M_w starting [gmol^{-1}]	M_w evaporated [gmol^{-1}]	Equivalent conjugation
P3HT	~36300	~1500	9
PTh	-	>900-1000	>11-12

3.4 Topography of P3HT and PTh thin films

Performance of photovoltaic devices is largely determined by the quality of individual thin films. Unlike spin-casting methods, vacuum processing of organic molecules generally leads to a high level of homogeneity and only a small number of defects⁴². Evaporated P3HT and PTh thin films were characterised both in terms of surface topography (MicroXAM, AFM) and structural morphology (TEM, XRD).

The surface of P3HT thin films was first investigated by the optical profilometer MicroXAM. As can be seen in Figure 9a, polymer aggregation caused by poor substrate wetting creates large variations in the film thickness. This topography can lead to low shunt resistance of the active layer due to partial shorting across the device and thus limited device performance. Later discussion in *sections 4.3* and *4.5* shows that this effect is indeed apparent, especially in polymer homojunctions and planar heterojunctions with very thin P3HT layers.

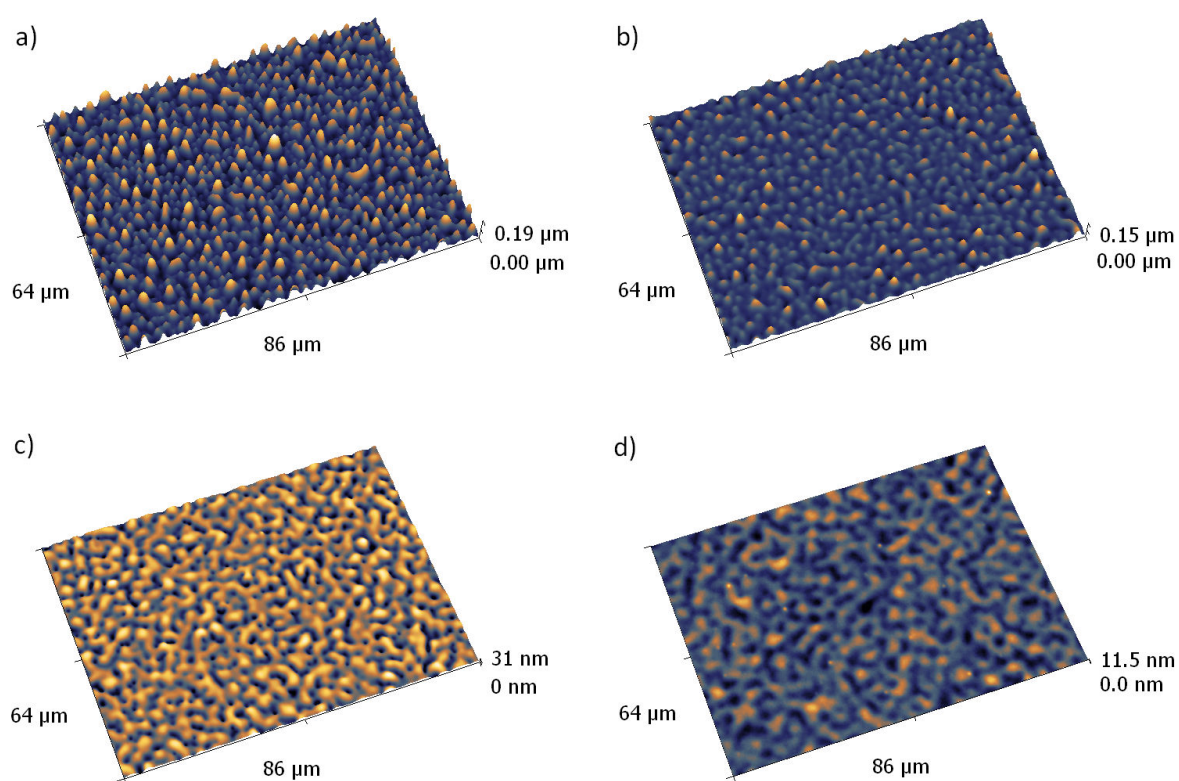


Figure 9. MicroXAM images of P3HT film deposited on different substrates by evaporation: (a) PEDOT annealed at 140 °C/5 min, (b) plain ITO, (c) PEDOT non-annealed, (d) PEDOT annealed and plasma-treated for 2 min. Average P3HT thickness is approximately 70 nm.

Since the evaporated P3HT did not wet the standard PEDOT:PSS electrode surface (after spin-casting PEDOT is annealed at 140 °C for 5 min), different surface modifications were examined for wettability: plain ITO (Figure 9b), non-annealed PEDOT (Figure 9c), and a standard annealed PEDOT treated with oxygen plasma for 2 min (Figure 9d). Respective RMS

roughness values can be found in Table 5. Although de-wetting behaviour was observed in all cases, the smallest variations in thickness were on plasma-treated PEDOT. This is probably due to improved surface energy caused by the plasma treatment.

Table 5. RMS roughness of P3HT deposited at different surfaces.

	PEDOT annealed	ITO	PEDOT non-annealed	PEDOT plasma-treated
RMS roughness (nm)	28.50	13.60	5.60	1.42

P3HT films also suffered from macroscopic defects called ‘spits’. Due to high viscosity of the polymer melt, small micro-droplets were frequently expelled by the evaporation source directly onto the substrate when vapour from beneath the liquid surface was ejected. The number and size of the spits was roughly proportional to the amount of material in the boat and the evaporation temperature. As illustrated in Figure 10, these micro-droplets can take up to almost 1% of the film surface area. This fraction is obviously deposition time/film thickness dependent as the individual data points illustrate (from left to right, the dots represent P3HT films 10, 20, 40 and 70 nm thick).

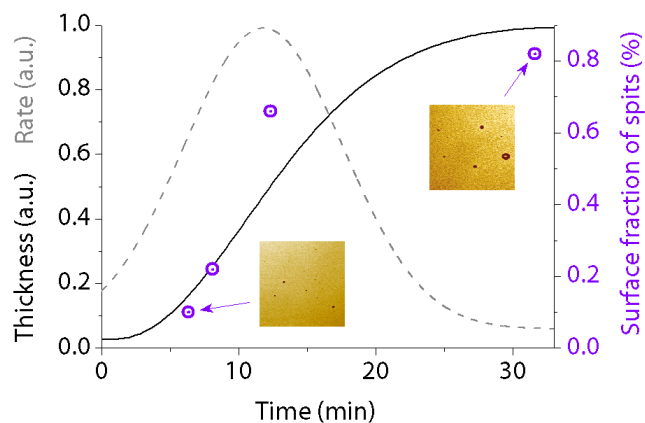


Figure 10. Surface fraction of the spits as a function of deposition time (for devices with 10, 20, 40 and 70 nm thickness). Cumulative thickness (solid line, the peak value is 70 nm) and the deposition rate (dashed line, the peak value is approximately 2 nm/min) are included. Representative optical images are shown for both extreme cases.

The spitting phenomenon was not observed for PTh. This might be directly related to the absence of side groups. Free volume in polythiophene is significantly smaller than that in P3HT, which in turn leads to decreased chain mobility and thus increased T_g . Difference in the molecular weights of the polymers can have additional influence on their plasticity above T_g . Heating of PTh did not lead to liquefaction of the polymer but rather resembled a solid-gas sublimation behaviour. Since the depositions yielded very uniform films, no specific investigation was done to see what the dominant defects in PTh films are. Low shunt resistance in PTh/ C_{60} devices (see *section 4.5*) suggests a presence of pinholes.

Topography and roughness of P3HT and PTh thin films were directly compared at both the macro- and nano-scale. Figure 11 shows a comparison of the surface profiles imaged by MicroXAM (blue images). As already discussed, the P3HT film does not wet the PEDOT:PSS and forms island-type structures. In contrast, PTh coats the surface well and creates a microscopically flat film. Higher resolution topography was obtained from AFM scans, here represented as insets of Figure 11 (brown images). At this scale P3HT films are relatively

smooth, while the PTh is composed of grains between 20 and 50 nm in diameter. The featureless character of the former might result from packing disorder caused by side groups and their dissociation, and the appearance of grains in the latter might be consistent with packing of the PTh molecules into more ordered agglomerates. MicroXAM and AFM images are quantified in terms of RMS roughness which is summarised in Table 6.

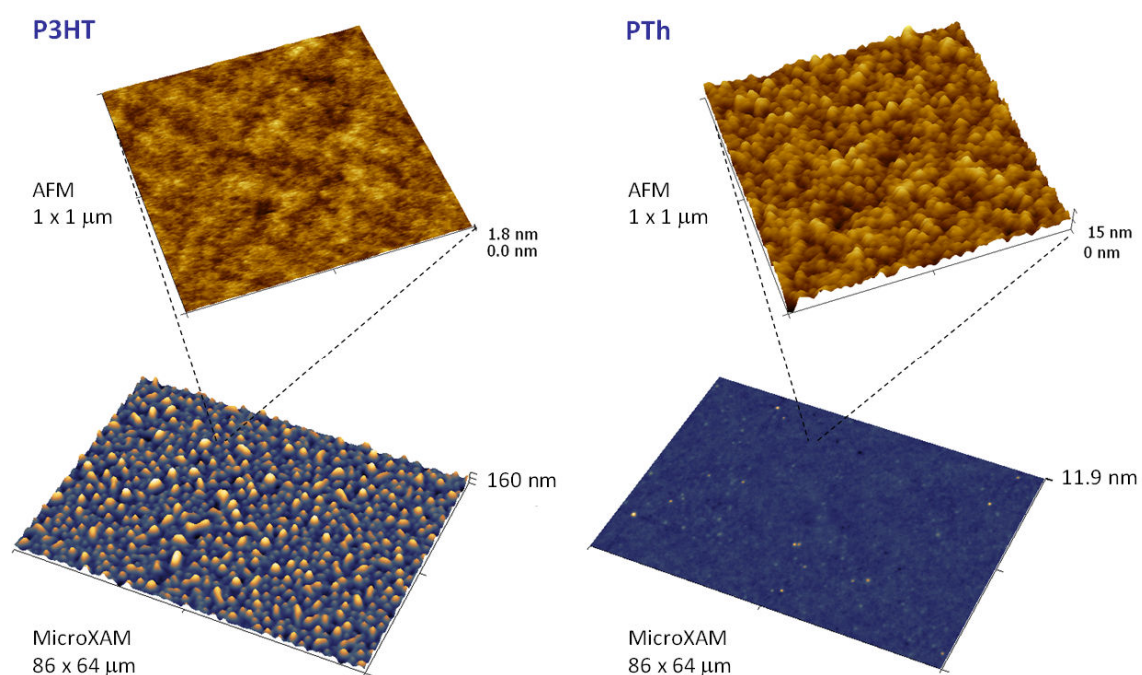


Figure 11. MicroXAM images of 70 nm thick P3HT (left blue) and PTh (right blue) films on PEDOT substrate. Scaled insets (brown) are high resolution 1 x 1 μm AFM scans (positions of the scaled areas are only illustrative).

Table 6. RMS roughness values for MicroXAM and AFM scans of P3HT and PTh thin films.

	P3HT (86 x 64 μm)	PTh (86 x 64 μm)	P3HT (1 x 1 μm)	PTh (1 x 1 μm)
RMS roughness (nm)	26.10	0.35	0.21	1.77

3.5 Structural analysis of P3HT and PTh thin films

Next, structural and morphological studies of P3HT and PTh films were performed using TEM and XRD. The low magnification bright TEM image of PTh shown in Figure 12a suggests a slightly smaller grain size of between 5 and 20 nm. High resolution phase contrast imaging (Figure 12b) of these grains confirms that they are made of single crystals of polythiophene.

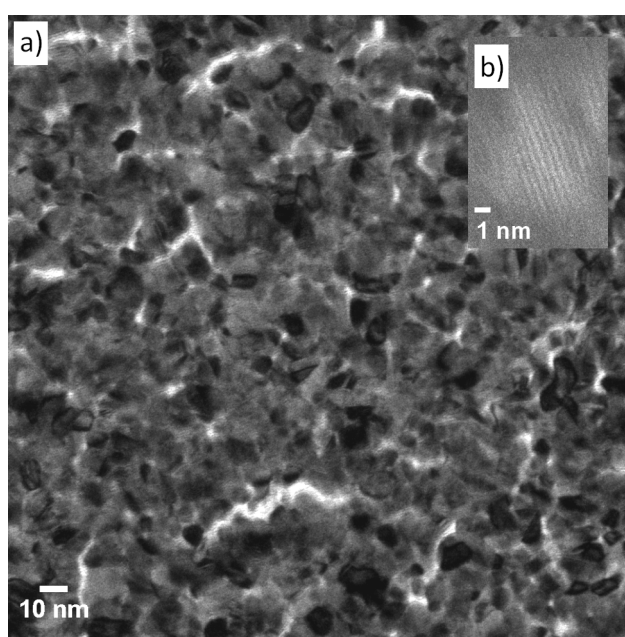


Figure 12. (a) Bright TEM image of PTh grains. (b) Phase contrast image of a single polythiophene crystal.

A TEM diffraction pattern in Figure 13 shows that these crystal grains are orientated in different directions. The plane spacing corresponds with other TEM and XRD studies^{35, 43}. TEM of the P3HT samples shows an amorphous structure with no grains or crystal structure present and an amorphous diffraction pattern.

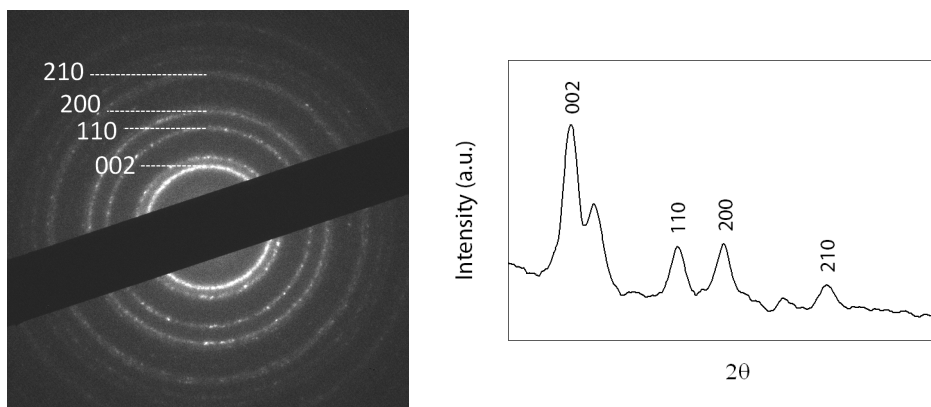


Figure 13. Diffraction pattern of PTh with crystallographic planes indexed (due to lack of supporting literature, no assignment was made to the peak next to 002).

XRD patterns of the PTh film taken normal to its plane suggest substantially higher crystallinity in PTh than its P3HT counterpart (Figure 14a). Such θ - 2θ XRD analysis does not map the full range of crystal orientations, and so the intensities do depend on the orientational distribution of the crystals. Diffraction peaks at 19.6° , 22.8° and 28.0° are in agreement with literature data and correspond to 110, 200 and 210 reflections of polythiophene^{35, 44}. The $(hk0)$ indexing of reflections suggests polythiophene chains lie in the plane of the substrate⁴⁴. The calculated lattice parameters are $a = 7.80 \text{ \AA}$, $b = 5.51 \text{ \AA}$ and $c \approx 7.70 \text{ \AA}$ (c is estimated from the thiophene monomer⁴⁵), all consistent with either a monoclinic or orthorhombic unit cell with the molecules rotated around their axis by alternately $\alpha \approx \pm 31^\circ$ to the unit cell b axis^{35, 45}. This rotation leads to a standard herringbone packing motif as shown in the inset of Figure 14a. Precise parameters as well as determination of monoclinic angle β would require analysis of a more detailed data set.

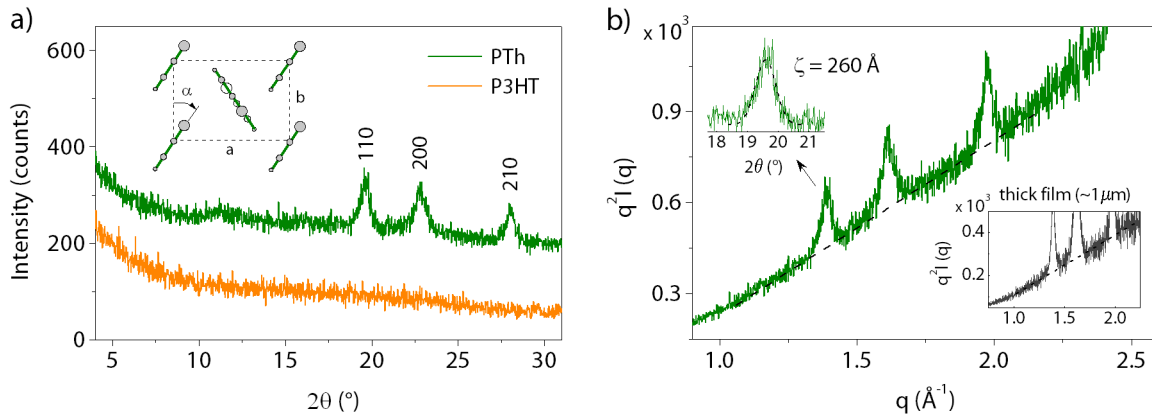


Figure 14. (a) XRD traces of PTh and P3HT deposited on silicon wafers. Inset of the figure shows unit cell of PTh with the herringbone packing motif. (b) XRD intensity curve $q^2I(q)$ of PTh with Gaussian fit of the peak 110 (upper inset) and intensity curve of 1 μm thick PTh film (lower inset).

The degree of crystallinity, X_{cr} , of a polymer can be estimated as the ratio between the intensity of the diffraction peaks over the total diffracted intensity (including amorphous areas). The values of $X_{cr} = 35\text{-}40\%$ have been found for unannealed polythiophene powder^{35, 44}. In order to analyse the contribution of the amorphous background, the data of Figure 14a were replotted as $q^2I(q)$ vs. q (Figure 14b), where $q = 4\pi(\sin\theta)/\lambda$ is the magnitude of the scattering vector and $I(q)$ is the total scattered intensity. This allowed the total intensity to be resolved into the background diffuse scattering and the crystalline diffraction. As seen from the plot, the baseline of the diffraction peaks appears linear (fitted by the dotted line) with no signs of amorphous phase present in this orientation. Similar results were obtained from the analysis of thick-film samples ($\approx 1 \mu\text{m}$, see lower inset of Figure 14b), neither was any amorphous background found outside the plotted range. This implies that the PTh films have high crystallinity^{35, 44} after the vacuum deposition.

Additionally, a coherence length $\xi = 260 \text{ \AA}$ of the polymer was calculated from the Debye-Scherrer relation⁴⁶

$$\xi = 57.3\lambda/(\beta \cos\theta) \quad (1)$$

where $\beta = (B^2 - b_0^2)^{1/2}$, B is the measured half-width of the peak (in degrees), b_0 is the instrumental resolution ($<0.05^\circ$), λ is the wavelength of the X-radiation (1.5418 Å), 2θ is the scattering angle. Half-width B was obtained from a Gaussian fit of the peak 110, as seen in upper inset of Figure 14b. The equivalent crystal size ~ 25 nm would be consistent with the findings of both AFM and TEM.

3.6 Conclusion

The vacuum thermal evaporation of P3HT and PTh has been investigated. Structural studies of P3HT before and after evaporation revealed changes in the molecular structure caused by thermal heating. According to GPC, FT-IR and NMR, the most pronounced differences are the loss of molecular weight and cleavage of the alkyl side groups from the conjugated backbone. Similarly, the conjugation length of side group-free PTh was found to decrease after evaporation. The estimated degree of conjugation in deposited PTh was higher than in P3HT and so was the correspondence of the PTh optical band-gap with the previous literature.

The study has shown that polymer side groups have a strong influence on the morphological properties of vacuum-deposited polymer thin films. MicroXAM and AFM topographic characterisation showed that while PTh forms uniform flat thin films, P3HT dewets the surface and forms island-type structures. Moreover, TEM and XRD data revealed that, unlike P3HT, evaporated PTh forms highly crystalline films without requiring

annealing. This implies significantly higher molecular order in PTh than in its solution-processable equivalent P3HT. The vacuum thermal evaporation was thus shown to be suitable for the deposition of low solubility polymers.

3.7 References

1. Krebs, F. C. *Solar Energy Materials and Solar Cells* **2009**, 93, (4), 394-412.
2. Xue, J. G.; Uchida, S.; Rand, B. P.; Forrest, S. R. *Applied Physics Letters* **2004**, 84, (16), 3013-3015.
3. Rand, B. P.; Genoe, J.; Heremans, P.; Poortmans, J. *Progress in Photovoltaics* **2007**, 15, (8), 659-676.
4. Li, G.; Zhu, R.; Yang, Y. *Nature Photonics* **2012**, 6, (3), 153-161.
5. Dennler, G.; Scharber, M. C.; Brabec, C. J. *Advanced Materials* **2009**, 21, (13), 1323-1338.
6. Ma, W. L.; Yang, C. Y.; Gong, X.; Lee, K.; Heeger, A. J. *Advanced Functional Materials* **2005**, 15, (10), 1617-1622.
7. Kim, J. Y.; Lee, K.; Coates, N. E.; Moses, D.; Nguyen, T. Q.; Dante, M.; Heeger, A. J. *Science* **2007**, 317, (5835), 222-225.
8. Gritsenko, K. P.; Krasovsky, A. M. *Chemical Reviews* **2003**, 103, (9), 3607-3649.
9. Angelopoulos, M.; Asturias, G. E.; Ermer, S. P.; Ray, A.; Scherr, E. M.; Macdiarmid, A. G.; Akhtar, M.; Kiss, Z.; Epstein, A. J. *Molecular Crystals and Liquid Crystals* **1988**, 160, 151-163.
10. Biswas, A.; Marton, Z.; Kanzow, J.; Kruse, J.; Zaporajtchenko, V.; Faupel, F.; Strunskus, T. *Nano Letters* **2003**, 3, (1), 69-73.
11. Biswas, A.; Aktas, O. C.; Kanzow, J.; Saeed, U.; Strunskus, T.; Zaporajtchenko, V.; Faupel, F. *Materials Letters* **2004**, 58, (9), 1530-1534.
12. Faupel, F.; Takele, H.; Greve, H.; Pochstein, C.; Zaporajtchenko, V. *Nanotechnology* **2006**, 17, (14), 3499-3505.
13. Faupel, F.; Beyene, H. T.; Chakravadhanula, V. S. K.; Hanisch, C.; Elbahri, M.; Strunskus, T.; Zaporajtchenko, V.; Kienle, L. *Journal of Materials Science* **2010**, 45, (21), 5865-5871.
14. Vree, C.; Mayr, S. G. *Journal of Applied Physics* **2008**, 104, (8), -.
15. Irimia-Vladu, M.; Marjanovic, N.; Vlad, A.; Ramil, A. M.; Hernandez-Sosa, G.; Schwodiauer, R.; Bauer, S.; Sariciftci, N. S. *Advanced Materials* **2008**, 20, (20), 3887-+.
16. Wei, H. Y.; Scudiero, L.; Eilers, H. *Applied Surface Science* **2009**, 255, (20), 8593-8597.

17. Yang, H. C.; Shin, T. J.; Yang, L.; Cho, K.; Ryu, C. Y.; Bao, Z. N. *Advanced Functional Materials* **2005**, 15, (4), 671-676.
18. Patricio, P. S. O.; Calado, H. D. R.; de Oliveira, F. A. C.; Righi, A.; Neves, B. R. A.; Silva, G. G.; Cury, L. A. *Journal of Physics-Condensed Matter* **2006**, 18, (32), 7529-7542.
19. Zen, A.; Pflaum, J.; Hirschmann, S.; Zhuang, W.; Jaiser, F.; Asawapirom, U.; Rabe, J. P.; Scherf, U.; Neher, D. *Advanced Functional Materials* **2004**, 14, (8), 757-764.
20. Kline, R. J.; McGehee, M. D.; Kadnikova, E. N.; Liu, J. S.; Frechet, J. M. J.; Toney, M. F. *Macromolecules* **2005**, 38, (8), 3312-3319.
21. Brown, P. J.; Thomas, D. S.; Kohler, A.; Wilson, J. S.; Kim, J. S.; Ramsdale, C. M.; Siringhaus, H.; Friend, R. H. *Physical Review B* **2003**, 67, (6).
22. Fichou, D., *Handbook of Oligo- and Polythiophenes*. John Wiley & Sons: 2008; p 558.
23. Sun, S. Y.; Salim, T.; Wong, L. H.; Foo, Y. L.; Boey, F.; Lam, Y. M. *Journal of Materials Chemistry* **2011**, 21, (2), 377-386.
24. Chen, T. A.; Wu, X. M.; Rieke, R. D. *Journal of the American Chemical Society* **1995**, 117, (1), 233-244.
25. Johnstone, R. A. W.; Rose, M. E., *Mass Spectrometry for Chemists and Biochemists*. Cambridge University Press: 1996; p 524.
26. da Silva, M. A. V. R.; Santos, A. F. L. O. M.; Gomes, J. R. B.; Roux, M. V.; Temprado, M.; Jimenez, P.; Notario, R. *Journal of Physical Chemistry A* **2009**, 113, (41), 11042-11050.
27. Depuy, C. H.; Kass, S. R.; Bean, G. P. *Journal of Organic Chemistry* **1988**, 53, (19), 4427-4433.
28. Culberson, L. M.; Sanov, A. *Journal of Chemical Physics* **2011**, 134, (20).
29. Pretsch, E.; Bühlmann, P.; Badertscher, M., *Structure Determination of Organic Compounds: Tables of Spectral Data*. Springer: 2009; p 422.
30. Rico, M.; Orza, J. M.; Morcillo, J. *Spectrochimica Acta* **1965**, 21, (4), 689-&.
31. Li, J. Q.; Aoki, K. *Journal of Electroanalytical Chemistry* **1998**, 458, (1-2), 155-160.
32. Singh, R. K.; Kumar, J.; Singh, R.; Kant, R.; Chand, S.; Kumar, V. *Materials Chemistry and Physics* **2007**, 104, (2-3), 390-396.
33. Olinga, T.; Destri, S.; Porzio, W.; Selva, A. *Macromolecular Chemistry and Physics* **1997**, 198, (4), 1091-1107.
34. Ferrari, M.; Mucci, A.; Schenetti, L.; Malmusi, L. *Magnetic Resonance in Chemistry* **1995**, 33, (8), 657-663.
35. Mo, Z.; Lee, K. B.; Moon, Y. B.; Kobayashi, M.; Heeger, A. J.; Wudl, F. *Macromolecules* **1985**, 18, (10), 1972-1977.
36. Chen, S. A.; Ni, J. M. *Macromolecules* **1992**, 25, (23), 6081-6089.

37. Sankir, M.; Kucukyavuz, Z.; Kucukyavuz, S. *Journal of Applied Polymer Science* **2003**, 87, (13), 2113-2119.
38. Salzner, U.; Lagowski, J. B.; Pickup, P. G.; Poirier, R. A. *Synthetic Metals* **1998**, 96, (3), 177-189.
39. Furukawa, Y.; Akimoto, M.; Harada, I. *Synthetic Metals* **1987**, 18, (1-3), 151-156.
40. Akimoto, M.; Furukawa, Y.; Takeuchi, H.; Harada, I.; Soma, Y.; Soma, M. *Synthetic Metals* **1986**, 15, (4), 353-360.
41. Poussigue, G.; Benoit, C. *Journal of Physics-Condensed Matter* **1989**, 1, (48), 9547-9560.
42. Forrest, S. R. *Nature* **2004**, 428, (6986), 911-918.
43. Garnier, F.; Tourillon, G.; Barraud, J. Y.; Dexpert, H. *Journal of Materials Science* **1985**, 20, (8), 2687-2694.
44. Hermet, P.; Bantignies, J. L.; Almairac, R.; Sauvajol, J. L.; Serein, F.; Lere-Porte, J. P. *Journal of Physical Chemistry B* **2008**, 112, (40), 12662-12665.
45. Bruckner, S.; Porzio, W. *Makromolekulare Chemie-Macromolecular Chemistry and Physics* **1988**, 189, (4), 961-967.
46. Alexander, L. E., *X-Ray Diffraction Methods in Polymer Science*. John Wiley & Sons Inc: 1969; p 582.

4.1 Introduction

Polythiophenes form a family of conjugated polymers that has been investigated for more than three decades¹⁻³. Their distinctive electronic properties have stimulated their application in many fields of electronics and optics, such as chemical and biological sensors, field-effect transistors, photovoltaic cells and light-emitting diodes⁴⁻¹¹. Efficient charge transport in conjugated systems occurs via strong coupling of the polymer electronic states. Polymer structure determines both backbone planarity and π stacking which influences intra and inter-chain electronic processes¹²⁻¹⁴. Polymers with no side groups have the opportunity for enhanced backbone packing and electronic properties in the solid state^{15, 16}, but for their effective processing in solution, side groups have to be added. In this chapter, functional photovoltaic devices based on vacuum-deposited polythiophenes, PTh and P3HT, are presented. Different processing and device parameters are examined, and the influence side groups have on the electronic properties of the cells is explored. Planar heterojunction devices with high rate of reproducibility and efficiencies comparable to solution-deposited equivalents are fabricated.

Since the discovery of electrical conductivity in polythiophene, many attempts have been made to improve its solubility while preserving its unique properties. Introduction of alkyl groups onto the polythiophene backbone has led to a successful trade-off between

solubility and conductivity¹⁷. Presence of these groups, however, results in distortions of the backbone conformation and thus various side effects, such as temperature- or solvent-induced changes in the optical absorption (i.e. thermochromism or solvatochromism¹⁸). Layered structures have alkyl side groups acting as spacers between the backbone stacks thus allowing delocalisation of molecular orbitals in only two dimensions of the polymer crystal (separation within the backbone plane is shown in Figure 1). In addition, the high degree of regioregularity of polythiophenes is required to prevent molecular disorder¹⁹. It has been shown that intermolecular packing is reduced by increased side-chain disorder with longer alkyl side groups in polythiophenes²⁰ and several studies of hole transport in thin films of poly(3-alkylthiophene)s have revealed a decrease in mobility as a function of increasing side-chain length²¹⁻²⁴. These are just some of the examples, in which optical and electronic properties of the polymers are compromised by their need for solubility²¹.

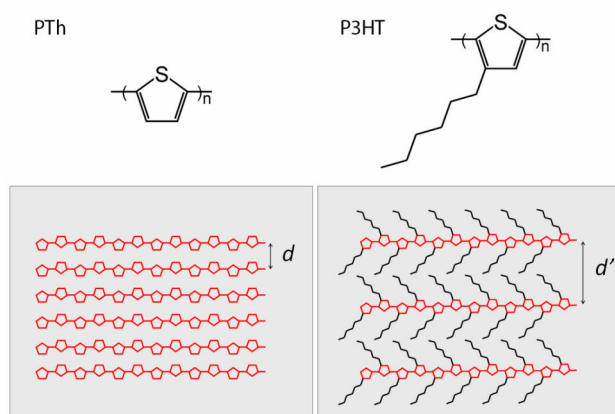


Figure 1. Molecular structure of P3HT and PTh with simple models of their packing. PTh chains pack with closer proximity (d) than P3HT (d') due to the lack of side groups.

Various deposition methods have been explored to enhance the molecular order and packing in polythiophene thin films. These included Langmuir-Blodgett films^{25, 26}, electrochemical polymerisation on conductive surfaces²⁷⁻²⁹, or transformation of soluble

precursor polymers³⁰⁻³². Many of these techniques, however, lack scalability and the throughput necessary for industrial application, while others involve reactions (e.g. heating, UV-light) which cause degradation of other device components or leave by-product residues. Standard solution coating and printing are thus the only widely investigated methods for large-scale processing of conjugated polymers^{33, 34}.

Sections 3.2 and 3.3 have shown that polythiophenes can be deposited by vacuum thermal evaporation while mostly retaining their chemical composition and structure. In this chapter, the deposition technique is applied to fabricate simple Schottky junction polythiophene/Al and planar heterojunction polythiophene/C₆₀ photovoltaic cells. It is shown that assembly of PTh molecules into ordered films with high crystallinity leads to enhanced charge transport properties. To illustrate the potential of vacuum-deposited polymer thin films in electronic and optoelectronic applications, a series of photovoltaic devices is fabricated and their detailed characterisation performed.

4.2 Electronic properties of PTh and P3HT thin films

A high degree of molecular order of polymers is known to improve the charge carrier transport³⁵. The space charge limited current (SCLC) technique³⁶ was therefore used to measure hole mobility, μ_p , of PTh and P3HT. Hole-only devices were fabricated by depositing a polymer layer between PEDOT-coated ITO bottom electrode and an 80 nm thick gold top electrode, as drawn in Figure 2 (in the case of P3HT, the wettability of the standard annealed PEDOT surface was altered by plasma treatment in order to prevent device shorting, see *section 3.4*). The work function of Au matches the HOMO level of the polymer and creates an

ohmic contact for efficient hole injection. In contrast to FET mobility measurements, this architecture allows accurate determination of mobilities normal to the plane of the device, the direction of charge transport in photovoltaic devices.

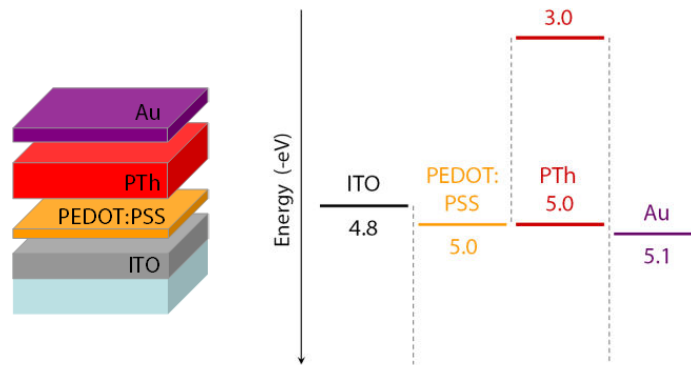


Figure 2. Schematic drawing of the device architecture used for SCLC measurements (left) with position of the energy levels (right). Exact position of the PTh³⁷ levels after the vacuum deposition is unknown. The uncertainty in the PEDOT:PSS levels is approximately ± 0.2 eV³⁸ (this might be further increased by the plasma treatment).

Figure 3 shows the current density as a function of the applied voltage (corrected for the built-in voltage $V_{BI\ PTh} \approx 0.05$ V, $V_{BI\ P3HT} \approx 0.02$ V) in both log-log (Figure 3a) and semi-log scales (Figure 3b). While the slope of the curve at low voltages equals 1 and reflects the linear ohmic behaviour of the device, the slope at higher voltages is 2 indicating the presence of space charge-limited current.

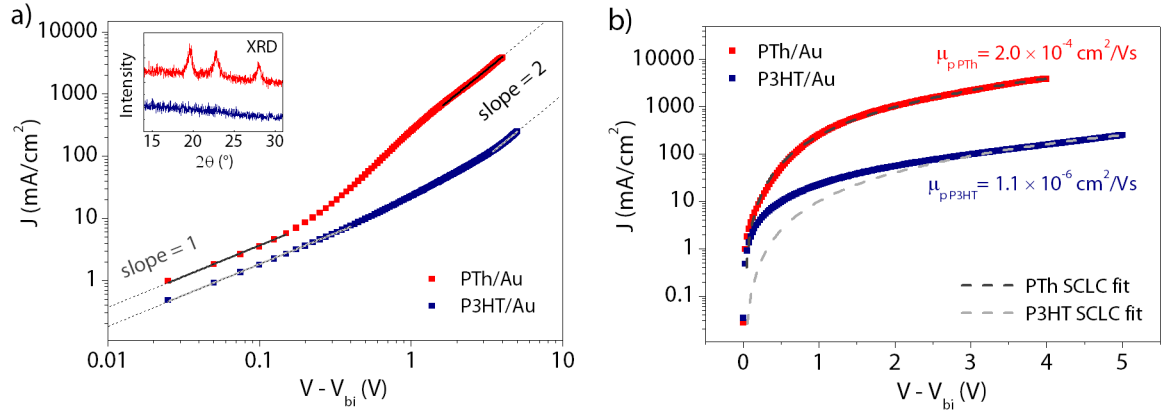


Figure 3. (a) Dark J - V characteristics of an ITO/PEDOT:PSS/polymer/Au devices in double-logarithmic scale. Fitted are low-voltage regions with ohmic character (slope = 1) and space charge limited regions above >1 V (slope = 2). The inset compares crystallinity of PTh (red) and P3HT (blue) thin films as previously measured by XRD (*section 3.5*). (b) The same J - V characteristics in semi-logarithmic scale fitted by single-carrier SCLC (Equation 1).

In the space charge-limited regime, the electrode injects more holes than the material can transport and the J - V dependence become quadratic as quantitatively described by Child's law³⁶

$$J = \frac{9}{8} \varepsilon_0 \varepsilon_r \mu_p \frac{V^2}{L^3} \quad (1)$$

where ε_0 is permittivity of free space, ε_r is the dielectric constant (~ 3 for both PTh³⁹ and P3HT⁴⁰), μ_p is the mobility, V is potential and L is the film thickness (in our case 130 nm for PTh and ~ 65 nm for P3HT). Fitting Equation 1 to the experimental data leads to the hole mobilities $\mu_{p\text{PTh}} = 2.0 \times 10^{-4} \text{ cm}^2\text{V}^{-1}\text{s}^{-1}$ and $\mu_{p\text{P3HT}} = 1.1 \times 10^{-6} \text{ cm}^2\text{V}^{-1}\text{s}^{-1}$, as shown in Figure 3b.

Although the value for P3HT appears very low, it likely reflects the poor molecular order in the polymer films as revealed by XRD and TEM studies in *section 3.5* (see also the inset of Figure 3a). Hole mobility in PTh is comparable with the best photodiode mobilities achieved for ordered high molecular weight P3HT deposited from solution^{36, 41}.

4.3 Polymer/Al Schottky photovoltaic devices

When polythiophene (PTh or P3HT) is placed in a direct contact with aluminium, a Schottky junction forms at the semiconductor/metal interface⁴². Simple photovoltaic devices were thus fabricated by depositing an Al top electrode onto the polymer layer, as shown in Figure 4 (as with SCLC devices, the wettability of the standard annealed PEDOT surface was altered by plasma treatment in order to minimise device shorting). The thickness of the PTh layer was 60 nm, and P3HT layer ~50 nm. The *J-V* characteristics of both PTh/Al and P3HT/Al homojunctions in the dark and under illumination are plotted in Figure 4a and Figure 4b, respectively.

To a certain extent, both polymers exhibited a photovoltaic effect. However, it was only PTh/Al junction which generated significant photocurrent and photovoltage, and displayed rectifying diode behaviour. De-wetting of P3HT likely resulted in an extremely low shunt resistance and degraded photo-response. Overall, the performance of the Schottky devices was very poor. A low exciton diffusion length in the polymers probably causes substantial monomolecular recombination, and reduced shunt resistance of the films (especially de-wetting P3HT).

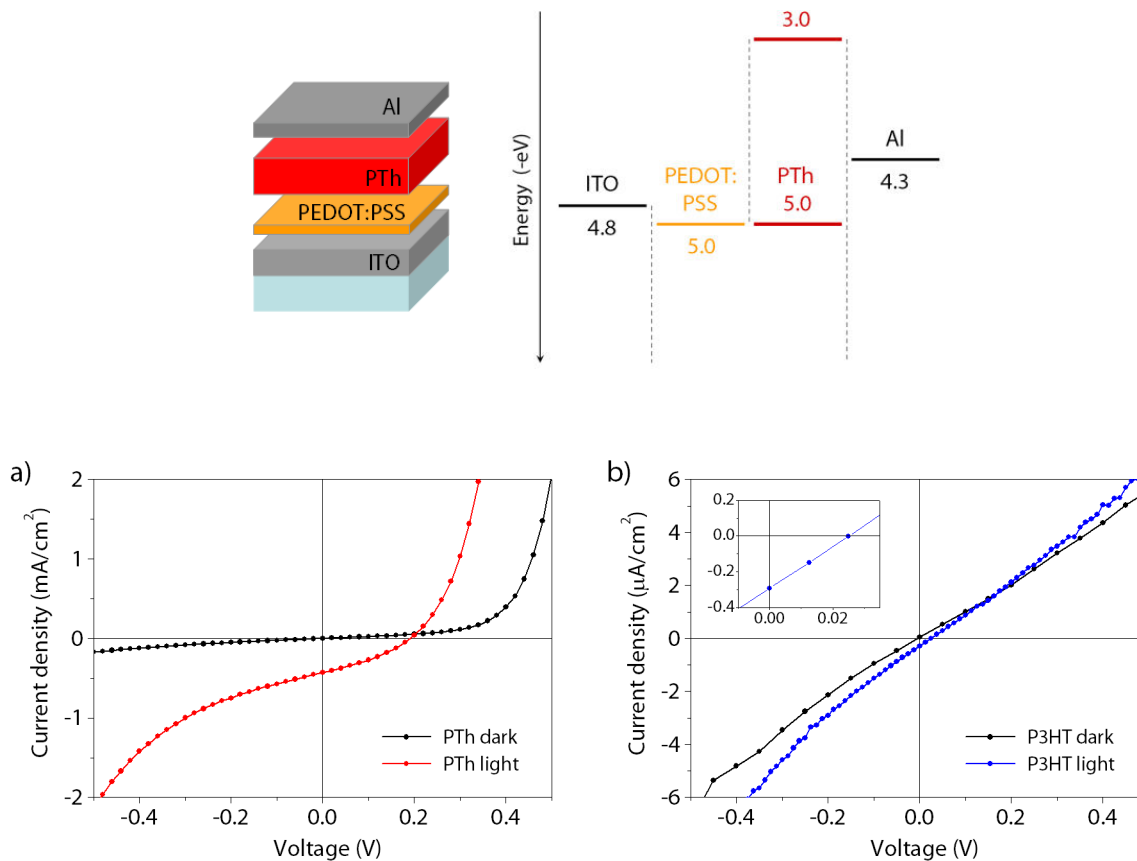


Figure 4. Architecture of the PTh/Al Schottky junction (top left) with position of the energy levels (top right). Light and dark J - V characteristics of (a) PTh/Al and (b) P3HT/Al homojunctions (inset of (b) shows the 4th quadrant in detail). Absence of a standard diode rectification for the P3HT homojunction could be attributed to low R_{sh} .

As Schottky junctions based on organic semiconductors generally exhibit poor performance^{43, 44}, no further optimisation or analysis was performed on the devices.

4.4 Polymer/fullerene planar heterojunction solar cells

To demonstrate the possibilities for vacuum thermal deposition of conjugated polymers, polymer/fullerene planar heterojunction devices were fabricated. Figure 5 shows a schematic drawing of the device architecture with positions of the energy levels.

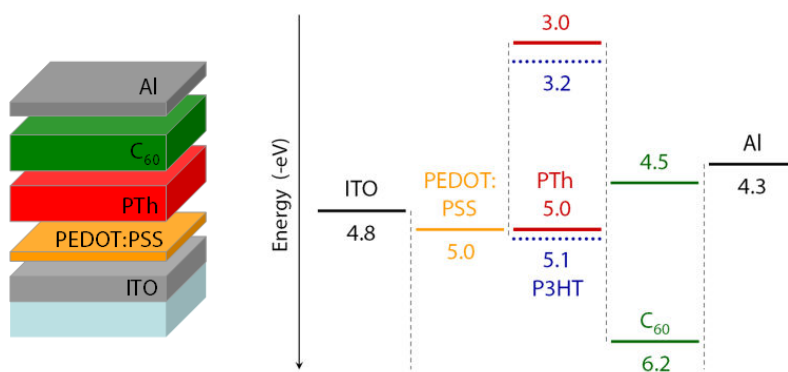


Figure 5. Architecture of the polymer-based planar heterojunction solar cell (left) with position of the energy levels^{38, 45, 46} (right). Due to structural changes taking place during the evaporation, the polymer energy levels are only approximate.

The maximum open circuit voltage of an organic photovoltaic cells is strongly influenced by the energy difference between HOMO level of the donor and LUMO level of the acceptor⁴⁵. However, its 'real' experimental value is determined by a large number of factors ranging from the device architecture and morphology of the thin films⁴⁷⁻⁴⁹ to molecular properties of the donor/acceptor interface⁵⁰ and dependence of the energy levels on temperature and molecular order^{51, 52}.

In the previous chapter it was shown that vacuum thermal evaporation significantly affects the molecular weight of the polymer and hence its electronic structure. This means that processing conditions impact the overall device V_{oc} . Figure 6 suggests this dependence, i.e. V_{oc} of P3HT/ C_{60} heterojunctions is plotted as a function of the evaporation temperature (note that all depositions were conducted at the same vacuum pressure, and the thickness of the samples was >15 nm in order to minimise the effect of low shunt resistance due to de-wetting, as seen in *section 4.5*). An average V_{oc} of 0.35 V for P3HT evaporated at 385 °C increases to 0.7 V for polymer evaporated at 415 °C. In line with *section 3.2*, where higher evaporation temperature was shown to better preserve the polymer molecular weight,

this improvement in V_{oc} indicates that the evaporation of P3HT at higher temperatures might be an important step towards preserving its optoelectronic properties. The other important parameters influencing V_{oc} are the thin-film growth conditions. Shunt resistance (and thus V_{oc}) can be affected through different deposition rates which cause differences in growth and molecular stacking of P3HT. These morphological effects were not investigated. The value of V_{oc} drops again to 0.6 V once the temperature is raised further to 435 °C, however, this can already be an effect of the excessive heat which leads to the polymer degradation. In the case of PTh/ C_{60} devices, no clear dependence of V_{oc} on the evaporation temperature of the polymer was found. The values were similar ~ 0.4 V across a wide range of temperatures (290-350 °C).

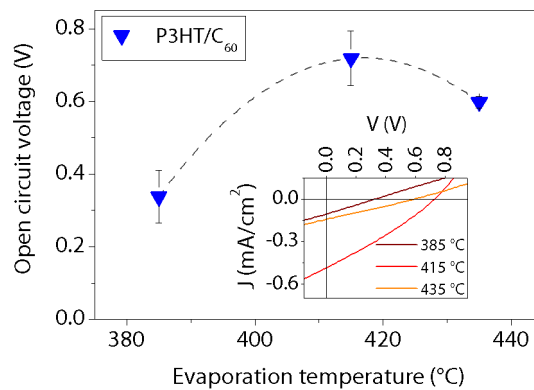


Figure 6. V_{oc} of the P3HT/ C_{60} heterojunctions as a function of evaporation temperature.

The inset shows J - V curves of the representative devices (thickness of P3HT was 38 nm/385 °C, 19 nm/415 °C and 24 nm/435 °C, with $C_{60} \geq 50$ nm).

Finally, a comparison of two representative P3HT and PTh-based heterojunctions is shown in Figure 7. The thickness of the P3HT layer is 12 nm, PTh 40 nm (both near their optimal value, see *section 4.5*) and C_{60} layer 50 nm (also, see *section 4.5*). V_{oc} of the PTh/ C_{60} device appears much smaller (by ~ 0.25 V) than would be expected from the HOMO level difference between PTh and P3HT (~ 0.1 eV). This suggests that there are additional factors

which determine its value. Firstly, the shunt resistance (R_{sh}) of the PTh/ C_{60} heterojunction is substantially lower than in P3HT/ C_{60} (see Table 1), probably due to crystalline nature of as-deposited PTh (see section 3.5). Low R_{sh} results from partial shorting across the device and leads to decreased V_{oc} . Secondly, the reverse saturation current density (J_0) which corresponds to the strength of intermolecular interaction between PTh/ C_{60} is higher than in P3HT/ C_{60} (Table 1). Perez *et al.* has shown that high J_0 in planar heterojunction interfaces indicates strong donor/acceptor intermolecular overlap and also reduced V_{oc} . This overlap was also correlated with higher crystallinity of the donor molecules as well as better hole transport properties⁵⁰.

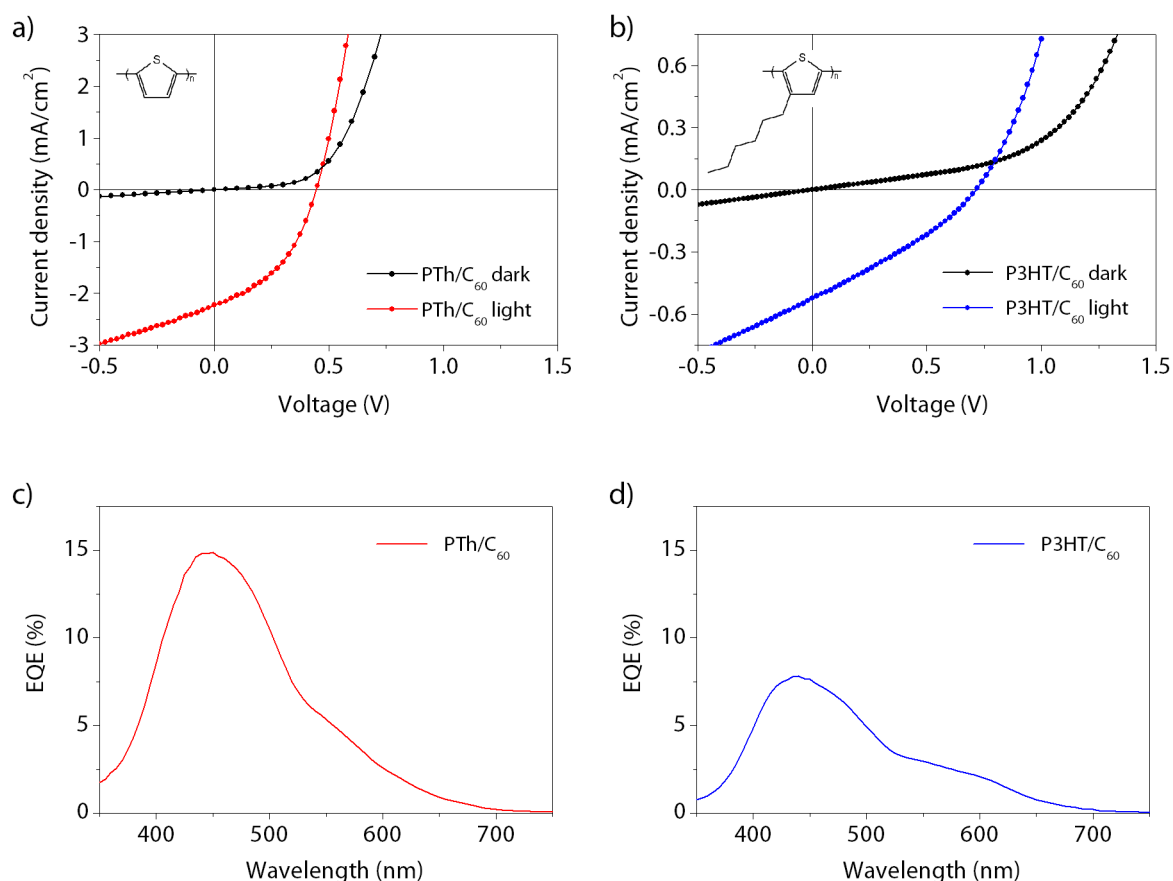


Figure 7. Light and dark J - V characteristics of a typical PTh- (a) and P3HT-based (b) planar heterojunction. EQE response of the PTh/ C_{60} (c) device and P3HT/ C_{60} (d) device with the same thickness as (b). As discussed in section 3.2, the shoulder features near 600 nm (c, d) suggest intermolecular π - π interactions and thus crystallinity of the evaporated polymers.

Enhanced molecular packing and hole transport in PTh leads to lower charge recombination (improved FF) and more efficient charge extraction (J_{sc}). This is also demonstrated by higher external quantum efficiency (EQE), as shown in Figure 7c, d. Accordingly, the series resistance of the PTh/ C_{60} device is considerably lower than P3HT/ C_{60} despite the increased device thickness (Table 1).

Table 1. Qualitative comparison of typical P3HT (12 nm) and PTh (40 nm) bilayers.

device	R_{sh} [Ωcm^2]	J_0 [mAcm^{-2}]	V_{oc} [V]	FF [%]	R_s [Ωcm^2]	Peak EQE [%]
PTh/ C_{60}	622	1.21×10^{-2}	0.45	42.2	11	14.9
P3HT/ C_{60}	1377	1.66×10^{-5}	0.71	30.6	349	7.8

4.5 Thickness-optimisation of planar heterojunction solar cells

The optoelectronic behaviour of PTh and P3HT films was studied in thickness-optimised planar heterojunction solar cells of configuration ITO/PEDOT:PSS/polymer/ C_{60} /Al. This allowed direct comparison of the effect of the materials properties without the greater variability in morphology associated with bulk heterojunctions or annealing⁵³⁻⁵⁶. A preliminary set of experiments was conducted in order to find the optimal C_{60} layer thickness, as seen in Figure 8. The best photocurrent generation as well as PCE was achieved for 50 nm of C_{60} . For consistency, a 50 nm thick fullerene layer was used also in PTh-based devices. The lower C_{60} thickness led to reduced shunt resistance - R_{sh} decreased from $752 \Omega\text{cm}^2$ for 60 nm to $318 \Omega\text{cm}^2$ for 40 nm of C_{60} (with 20 nm of PTh for both cases).

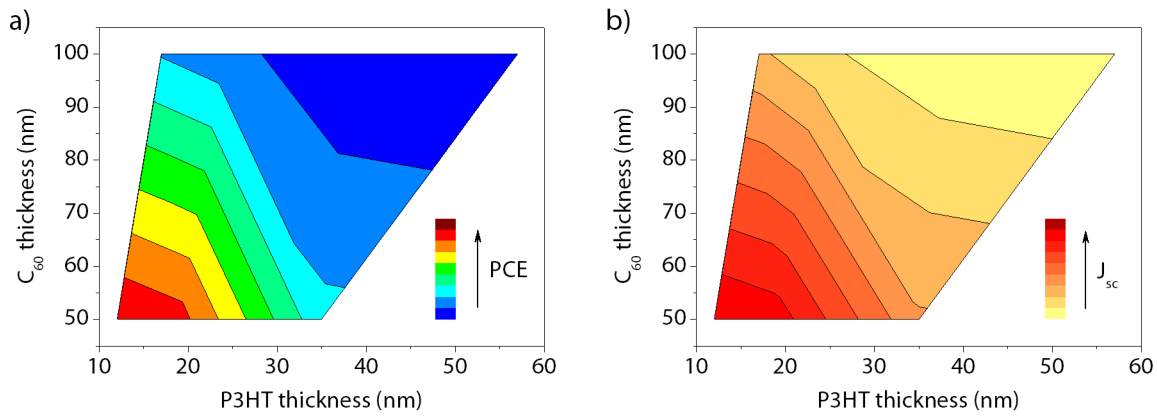


Figure 8. (a) PCE and (b) J_{sc} optimisation of the fullerene thickness in P3HT/ C_{60} planar heterojunction devices.

Following this, the polymer thickness was varied to optimise the overall device performance. Figure 9 plots the main figures of merit, PCE, J_{sc} , V_{oc} , FF, as functions of the donor thickness, with the best cell parameters summarised in Table 2.

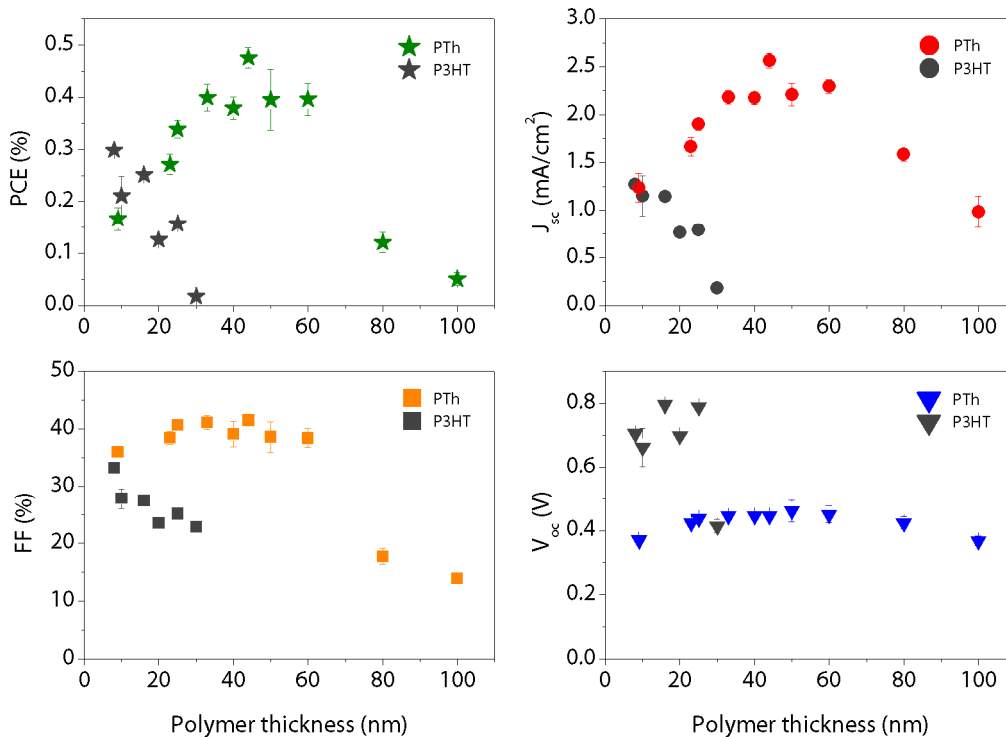


Figure 9. Main figures of merit (PCE, J_{sc} , V_{oc} , FF) as functions of the polymer thickness for ITO/PEDOT:PSS/polymer/Al devices. Thickness of the C_{60} layer was constant 50 nm.

Table 2. Comparison of the main J - V parameters of the best PTh- and P3HT-based devices.

device	thickness [nm]	J_{sc} [mAcm ⁻²]	V_{oc} [V]	FF [%]	PCE [%]
PTh/C ₆₀	44	-2.70	0.45	42.7	0.52
P3HT/C ₆₀	8	-1.30	0.71	32.9	0.30

For P3HT/C₆₀ devices, the best power conversion efficiency PCE = 0.30% was achieved with 8 nm-thick P3HT (Table 2). The value compares favourably to that of spin-coated P3HT/C₆₀ planar heterojunctions reported previously (PCE = 0.17%⁵⁷). The trend of increasing J_{sc} with decreasing P3HT layer thickness probably relates to its poor charge transport properties and short exciton diffusion length⁵⁸. In line with *sections 3.4* and *4.3*, P3HT thicknesses below ~10 nm suffered from low shunt resistance (R_{sh} of 8 nm thick P3HT film was 717 Ωcm^2 as compared to 1377 Ωcm^2 for 12 nm of P3HT).

PTh planar heterojunctions exhibited significantly better performance. Optimal donor thickness was found to be 44 nm, leading to PCE = 0.52% (Table 2). The J - V curves in Figure 10a indicate that the large, almost 70%, increase in efficiency results from enhanced charge extraction in PTh films through improved current parameters $J_{sc\text{ PTh}} = 2.7\text{ mAcm}^{-2}$ and $FF_{\text{PTh}} = 42.7\%$ (compared to $J_{sc\text{ P3HT}} = 1.3\text{ mAcm}^{-2}$, $FF_{\text{P3HT}} = 32.9\%$). Again, the higher photocurrent and the lower rate of recombination correspond well with greater molecular order and hole mobilities. This may also be a result of better structural stability of PTh compared to P3HT, where dissociation of side groups can play various inhibition roles in charge conduction. Absorption of the heterojunctions, shown in Figure 10b, is very similar. PTh/C₆₀ absorbs more light in the blue and red part of the spectrum near 400 and 550 nm,

respectively. When compared to the inset of Figure 10b (absorption profiles of single PTh and P3HT layers), these regions correlate with enhanced PTh absorption.

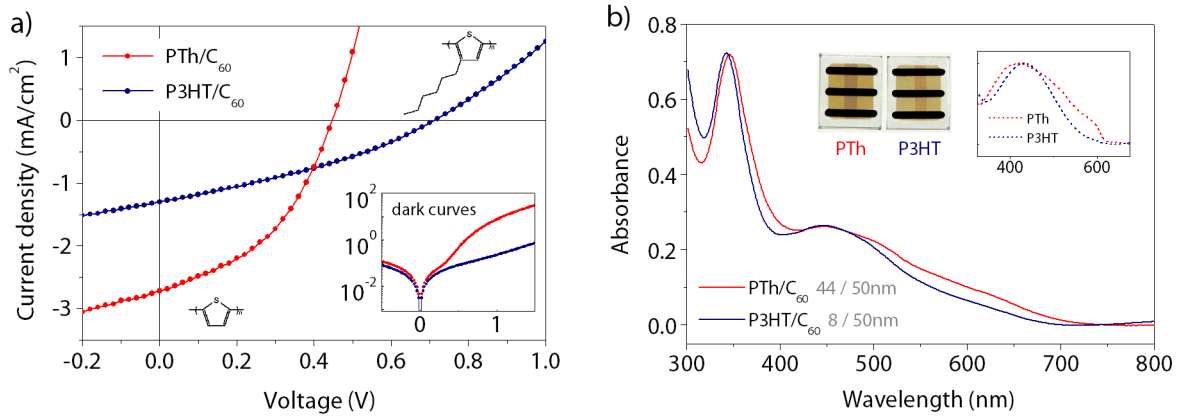


Figure 10. (a) Comparison of J - V characteristics of the best performing PTh/C₆₀ and P3HT/C₆₀ devices under illumination and (inset) in the dark. (b) UV-Vis absorbance spectra of the devices. The inset shows normalised absorption of single PTh and P3HT thin films as well as images of the devices.

The shape of the dark curves (inset of Figure 10a) illustrates the difference in the quality of the donor/acceptor interfaces. While in case of P3HT/C₆₀ poor rectification is observed, the interface of PTh/C₆₀ displays much better diode characteristics. This is reflected also in the better diode ideality factor $n_{\text{PTh}} = 2.59$ of the device (compared to $n_{\text{P3HT}} \approx 4.54$, see Table 3). As in the previous comparison, the series resistance of the polythiophene devices, $R_{s \text{ PTh}} = 25 \Omega\text{cm}^2$, is considerably lower than $R_{s \text{ P3HT}} = 119 \Omega\text{cm}^2$.

Table 3. Comparison of the PTh- and P3HT-based device parameters.

device	n	R_s [Ωcm^2]	R_{sh} [Ωcm^2]	μ_p [$\text{cm}^2\text{V}^{-1}\text{s}^{-1}$]
PTh/C ₆₀	2.59	25	441	2.0×10^{-4}
P3HT/C ₆₀	4.54	119	717	1.1×10^{-6}

Enhanced performance of the PTh/C₆₀ devices is comparable to vacuum-deposited sexithiophene/C₆₀ planar heterojunctions⁵⁹, and untreated polythiophene and poly(alkylthiophene)/C₆₀ bilayers processed in solution^{57, 60}. The limited V_{oc} in PTh/C₆₀ devices could be altered by introduction of an interface layer (LiF, bathocuproine BCP⁴⁷) which increases the device shunt resistance, or simply, by better molecular design for greater separation of the energy levels.

4.6 Optical and morphological properties of planar heterojunction solar cells

Figure 11 compares optical absorption (top) and surface topography (bottom a-b) of two representative PTh/C₆₀ thin films with different thicknesses - 25 and 44 nm PTh under 50 nm of C₆₀. The absorption profile of the heterojunctions seems to be dominated by C₆₀ with PTh influencing the short-wavelength region near 400 nm. This is also where the polymer has the peak of absorption. Spectra of pure PTh and C₆₀ are shown in the inset of Figure 11. MicroXAM images below (Figure 11a-b) show a flat topography of the heterojunction films. RMS roughness is less than 0.2 nm in both cases which corresponds well with the small roughness of PTh (see *section 3.4*) and C₆₀ (Figure 11c) single films.

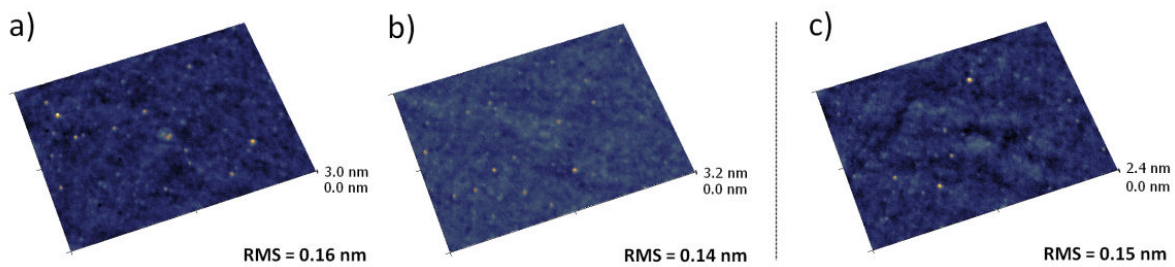
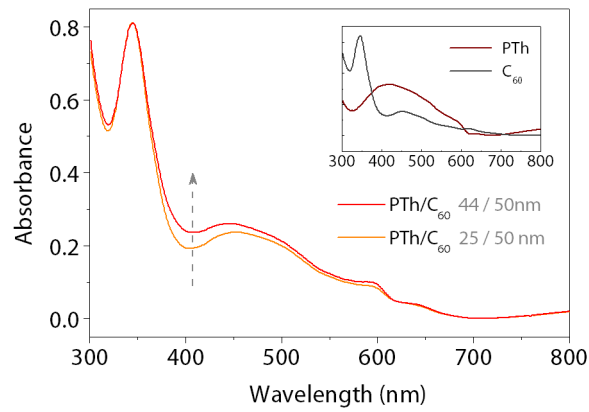


Figure 11. Optical absorption of PTh/ C_{60} planar heterojunctions (top, inset shows spectra of pure 50 nm PTh and 70 nm C_{60} layers) with MicroXAM surface profiles (a-b). A MicroXAM profile of (c) single layer of 70 nm C_{60} is included for comparison.

The XY-scale of the MicroXAM images is 86 x 64 μm .

A similar comparison is made for P3HT/ C_{60} films, as shown in Figure 12. Again, optical absorption of the heterojunctions resembles that of C_{60} and different thicknesses of P3HT (8 and 25 nm) results only in an improvement near 400 nm. Surface topography of the films shows an increase in surface roughness of C_{60} likely due to greater roughening of the underlying P3HT layer (8, 16 and 25 nm as Figure 12a, b, and c, respectively). While shallow pits in an 8 nm average thickness of P3HT are largely filled in by the 50 nm of C_{60} on top, the pits of thicker P3HT layers get deeper (see scans of single P3HT films in *section 3.4*) and hence are reflected in the C_{60} surface topography.

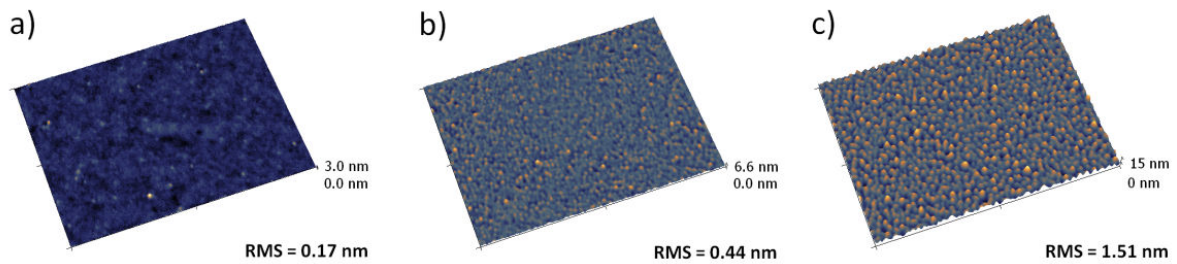
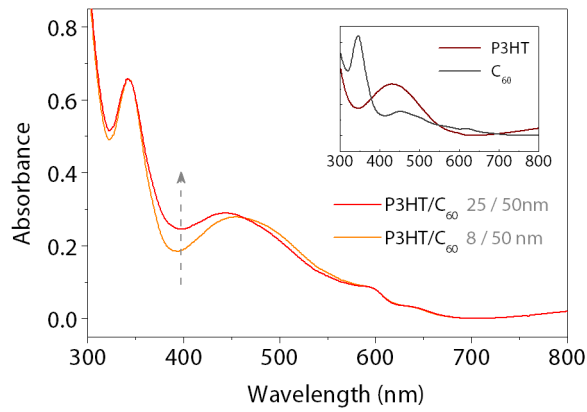


Figure 12. Optical absorption of two P3HT/C₆₀ planar heterojunctions (top, inset shows spectra of 50 nm PTh and 70 nm C₆₀ layers). Below is a development of C₆₀ surface roughness due to underlying (a) 8, (b) 16 and (c) 25 nm of P3HT, as scanned by MicroXAM.

The XY-scale of the images is 86 x 64 μm .

4.7 Effect of illumination intensity on planar heterojunction solar cells

The effect of illumination intensity on the performance of PTh- and P3HT-based devices was investigated, as shown in Figure 13 (a-c PTh/C₆₀ 44/50 nm, and d-f P3HT/C₆₀ 10/50 nm). While in both cases V_{oc} and FF remain relatively constant down to ~ 0.1 sun, J_{sc} exhibits a sub-linear dependence on illumination. As a result, the PCE of the cells at ~ 0.1 sun increases to a maximum of 0.71% for PTh/C₆₀ and 0.49% for P3HT/C₆₀.

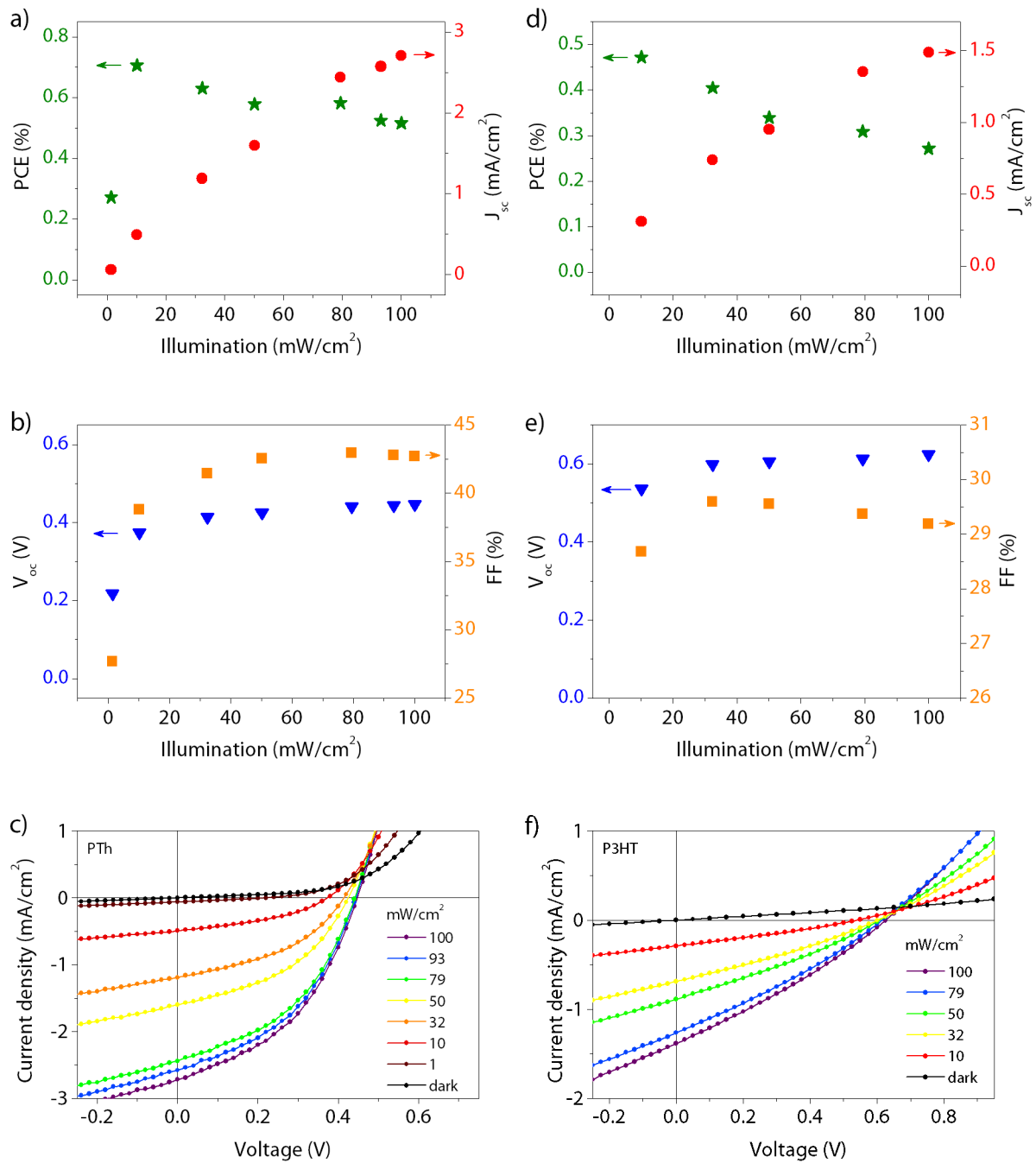


Figure 13. Main photovoltaic parameters and J-V plots of (a-c) PTh/C60 and (d-f) P3HT/C60 heterojunctions under different illumination intensity (0.01-1 sun).

As discussed in *section 1.2.4*, the presence of net charge near the planar heterojunction interface leads to shielding of the internal built-in field and thus increased carrier recombination losses. Behaviour of the devices at different illumination intensities allows

study of the underlying recombination processes. The scaling exponent α from the power-law dependence of the J_{sc} on incident intensity P_0

$$J_{sc} \propto P_0^\alpha \quad (2)$$

can be obtained as an indication of bimolecular (non-geminate) recombination⁶¹. For a linear dependence of J_{sc} on P_0 ($\alpha = 1$), the charge carrier losses are dominated by monomolecular recombination, while a non-linear dependence ($\alpha < 1$) suggests bimolecular recombination, mostly due to space charge effects and imbalanced carrier mobilities⁵¹. By fitting the J_{sc} data in Figure 14a, b with Equation 2 the values of α were calculated for both PTh/ C_{60} and P3HT/ C_{60} heterojunction devices, respectively. These are depicted, along with J_{sc} and PCE , in Table 4.

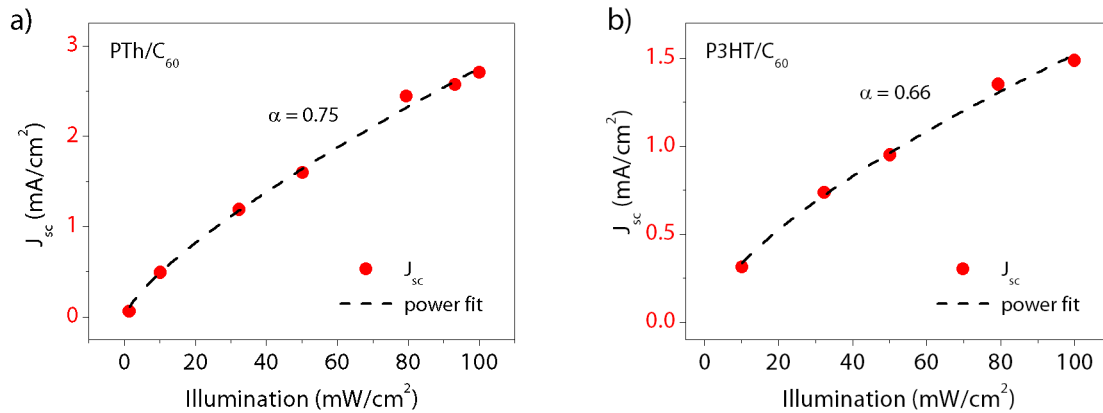


Figure 14. Illumination dependence of (a) PTh and (b) P3HT J_{sc} fitted with a power law. Coefficients alpha are $\alpha = 0.75$ for PTh and $\alpha = 0.66$ for P3HT.

$\alpha < 1$ indicates the presence of bimolecular recombination, more significantly pronounced in P3HT-based devices ($\alpha_{P3HT} < \alpha_{PTh}$). This agrees with the previous finding that bimolecular recombination is the dominant carrier-loss mechanism not only in bulk heterojunction but also in planar heterojunction devices⁶¹. The recombination of the charge carriers takes

place at the polymer/fullerene interface and this is most likely due to the build up of space charge. As the space charge effects are less significant in films with smaller thickness or higher carrier mobilities⁶², this demonstrates that the heterojunctions using PTh as a hole conductor suffer from these effects substantially less than the devices using P3HT.

Table 4. Recombination parameters of PTh and P3HT solar cells.

device	J_{sc} (1 sun) [mAcm ⁻²]	J_{sc} (0.1 sun) [mAcm ⁻²]	PCE (1 sun) [%]	PCE (0.1 sun) [%]	α
PTh/C ₆₀	2.70	0.49	0.52	0.71	0.75
P3HT/C ₆₀	1.49	0.31	0.27	0.48	0.66

4.8 Effect of thermal annealing in planar heterojunction solar cells

The effect of post-production thermal annealing on the performance of PTh/C₆₀ (40/50 nm) and P3HT/C₆₀ (10/50 nm) devices was studied. The annealing temperature of 150 °C was chosen as a temperature which is above T_g of both polymers^{63, 64}. The devices were annealed for 10 min, the standard annealing time used for treatment of other polymer/fullerene planar heterojunctions⁶⁵. Typical device J - V characteristics and EQE response before and after annealing are plotted in Figure 15a-d.

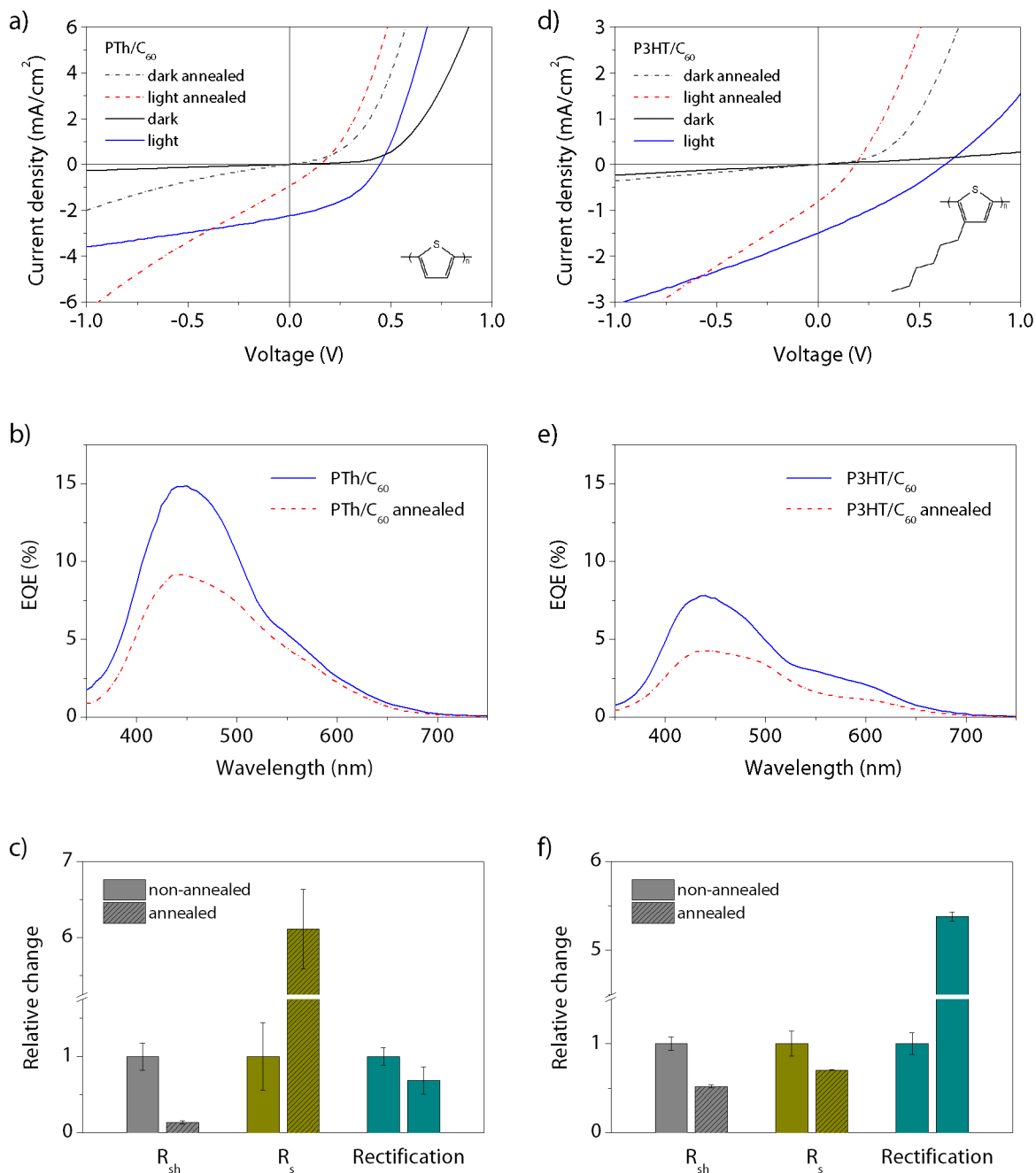


Figure 15. (a) Non-annealed (solid line) and annealed (dashed line) J - V characteristics of the PTh/C₆₀ planar heterojunction device. (b) EQE response before (solid) and after (dashed) annealing. (c) relative changes in R_s , R_{sh} and rectification under illumination before (full) and after (patterned) annealing. (d-f) Characteristics of the P3HT/C₆₀ device.

For both polymer systems, the device performance deteriorates upon annealing. Poor charge extraction in the PTh/C₆₀ device is represented by decreased photocurrent (Figure 15a) and EQE response (Figure 15b). This might be due to increased R_s (Figure 15c)

resulting from unfavourable morphology changes within the polymer or fullerene layer. In addition, annealing significantly reduces R_{sh} and thus lowers V_{oc} . Accordingly, rectification of the PTh/ C_{60} heterojunction worsens as a result of high leakage current. Such changes could be consistent with coarsening of the film due to the growth of larger PTh grains (in line with other findings in *section 5.2* and *section 5.5*). The annealed P3HT/ C_{60} device exhibits similar degradation, as shown in Figure 15d-f. However, R_s improves upon annealing as well as the rectification of the junction. Molecular order in the P3HT film probably improves upon annealing, but the low value of R_{sh} reduces both J_{sc} and V_{oc} .

Contrary to expectations, annealing of vacuum-deposited polymer/fullerene planar heterojunctions does not lead to improved charge extraction and enhanced performance. Morphological development appears to be different to that of the solution-processed systems⁵³⁻⁵⁵. This is probably due to formation of polymer crystals/agglomerates which degrade the overall properties.

4.9 Conclusion

The vacuum thermal deposition of P3HT and PTh has been successfully applied to fabrication of planar heterojunction photovoltaic cells. High molecular order in vacuum-deposited PTh thin films was shown to result in enhanced charge transport properties. This demonstrated that polymer side groups have a strong influence on both structural and electronic properties of vacuum-deposited polymer thin films. PTh/ C_{60} planar heterojunction devices had significantly better current generation and conduction characteristics (J_{sc} , FF), resulting in improved overall PCE by 70% as compared to P3HT/ C_{60} .

Accordingly, EQE of PTh-based devices was almost double that of P3HT. Illumination intensity studies revealed non-linear dependence of J_{sc} on power intensity, suggesting space charge effects and a significant amount of bimolecular recombination. PCE of PTh/C₆₀ and P3HT/C₆₀ bilayers at low illumination (0.1 sun) was 0.71% and 0.49%, respectively. Post-production thermal annealing of the devices lead to deteriorated performance due to reduced shunt resistance.

4.10 References

1. Bredas, J. L.; Themans, B.; Fripiat, J. G.; Andre, J. M.; Chance, R. R. *Physical Review B* **1984**, 29, (12), 6761-6773.
2. Chen, T. A.; Wu, X. M.; Rieke, R. D. *Journal of the American Chemical Society* **1995**, 117, (1), 233-244.
3. Zhan, X. W.; Zhu, D. B. *Polymer Chemistry* **2010**, 1, (4), 409-419.
4. Ho, H. A.; Boissinot, M.; Bergeron, M. G.; Corbeil, G.; Dore, K.; Boudreau, D.; Leclerc, M. *Angewandte Chemie-International Edition* **2002**, 41, (9), 1548-1551.
5. Torsi, L.; Dodabalapur, A.; Sabbatini, L.; Zambonin, P. G. *Sensors and Actuators B-Chemical* **2000**, 67, (3), 312-316.
6. Sirringhaus, H.; Brown, P. J.; Friend, R. H.; Nielsen, M. M.; Bechgaard, K.; Langeveld-Voss, B. M. W.; Spiering, A. J. H.; Janssen, R. A. J.; Meijer, E. W.; Herwig, P.; de Leeuw, D. M. *Nature* **1999**, 401, (6754), 685-688.
7. Sirringhaus, H. *Advanced Materials* **2005**, 17, (20), 2411-2425.
8. Park, S. H.; Roy, A.; Beaupre, S.; Cho, S.; Coates, N.; Moon, J. S.; Moses, D.; Leclerc, M.; Lee, K.; Heeger, A. J. *Nature Photonics* **2009**, 3, (5), 297-U5.
9. Dennler, G.; Scharber, M. C.; Brabec, C. J. *Advanced Materials* **2009**, 21, (13), 1323-1338.
10. Kraft, A.; Grimsdale, A. C.; Holmes, A. B. *Angewandte Chemie-International Edition* **1998**, 37, (4), 402-428.
11. Perepichka, I. F.; Perepichka, D. F.; Meng, H.; Wudl, F. *Advanced Materials* **2005**, 17, (19), 2281-2305.

12. Yamamoto, T.; Komarudin, D.; Arai, M.; Lee, B. L.; Suganuma, H.; Asakawa, N.; Inoue, Y.; Kubota, K.; Sasaki, S.; Fukuda, T.; Matsuda, H. *Journal of the American Chemical Society* **1998**, 120, (9), 2047-2058.
13. McCullough, R. D. *Advanced Materials* **1998**, 10, (2), 93-+.
14. Brown, P. J.; Thomas, D. S.; Kohler, A.; Wilson, J. S.; Kim, J. S.; Ramsdale, C. M.; Sirringhaus, H.; Friend, R. H. *Physical Review B* **2003**, 67, (6).
15. Park, Y. D.; Kim, D. H.; Jang, Y.; Cho, J. H.; Hwang, M.; Lee, H. S.; Lim, J. A.; Cho, K. *Organic Electronics* **2006**, 7, (6), 514-520.
16. Gevorgyan, S. A.; Krebs, F. C. *Chemistry of Materials* **2008**, 20, (13), 4386-4390.
17. Jen, K. Y.; Miller, G. G.; Elsenbaumer, R. L. *Journal of the Chemical Society-Chemical Communications* **1986**, (17), 1346-1347.
18. Inganas, O.; Salaneck, W. R.; Osterholm, J. E.; Laakso, J. *Synthetic Metals* **1988**, 22, (4), 395-406.
19. Kim, Y.; Cook, S.; Tuladhar, S. M.; Choulis, S. A.; Nelson, J.; Durrant, J. R.; Bradley, D. D. C.; Giles, M.; McCulloch, I.; Ha, C. S.; Ree, M. *Nature Materials* **2006**, 5, (3), 197-203.
20. Prosa, T. J.; Winokur, M. J.; Moulton, J.; Smith, P.; Heeger, A. J. *Macromolecules* **1992**, 25, (17), 4364-4372.
21. Gadisa, A.; Oosterbaan, W. D.; Vandewal, K.; Bolsee, J. C.; Bertho, S.; D'Haen, J.; Lutsen, L.; Vanderzande, D.; Manca, J. V. *Advanced Functional Materials* **2009**, 19, (20), 3300-3306.
22. Cho, K.; Park, Y. D.; Kim, D. H.; Jang, Y.; Cho, J. H.; Hwang, M.; Lee, H. S.; Lim, J. A. *Organic Electronics* **2006**, 7, (6), 514-520.
23. Kaneto, K.; Lim, W. Y.; Takashima, W.; Endo, T.; Rikukawa, M. *Japanese Journal of Applied Physics Part 2-Letters* **2000**, 39, (8B), L872-L874.
24. Chen, S. A.; Liao, C. S. *Macromolecules* **1993**, 26, (11), 2810-2816.
25. Nakahara, H.; Nakayama, J.; Hoshino, M.; Fukuda, K. *Thin Solid Films* **1988**, 160, (1-2), 87-97.
26. Bjornholm, T.; Hassenkam, T.; Reitzel, N. *Journal of Materials Chemistry* **1999**, 9, (9), 1975-1990.
27. Valaski, R.; Canestraro, C. D.; Micaroni, L.; Mello, R. M. Q.; Roman, L. S. *Solar Energy Materials and Solar Cells* **2007**, 91, (8), 684-688.
28. Yu, J. W.; Kim, S. Y.; Lee, K. H.; Chin, B. D. *Solar Energy Materials and Solar Cells* **2009**, 93, (1), 129-135.
29. Advincula, R.; Grande, C. D.; Tria, M. C.; Jiang, G. Q.; Ponnampati, R. *Macromolecules* **2011**, 44, (4), 966-975.
30. Liu, J. S.; Kadnikova, E. N.; Liu, Y. X.; McGehee, M. D.; Frechet, J. M. J. *Journal of the American Chemical Society* **2004**, 126, (31), 9486-9487.
31. Krebs, F. C.; Bjerring, M.; Nielsen, J. S.; Nielsen, N. C. *Macromolecules* **2007**, 40, (16), 6012-6013.

32. Ho, K. C.; Wei, H. Y.; Huang, J. H.; Chu, C. W. *Acs Applied Materials & Interfaces* **2010**, 2, (5), 1281-1285.
33. Krebs, F. C. *Solar Energy Materials and Solar Cells* **2009**, 93, (4), 394-412.
34. Krebs, F. C.; Jorgensen, M.; Norrman, K.; Hagemann, O.; Alstrup, J.; Nielsen, T. D.; Fyenbo, J.; Larsen, K.; Kristensen, J. *Solar Energy Materials and Solar Cells* **2009**, 93, (4), 422-441.
35. Bredas, J. L.; Norton, J. E.; Cornil, J.; Coropceanu, V. *Accounts of Chemical Research* **2009**, 42, (11), 1691-1699.
36. Goh, C.; Kline, R. J.; McGehee, M. D.; Kadnikova, E. N.; Frechet, J. M. J. *Applied Physics Letters* **2005**, 86, (12).
37. Salzner, U.; Lagowski, J. B.; Pickup, P. G.; Poirier, R. A. *Synthetic Metals* **1998**, 96, (3), 177-189.
38. Po, R.; Carbonera, C.; Bernardi, A.; Camaioni, N. *Energy & Environmental Science* **2011**, 4, (2), 285-310.
39. Brocks, G. *Journal of Chemical Physics* **2000**, 112, (12), 5353-5363.
40. Chirvase, D.; Chiguvare, Z.; Knipper, A.; Parisi, J.; Dyakonov, V.; Hummelen, J. C. *Synthetic Metals* **2003**, 138, (1-2), 299-304.
41. Mihailetchi, V. D.; Xie, H. X.; de Boer, B.; Koster, L. J. A.; Blom, P. W. M. *Advanced Functional Materials* **2006**, 16, (5), 699-708.
42. Takshi, A.; Dimopoulos, A.; Madden, J. D. *Applied Physics Letters* **2007**, 91, (8).
43. Hoppe, H.; Sariciftci, N. S. *Journal of Materials Research* **2004**, 19, (7), 1924-1945.
44. Brabec, C. J.; Sariciftci, N. S.; Hummelen, J. C. *Advanced Functional Materials* **2001**, 11, (1), 15-26.
45. Scharber, M. C.; Wuhlbacher, D.; Koppe, M.; Denk, P.; Waldauf, C.; Heeger, A. J.; Brabec, C. L. *Advanced Materials* **2006**, 18, (6), 789-+.
46. Peumans, P.; Forrest, S. R. *Applied Physics Letters* **2001**, 79, (1), 126-128.
47. Chang, C. C.; Lin, C. F.; Chiou, J. M.; Ho, T. H.; Tai, Y.; Lee, J. H.; Chen, Y. F.; Wang, J. K.; Chen, L. C.; Chen, K. H. *Applied Physics Letters* **2010**, 96, (26).
48. Su, M. S.; Kuo, C. Y.; Yuan, M. C.; Jeng, U. S.; Su, C. J.; Wei, K. H. *Advanced Materials* **2011**, 23, (29), 3315-+.
49. van Bavel, S. S.; Barenklau, M.; de With, G.; Hoppe, H.; Loos, J. *Advanced Functional Materials* **2010**, 20, (9), 1458-1463.
50. Perez, M. D.; Borek, C.; Forrest, S. R.; Thompson, M. E. *Journal of the American Chemical Society* **2009**, 131, (26), 9281-9286.
51. Cowan, S. R.; Roy, A.; Heeger, A. J. *Physical Review B* **2010**, 82, (24).
52. Miller, S.; Fanchini, G.; Lin, Y. Y.; Li, C.; Chen, C. W.; Su, W. F.; Chhowalla, M. *Journal of Materials Chemistry* **2008**, 18, (3), 306-312.

53. Ayzner, A. L.; Tassone, C. J.; Tolbert, S. H.; Schwartz, B. J. *Journal of Physical Chemistry C* **2009**, 113, (46), 20050-20060.
54. Chen, D.; Liu, F.; Wang, C.; Nakahara, A.; Russell, T. P. *Nano Letters* **2011**, 11, (5), 2071-2078.
55. Moon, J. S.; Takacs, C. J.; Sun, Y. M.; Heeger, A. J. *Nano Letters* **2011**, 11, (3), 1036-1039.
56. Lee, K. H.; Schwenn, P. E.; Smith, A. R. G.; Cavaye, H.; Shaw, P. E.; James, M.; Krueger, K. B.; Gentle, I. R.; Meredith, P.; Burn, P. L. *Advanced Materials* **2011**, 23, (6), 766-+.
57. Kim, J. S.; Park, Y.; Lee, D. Y.; Lee, J. H.; Park, J. H.; Kim, J. K.; Cho, K. *Advanced Functional Materials* **2010**, 20, (4), 540-545.
58. Shaw, P. E.; Ruseckas, A.; Samuel, I. D. W. *Advanced Materials* **2008**, 20, (18), 3516-+.
59. Sakai, J.; Taima, T.; Saito, K. *Organic Electronics* **2008**, 9, (5), 582-590.
60. Geiser, A.; Fan, B.; Benmansour, H.; Castro, F.; Heier, J.; Keller, B.; Mayerhofer, K. E.; Nuesch, F.; Hany, R. *Solar Energy Materials and Solar Cells* **2008**, 92, (4), 464-473.
61. Credgington, D.; Kim, Y.; Labram, J.; Anthopoulos, T. D.; Durrant, J. R. *Journal of Physical Chemistry Letters* **2011**, 2, (21), 2759-2763.
62. Scully, S. R., *Exciton Transport, Charge Extraction, and Loss Mechanisms in Organic Photovoltaics*. ProQuest: 2009; p 133
63. Chen, S. A.; Ni, J. M. *Macromolecules* **1992**, 25, (23), 6081-6089.
64. Zhao, Y.; Yuan, G. X.; Roche, P.; Leclerc, M. *Polymer* **1995**, 36, (11), 2211-2214.
65. Dang, M. T.; Hirsch, L.; Wantz, G. *Advanced Materials* **2011**, 23, (31), 3597-3602.

5.1 Introduction

In the pursuit of high organic photovoltaic power conversion efficiencies there is fierce competition between solution and vacuum processing¹⁻³. The former relies on the good morphology control of polymer-fullerene blends via phase separation⁴. The latter takes advantage of solvent-free processing which allows for a high degree of complexity to be used in the device architecture⁵. The completely different approaches have demonstrated similarly high efficiencies and both have shown the potential for low-cost scale-up by means of roll-to-roll processing^{6, 7}. In this chapter, polymer-fullerene blends are co-deposited by thermal evaporation in an attempt to develop a vacuum-processed bulk heterojunction with an enhanced degree of morphology control. The relationship between morphology and performance is studied by controlling the polymer-fullerene composition ratio and post-production thermal annealing conditions.

The intimate blend of donor and acceptor in a bulk heterojunction (BHJ) allows efficient exciton dissociation and charge extraction through an interpenetrated nanoscale network of the two phases. This architecture has demonstrated the ability to reach 100% internal quantum efficiency⁸ and as such has long become a standard platform for fabrication of devices with state-of-the-art performance⁹. In solution processing, the two most common ways of controlling morphology are choice of solvent and application of post-production

thermal annealing¹⁰. Vacuum-deposited BHJs are made by thermal co-evaporation of a molecular donor and acceptor. Morphology can be controlled via in-situ^{11, 12} and ex-situ thermal annealing^{13, 14}, and evaporation additives¹⁵. The approach allows deposition of gradient blends and therefore precise manipulation of horizontal as well as vertical donor-acceptor composition^{16, 17}. However, morphology control in vacuum-processed BHJs remains a big challenge. Co-deposition of small molecules often results in an almost homogeneous blend of the constituents with insufficient percolation pathways¹⁸. Due to the ease of crystallisation of small molecules, post-production thermal annealing of such blends does not lead to establishment/enhancement of the interpenetrated network but rather to nucleation and growth of microcrystals^{13, 19-21}, as illustrated in Figure 1. Co-evaporated BHJs have therefore often exhibited worse performance than their planar heterojunction counterparts^{13, 18, 21-24}, and only rarely can these systems be improved with annealing^{13, 14}.

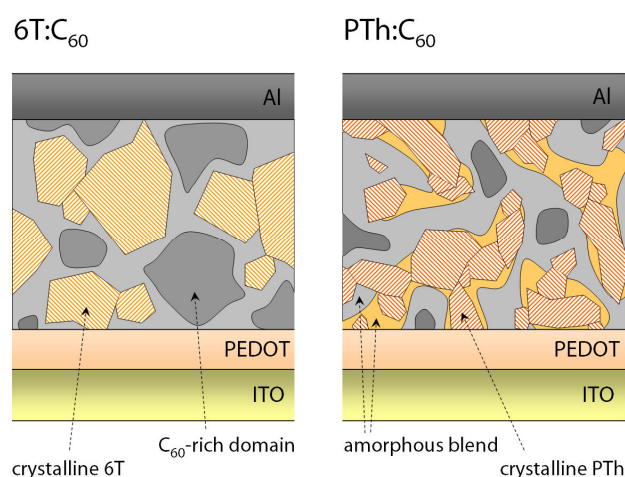


Figure 1. Proposed morphology in 6T:C₆₀ and PTh:C₆₀ bulk heterojunction systems. The left picture represents crystalline 6T (orange pattern) and crystalline C₆₀ (dark grey) within an amorphous 6T:C₆₀ blend (light grey). The right picture represents semicrystalline phase-separated PTh (red pattern and orange solid) and crystalline C₆₀ (dark grey) within an amorphous PTh:C₆₀ blend (light grey).

This chapter demonstrates use of polymeric materials for well-controlled nano-scale phase separation in a vacuum deposition system which allows further development of the device complexity. By blending PTh:C₆₀ a 60% increase in photocurrent in comparison with the PTh/C₆₀ planar heterojunction described in *section 4.5* is achieved. Using different polymer-fullerene compositions the effect of post-production thermal annealing on the development of morphology is studied. Post-annealing treatment is shown to improve the interpenetrated polymer-fullerene network and enhance efficiency by as much as 80%. Direct comparison of PTh with 6T shows that morphological behaviour of the vacuum-deposited polymer blends differs from that of small-molecule (oligomer) systems.

5.2 Optimisation of annealing parameters in PTh:C₆₀ blends

Performance and morphology of vacuum co-deposited BHJs was studied through variation of four main parameters - active layer thickness, polymer-fullerene composition, and post-production thermal annealing temperature and time. In order to see the effect of annealing on different PTh:C₆₀ compositions, optimisation of the annealing temperature and time had to be performed. A series of initial experiments, summarised in Figure 2, indicated that a BHJ with dominant ratio of C₆₀ (80%) and thickness of 70 nm lead to device characteristics comparable to the previously fabricated planar heterojunction devices ($J_{sc} \sim 2-3 \text{ mAcm}^{-2}$ and $V_{oc} \sim 0.40-0.45 \text{ V}$, see *section 4.5*). This composition thus served as a good standard for optimisation of the annealing parameters.

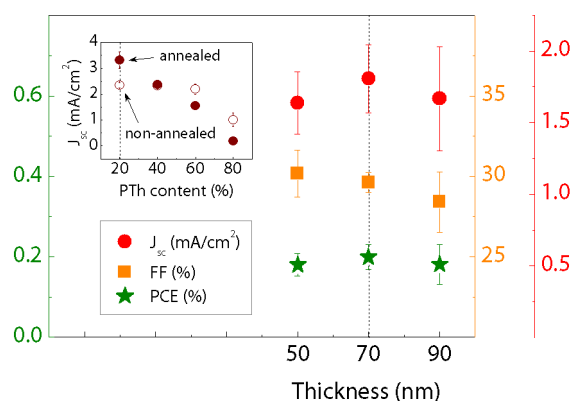


Figure 2. Initial optimisation of the 20% PTH:C₆₀ blend thickness. The inset depicts preliminary photocurrent studies of different PTH:C₆₀ compositions. The annealing conditions were taken from the Sakai *et al.*'s work¹⁴ on 20% 6T:C₇₀, i.e. at 140 °C for 20 min.

First, the optimal annealing temperature was found by annealing the devices for 10 min at different temperatures (100, 120, 140 and 160 °C), and subsequently, the optimal annealing time was found for the optimised temperature (from 5, 15, 30 and 60 min annealing at 120 °C). Both steps are shown in Figure 3a, b. The best performance was obtained for 30 min annealing at 120 °C, the temperature previously assigned by Chen *et al.* to the glass transition of PTh²⁵. The glass transition of the PTh:C₆₀ system might, however, be lower with C₆₀ acting as a plasticiser of PTh²⁶. The resulting increase in photocurrent after annealing was about 35% and PCE about 55%. It was also observed that above 120 °C the value of V_{oc} consistently decreases. This could be a result of phase segregation and crystallisation of one of the phases (see inset of Figure 3a) leading to the formation of shunt paths. In line with *section 5.6*, the crystallizing phase is likely to be C₆₀. The device R_{sh} decreases from 124 Ωcm^2 at 120 °C to 106 Ωcm^2 at 140 °C.

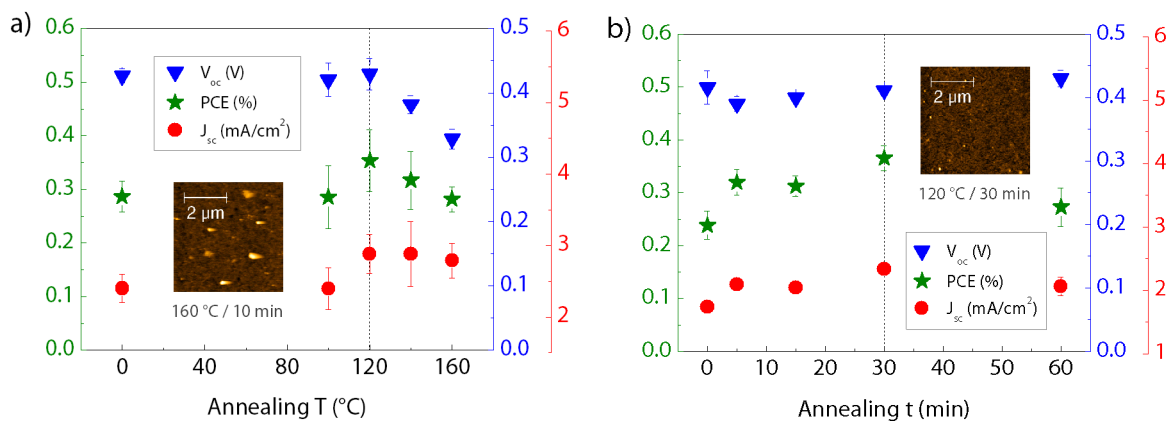


Figure 3. Optimisation of the (a) annealing temperature and (b) time in 20% PTh:C₆₀ bulk heterojunctions. The insets show (a) coarsening of the surface for high-temperature annealing and (b) smooth topography resulting from optimised annealing conditions as imaged by AFM.

The z-scale in both AFM images is 30 nm.

5.3 Effect of thermal annealing on different PTh:C₆₀ blend compositions

Performance of BHJ solar cells is greatly affected by the volume ratio between the donor and the acceptor phases²⁷⁻²⁹. In order to investigate this effect in our vacuum-deposited polymer-fullerene system, BHJs with different volume ratios of PTh (20, 40, 60 and 80%) were fabricated and divided into two groups – non-annealed and annealed. Both device groups were then studied and compared in terms of electronic performance and morphology. Light and dark J-V characteristics of representative devices with different composition are shown in Figure 4a, and a summary of the photovoltaic characteristics is shown in Figure 4b and Table 1.

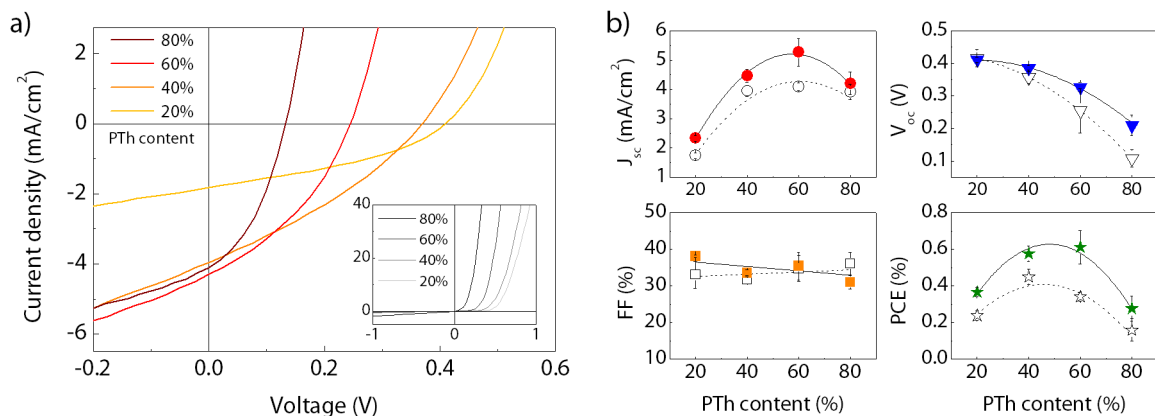


Figure 4. (a) J-V characteristics of representative non-annealed PTh:C₆₀ BHJs with different compositions. Dark J-V curves are included in the inset. (b) Summary of the main photovoltaic parameters of the devices before (empty symbols) and after (full symbols) thermal annealing.

Figure 4a shows that increasing polymer content (up to 60%) results in improved current generation which in turn seems to be the main factor that drives the PCE in this BHJ system. Enhanced diode characteristics in light and dark curves, Figure 4a (40-80% PTh), and decreasing series resistance R_s , Table 1 (40-60% PTh), are all consistent with the photocurrent increase. The films with higher PTh content show better overlap with the solar spectrum, as seen below in Figure 6b, *section 5.5*. This improvement in absorption, however, could only be partially responsible for the J_{sc} increase, as the trend in absorption with PTh content does not correlate well with that in J_{sc} .

Table 1. Typical values of series resistance (R_s), shunt resistance (R_{sh}) and saturation for PTh:C₆₀ bulk heterojunctions with different compositions.

PTh content (%)	R_s [Ωcm^2]		R_{sh} [Ωcm^2]		Saturation / $J(-0.5V)/J_{sc}$	
	non-annealed	annealed	non-annealed	annealed	non-annealed	annealed
20	72.1	16.8	234.5	280.0	1.74	1.71
40	3.7	4.2	138.7	167.1	1.70	1.46
60	3.2	1.5	124.5	204.9	1.51	1.32
80	4.1	24.3	113.9	67.1	1.57	1.50

The low fill factor (FF) suggests charge recombination and any improvement with increasing PTh content (for non-annealed devices) is minor. Open circuit voltage of donor-acceptor heterojunctions is determined by the HOMO level of the donor and LUMO level of the^{30, 31}. However, a systematic decrease in V_{oc} is observed, apparent in Figure 4b, which is attributed to decreasing shunt resistance R_{sh} of the devices (Table 1). This could be ascribed to a higher content of crystalline PTh which could introduce more shunt paths and thereby lower R_{sh} . A similar trend has been observed in both solution- and vacuum-processed BHJs^{32, 33}.

The annealed devices show a clear enhancement in performance, with some of them improving their efficiencies by as much as 80%. The average increase in J_{sc} is approximately 20-30%. Thermal annealing not only improves the photocurrent, but also increases R_{sh} of the devices (for 40-60% PTh) and consequently enhances the values of V_{oc} . This probably happens through sealing of the shunts created during the film growth³⁴. The exception is at high (80%) concentration of PTh, for which a rather unexpected drop in R_{sh} is calculated. It

is also the only case in which FF decreases after annealing, possibly as a result of coarsening of the blend. The other photovoltaic characteristics remain largely consistent with the ones of the non-annealed devices.

In general, the best performance of the vacuum-deposited PTh:C₆₀ devices, both before and after annealing, was found to peak between 40-60% PTh with devices exhibiting efficiencies around 0.7%. The bulk heterojunction system showed more than 200% improvement in J_{sc} in comparison with the optimised planar heterojunction PTh/C₆₀ (see *section 4.5*). Moreover, this donor-acceptor ratio corresponds well with the percolation model of blend films, in which ratios close to optimal 1:1 have the highest interface-to-volume ratio as well as the most-balanced percolation and charge carrier transport in the phases³⁵. Table 2 compares photovoltaic characteristics of co-evaporated PTh:C₆₀ cells with PTh:PCBM BHJs processed in solution from thermo-cleavable precursors³⁶, and vacuum-deposited 6T:C₆₀(C₇₀) devices^{14, 33} (enhanced parameters of the 6T-based cells result from the use of more complex device architecture and/or better absorbing acceptor C₇₀).

Table 2. Photovoltaic characteristics of selected oligo-/poly-thiophene BHJ systems. The bottom row is data from this work.

device architecture	process	J_{sc} [mAcm ⁻²]	V_{oc} [V]	FF [%]	PCE [%]
ITO/PEDOT:PSS/PTh:C ₆₀ /Al ³⁶ <i>converted from precursor at 310 °C</i>	solution	4.5	0.47	34	0.7
ITO/PEDOT:PSS/6T:C ₆₀ /BCP/Ag:Mg ³³ <i>non-annealed</i>	vacuum	5.6	0.68	39	1.5
ITO/PEDOT:PSS/6T:C ₇₀ /BCP/Ag:Mg ¹⁴ <i>non-annealed</i>	vacuum	7.8	0.39	38	1.2
ITO/PEDOT:PSS/6T:C ₇₀ /BCP/Ag:Mg ¹⁴ <i>annealed 140 °C / 20 min</i>	vacuum	9.2	0.58	45	2.4
ITO/PEDOT:PSS/PTh:C ₆₀ /Al <i>annealed 120 °C / 30 min</i>	<i>vacuum</i>	<i>5.7</i>	<i>0.34</i>	<i>39</i>	<i>0.7</i>

Although overall performance of the PTh:C₆₀ devices did not match that of solution-cast P3HT:PCBM devices (average PCE 3%)³⁷, it needs to be emphasised that PTh is not optimised to form vacuum-deposited heterojunction with C₆₀, in the way that P3HT is optimised for solution-processed heterojunction with PCBM. Better molecular design is necessary to adjust the energy levels of the polymer and thus improve absorption as well as its alignment with the acceptor for greater V_{oc} .

5.4 Effect of thermal annealing on charge extraction processes

The origin of recombination in two representative sets of BHJs was investigated - one near the peak performance (40% PTh) and one with a higher polymer ratio (80% PTh).

Illumination studies of the devices showed that J_{sc} follows sublinear dependence on the incident light intensity P_0 (unfortunately only two illumination intensities were used for the device set in question, however, the gradient of the fit was consistent with other measurements made on similar devices through the study). This is indicative of bimolecular recombination which is one of the major carrier losses in all organic BHJ cells^{38, 39}. The probable pathway is charge recombination across the interface of the materials, most likely caused by the accumulation of carriers in one of the phases due to imbalanced electron/hole mobilities and build up of space charge³⁸. From the power-law dependence $J_{sc} \propto P_0^\alpha$, values of α were obtained serving as a measure of the recombination losses³⁹. These are depicted along with the other main parameters J_{sc} and PCE in Table 3.

Table 3. J_{sc} and PCE of 40 and 80% PTh:C₆₀ BHJs under different illumination (0.1 and 1 sun). Calculated α for respective devices.

device	J_{sc} (1 sun) [mAcm ⁻²]	J_{sc} (0.1 sun) [mAcm ⁻²]	PCE (1 sun) [%]	PCE (0.1 sun) [%]	α
40% PTh:C ₆₀	3.94	0.72	0.46	0.70	0.74
40% PTh:C ₆₀ annealed	4.68	0.79	0.62	0.79	0.78
80% PTh:C ₆₀	4.09	0.57	0.22	0.22	0.86
80% PTh:C ₆₀ annealed	4.57	0.65	0.32	0.25	0.85

The coefficient $\alpha \sim 0.75$ for non-annealed 40% PTh BHJ suggests bimolecular recombination arising from space charge effects³⁹. Its value, however, improves with annealing which indicates that enhancement of the donor-acceptor network takes place. The value of α of BHJs with 80% PTh is much higher, implying a lower rate of bimolecular recombination. This means that the devices having such an unequal blend composition are still able to generate photocurrents comparable to 40-60% PTh heterojunctions, as seen in

Figure 4b. In this case the change in α on annealing is only small, showing that annealing has less effect on recombination in the blend with high PTh content. These findings illustrate that the rate of bimolecular recombination is strongly dependent on composition and annealing parameters, and as such is closely related to active layer morphology.

Finally, the EQE was measured to determine the photoconversion efficiency of the PTh:C₆₀ system. For this experiment, a device with 1:1 ratio of PTh:C₆₀ was fabricated (with current characteristics similar to the heterojunctions with 40% and 60% of PTh, i.e. $J_{sc} = 3.9 \text{ mAcm}^{-2}$ and FF = 35%). The EQE response of the device before and after annealing (at 120 °C for 20 min) is shown in Figure 5a.

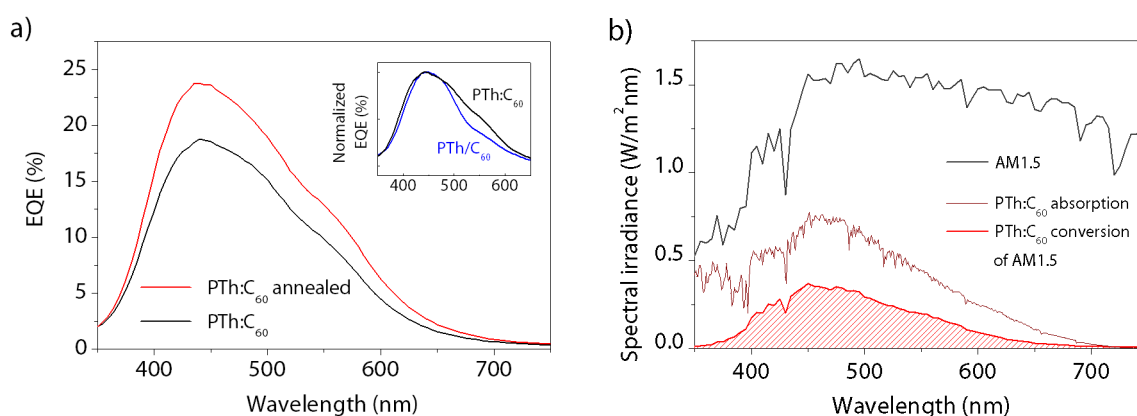


Figure 5. (a) Non-annealed (black line) and annealed (red line) EQE response of the 1:1 PTh:C₆₀ bulk heterojunction. The inset shows an EQE comparison of the non-annealed BHJ (black line) and a non-annealed PTh/C₆₀ 40/50 nm bilayer (blue line), both curves are normalised. (b) Portion of the AM1.5 illumination absorbed (thin red line) and converted into electricity (thick red line with the patterned area) by the annealed 1:1 PTh:C₆₀ device.

As in the other BHJ systems (*section 5.3*), the photocurrent increase of approximately 30% was observed upon annealing, leading to significantly better charge extraction ($J_{sc} = 5.2 \text{ mAcm}^{-2}$ and FF = 36%) and higher EQE. The peak efficiency at 440 nm improved from 18.8% to 23.8%. This value is ~60% higher than the peak EQE value of the PTh/C₆₀ bilayer

device from *section 4.8*. Moreover, the inset of Figure 5a shows overall broadening of the EQE response of a bulk heterojunction in comparison to that of a planar heterojunction (plotted are non-annealed devices). This probably results from a higher contribution of PTh to the collected photocurrent. The strengthening of the 500-600 nm region implies that more charges originating from PTh are extracted due to efficient exciton dissociation within the blend.

Figure 5b illustrates the amount of solar AM1.5 radiation that is absorbed by the annealed PTh:C₆₀ heterojunction and converted into electricity. The curve is inferred from the device EQE response. Although the power conversion efficiency of the cell is relatively poor, its internal quantum efficiency is significant when the low device absorption is considered. Simple calculation of the electron/photon ratio (using the EQE and absorption curves, respectively) estimates the IQE to be higher than 50% for many of the wavelengths. The device reflectance is an unknown loss. Such efficient conversion of the absorbed photons to electrons is comparable to optimised P3HT:PCBM systems⁴⁰⁻⁴³ and demonstrates the good morphology of the PTh:C₆₀ interpenetrated network.

5.5 Development of morphology in annealed PTh:C₆₀ blends

Improvement in photocurrent after annealing implies enhanced charge generation due to increased absorption, and/or better charge extraction through more efficient exciton dissociation and charge collection at the electrodes^{28, 44}. To understand this, a combination of XRD, UV-Vis absorption spectroscopy and AFM was used.

The crystal structure of PTh-only does not change upon annealing as the XRD traces in Figure 6a show. This suggests that enhanced charge extraction cannot come from further polymer crystallisation which would provide better hole transport⁴⁵. Neither does the increased photocurrent result from increased absorption of the annealed films, as can be seen in Figure 6b. The absorbance remains unchanged for all of the PTh:C₆₀ compositions owing to the already crystalline nature of vacuum-deposited PTh. These findings thus imply that it is a purely morphological development of the polymer-fullerene network that drives the increase in PCE.

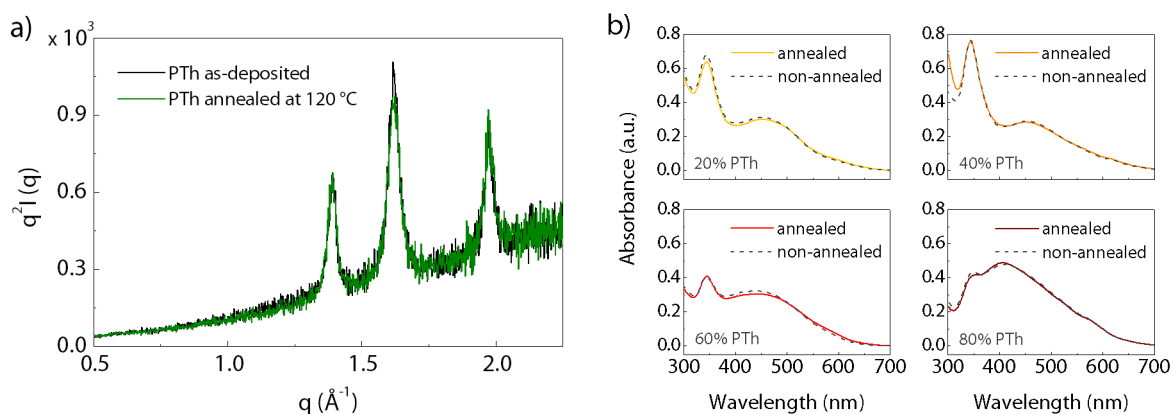


Figure 6. (a) XRD patterns of a thick single layer of PTh as-deposited (black line) and annealed at 120 °C for 20 min (green line). (b) Optical absorption of the PTh:C₆₀ blends before (dotted line) and after (full line) annealing.

The XRD traces of the 1:1 PTh:C₆₀ composition, shown in Figure 7, confirm that there is no significant increase in PTh crystallinity upon annealing either. Intensities of the characteristic PTh peaks at 19.6°, 22.8° and 28° remain similar^{46, 47}. This shows that, despite relatively high amount of PTh (50%) present within the blend, no excessive crystallisation occurs which would lead to strong phase segregation and device shorting. In contrast to the constancy of the PTh peaks, the relative intensity of the C₆₀ peaks⁴⁸ appears more

pronounced after annealing. Development of the donor-acceptor network on annealing is driven by crystallisation and re-arrangement of C_{60} on phase separation from the PTh.

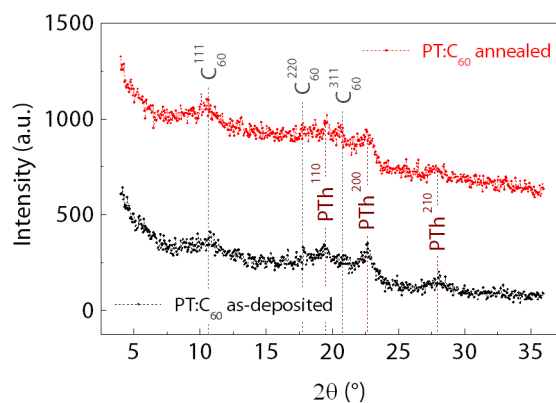


Figure 7. XRD traces of 50% PTh: C_{60} blend before (black) and after (red) thermal annealing. Dashed lines indicate position of the main PTh and C_{60} diffraction peaks.

In order to relate photovoltaic performance of the devices to their morphology, AFM topographic and phase-contrast studies were performed, with representative images summarised in Figure 8. The value of root-mean-square (RMS) surface roughness, taken from multiple samples and scan areas, is shown in Figure 9a. The phase images contain not only information on lateral surface morphology but also on materials' properties, such as viscoelasticity and adhesion. Their quantification is represented by the average peak-to-peak distance of domains in the phase images, as shown in Figure 9b.

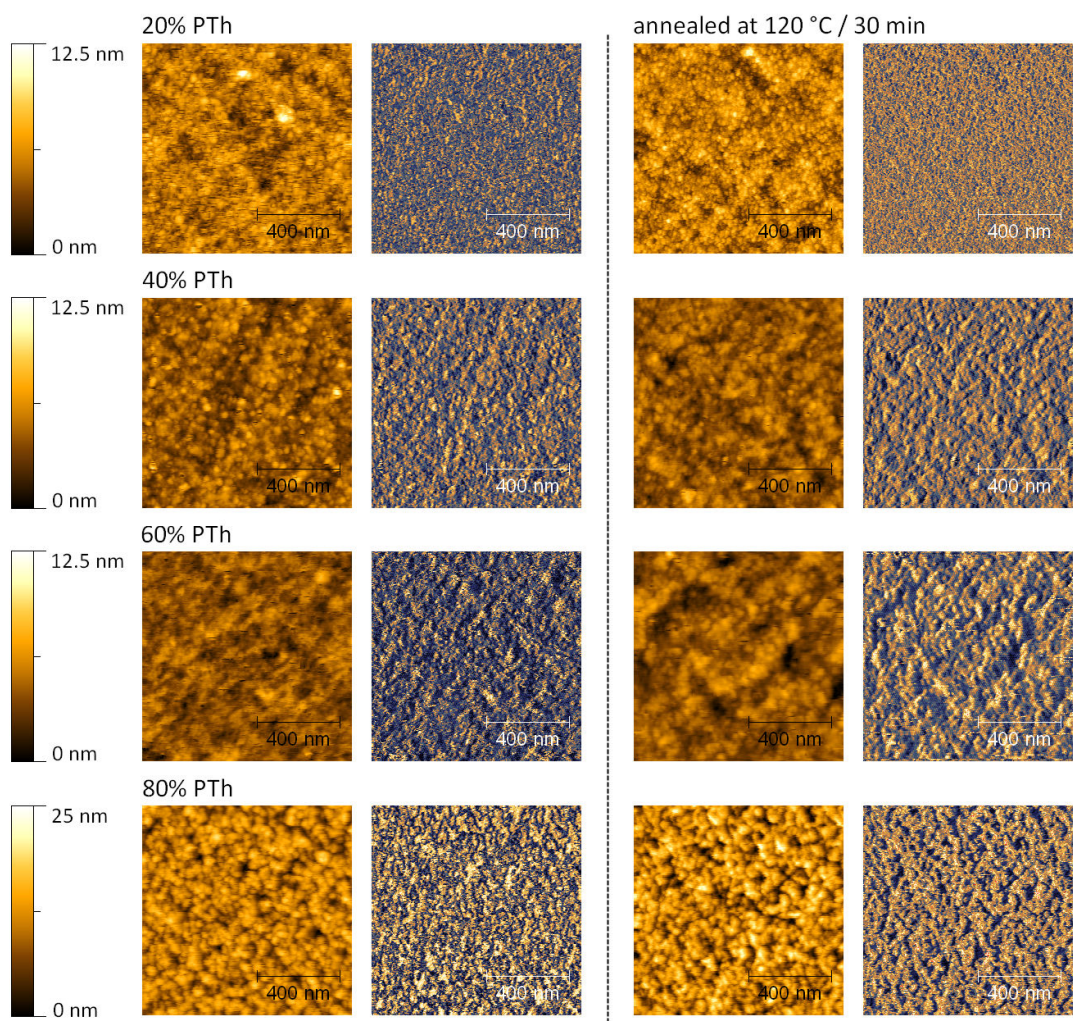


Figure 8. AFM topography (left) and phase (right) images of PTh:C₆₀ blends (with xy-scale of 1x1 μm and normalised phase scale for all images). Non-annealed films are left and annealed films right of the dotted line.

The trend of RMS roughness reaches minimum at the PTh composition between 40-60% (see Figure 9a). Overall values of less than 3.5 nm suggest a fine morphology in all blends. Even for large content of PTh (80%) the increase in roughness is only around 30%. This confirms that a moderate morphological development takes place in annealed vacuum-deposited blends similar to polymer-fullerene systems.

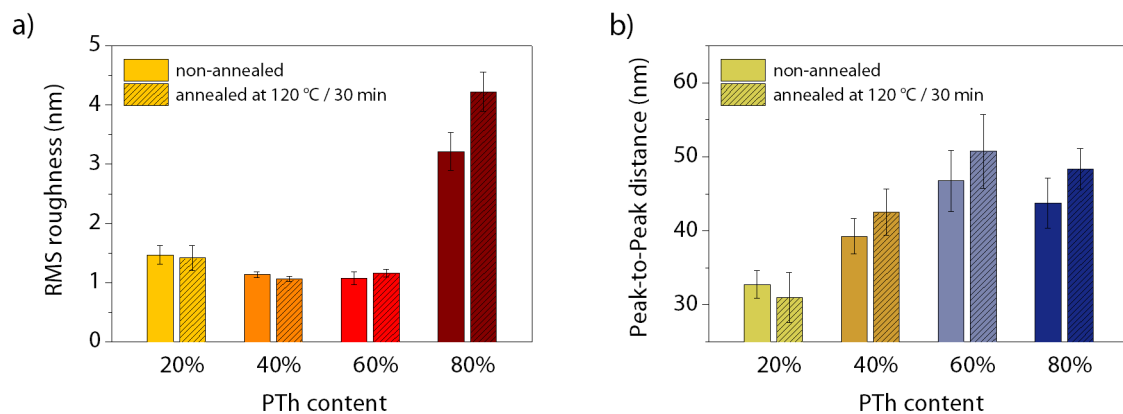


Figure 9. (a) RMS roughness of PTh:C₆₀ BHJ films before (single colour) and after (line pattern) thermal annealing. (b) Average peak-to-peak distance of the feature maxima in phase images.

The domains observed in the phase image of the PTh:C₆₀ blends range from an average size of ~30-35 nm at low PTh content to larger ~45-50 nm for 60% PTh. Moreover, there is a considerable development of the domain network upon annealing in all heterojunction films, as shown in Figure 8 and Figure 9b. For 40-80% PTh, the network coarsens which could suggest phase separation within the blends. This would be consistent with annealing-induced phase separation of polythiophene indicated by the XRD findings, and the photocurrent enhancement in BHJ devices (*section 5.3*).

5.6 Morphological comparison of polymer and oligomer BHJs

The response of the PTh:C₆₀ blend to post-annealing differs from that of the standard molecular systems^{13, 21, 49}. The distinctive combination of a longer chain polymer and a spherically symmetric fullerene might thus be critical in formation of an appropriate morphology as well as its further development upon annealing⁵⁰. Sakai *et al.* has shown¹⁴ that annealing of linear 6T/spherical C₇₀ blend (1:5) can lead to efficiency improvement.

However, the donor content was only 17% indicating that the charge transport and extraction in such system is based on a rather different morphology than that in PTh:C₆₀ with 20-80% PTh.

Nevertheless, due to the great similarity in molecular structure of PTh and 6T, a morphological study has been carried out to directly compare their behaviour in fullerene co-deposited blends. 6T:C₆₀ photovoltaic devices with the active-film parameters and performance similar to that reported by Sakai *et al.* were fabricated and their electronic and morphological response to post-annealing characterised. Despite significant efforts, no efficiency enhancement upon annealing was reproduced. *J-V* characteristics of a representative device (60 nm film thickness, ~17% 6T content, $J_{sc} = 3.94 \text{ mAcm}^{-2}$, $V_{oc} = 0.45 \text{ V}$, FF = 35.4% and PCE = 0.63%) before and after thermal treatment (at 140 °C for 20 min) are shown in Figure 10a. The reduction in V_{oc} upon annealing might be due to decreased R_{sh} resulting from unfavourable crystallisation of one of the phases.

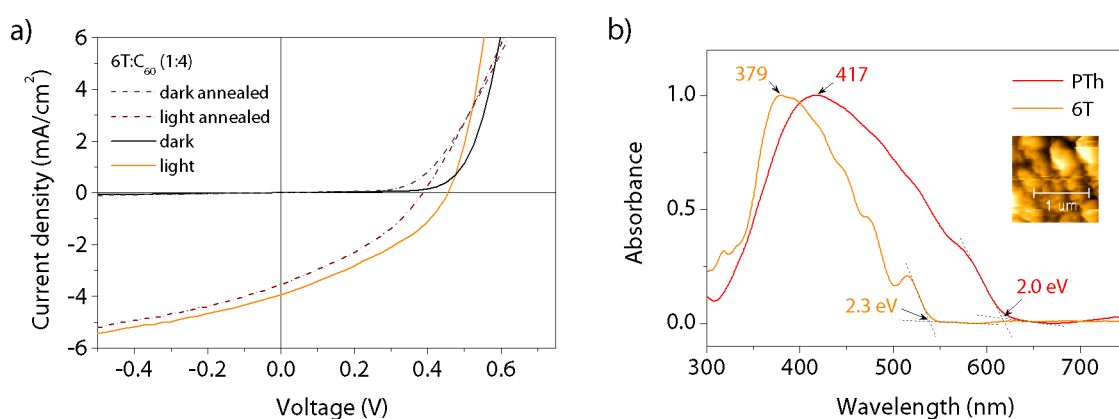


Figure 10. (a) Dark and light *J-V* characteristics of a 6T:C₆₀ device before (solid line) and after (dashed line) annealing (the inset shows AFM scan of the annealed 6T:C₆₀). (b) Normalised absorption spectra of single PTh (red) and 6T (orange) thin films (the inset shows AFM scan of the 6T film, z-scale on both insets is approximately 0-300 nm).

Although the 6T:C₆₀ device performance was comparable to PTh:C₆₀ (see *section 5.3*), there were several structural differences found between vacuum-deposited PTh and 6T. Figure 10b confirms that the band-gap of 6T (2.3 eV, in good agreement with the literature⁵¹) is substantially larger than the band-gap of PTh (2.0 eV) which arises from the much shorter conjugation length of the 6T oligomer in comparison to the PTh chain⁵². Numerous shoulders in the 6T spectrum indicate the high degree of crystallinity⁵³ in the oligomer film. This corresponds with the AFM surface scan, shown in the inset of Figure 10b, revealing high film roughness and a presence of large grains. Excessive fullerene content is thus required in the 6T:C₆₀ blends to prevent crystallisation and phase segregation of 6T.

The morphology of the oligothiophene- and polythiophene-fullerene systems was studied using XRD and AFM. The ratio of the blends was kept near their optimised device performance (i.e. ~17% 6T:C₆₀ and 50% PTh:C₆₀) and so were the annealing conditions. While development of the PTh:C₆₀ network upon annealing results from an interplay of the PTh and C₆₀ phases (for more detailed XRD analysis, see *section 5.5*), it is the C₆₀ phase which dominates the morphology in the 6T:C₆₀ blend, as shown in Figure 11 and Figure 12. Focusing on the 6T:C₆₀ system, the intensities of the main 111, 220 and 311 fullerene plane reflections⁴⁸ increase on annealing leaving only minimal evidence of the 6T crystals (near 19.5° and 28°^{54, 55}). This implies that agglomeration and crystallisation of C₆₀ takes place during the morphological development.

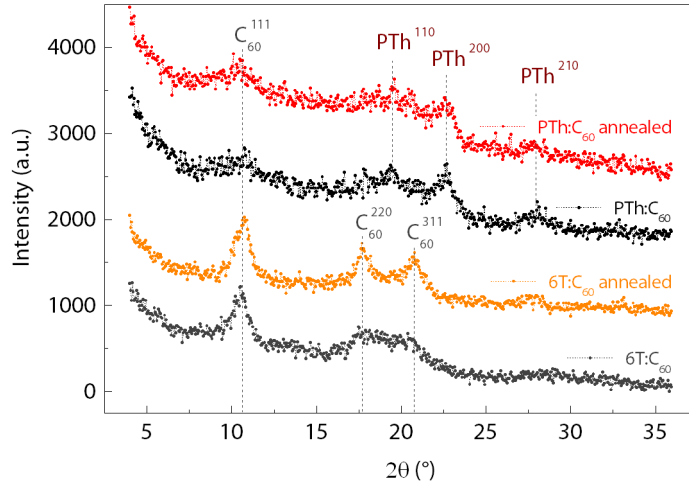


Figure 11. XRD traces of 20% 6T:C₆₀ blend before (grey) and after (orange) thermal annealing in comparison with 50% PTh:C₆₀ blend before (black) and after (red) thermal annealing. Dashed lines indicate position of the main PTh and C₆₀ diffraction peaks.

Surface topography of the films, represented by the AFM scans in Figure 12, shows large agglomerates present in the 6T:C₆₀ blend. In accordance with the XRD analysis, these are likely to be fullerene crystals⁵⁶ undergoing micro-scale phase segregation. The RMS roughness of the film is high (~25 nm) both before and after annealing (see Figure 12a). The thermal treatment reduces the number of agglomerates, however, their individual size increases. This is represented by higher kurtosis ('peakedness' of the height distribution) in Figure 12b. Similar phase behaviour might have resulted in deteriorated performance of the 6T:C₆₀ BHJ plotted in Figure 10a. In contrast to this development, Figure 12 shows that no such crystallisation is observed in the PTh:C₆₀ system. The films appear flat and the values of RMS roughness and kurtosis remain small after annealing.

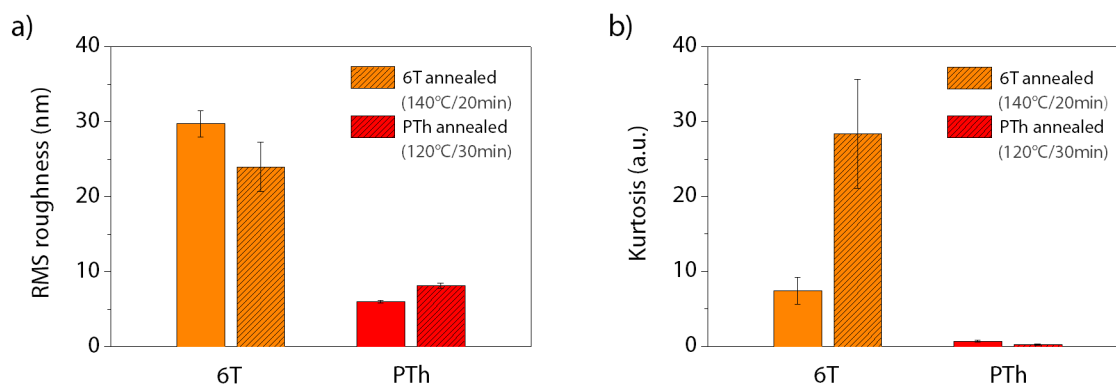
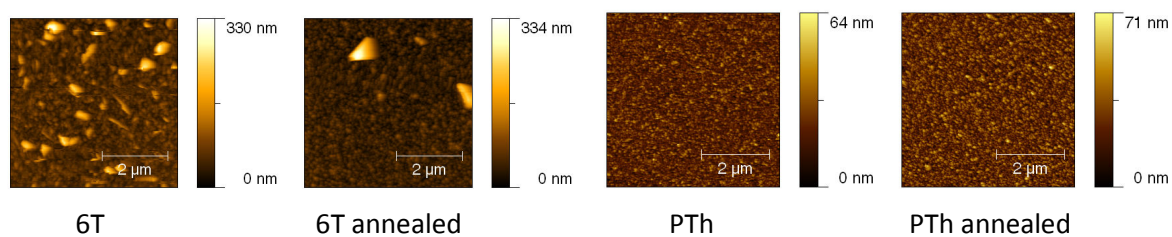


Figure 12. AFM scans of 6T- (top left two) and PTh-based (top right two) blends deposited on a silicon substrate (thickness ~ 150 nm). Images on left are before, and on right after thermal annealing. (a) RMS roughness and (b) kurtosis of the 6T:C₆₀ (orange) and PTh:C₆₀ (red) films. Patterned colour represents annealed samples.

These findings suggest that the annealing-induced morphology of the 20% 6T:C₆₀ blend consists of C₆₀ agglomerates partially intermixed with 6T crystals, all within an amorphous 6T:C₆₀ matrix. These phases must form a sufficient number of continuous percolated pathways in order to result in such efficient charge generation/extraction as seen in Sakai *et al.*'s work¹⁴ and Figure 10a. The longer-chain PTh exhibits a milder response to post-annealing, forming semi-crystalline nanoscale network with more balanced phase-separated phases and a finer morphology.

5.7 Multiple-layer BHJs as an equivalent to co-deposited BHJs

Bulk heterojunction films made by alternating deposition of very thin PTh and C₆₀ layers were fabricated. This alternating heterojunction (AHJ) concept, illustrated in Figure 13, has been shown to result in improved nanoscale morphology and thus enhanced J_{sc} , FF and PCE in comparison to standard co-deposited BHJ^{57, 58}. The effect of the sub-layer thickness was investigated in the 70 nm thick PTh:C₆₀ AHJ system, as shown in Figure 13. The thicknesses of the donor and acceptor sub-layers were kept equal while the overall number of sub-layers within the AHJ was varied from 8 to 28 (leading to thicknesses of 9, 5 and 2.5 nm for 8, 14 and 28 sub-layers respectively). The AHJs were further compared with a co-deposited 1:1 PTh:C₆₀ BHJ of the same thickness (70 nm).

Figure 13 shows that the multiple-layer approach indeed leads to performance superior to that of the standard BHJ. This is mostly a result of improved FF, which increases as much as 40% (5/5 nm sub-layers) compared to the blended 1:1 PTh:C₆₀. The PCE of the optimised AHJs (~0.6% for 2.5/2.5 nm sub-layers) is therefore significantly higher than that found in non-annealed BHJ devices (see *section 5.3*).

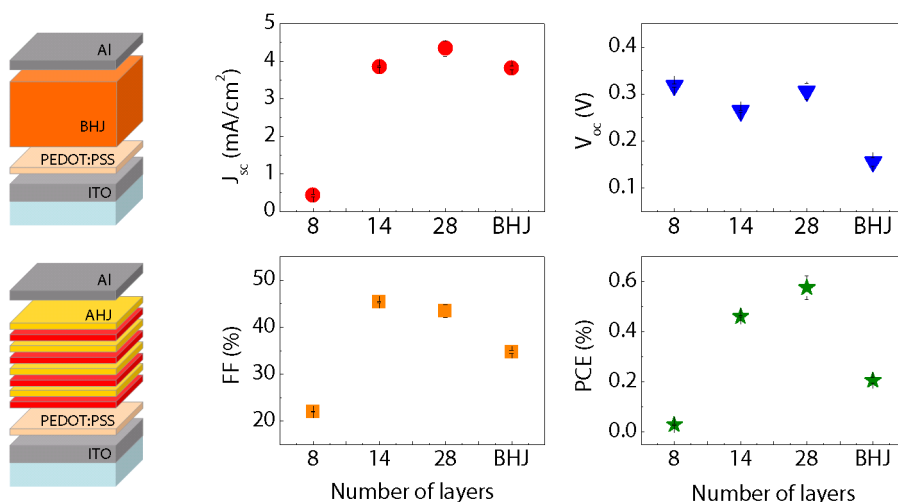


Figure 13. Illustration of BHJ (left top) and AHJ (left bottom) architectures. Summary of the main photovoltaic parameters of the AHJ devices with sub-layers of a different thickness.

The morphology of the AHJ is largely dependent on the thickness of the sub-layers forming the active layer. If the donor/acceptor sub-layers are too thick (e.g. 9 nm), they likely act as barriers for the transport of the minority charge carriers, resulting in high recombination and very low photocurrent (see Figure 13). However, thinner sub-layers (5 - 2.5 nm) appear to form a morphology which facilitates the transport of the majority carriers while allowing also a sufficient pathway for the minority carriers. This results in much lower recombination and thus higher FF. It is unclear at the moment, if the PTh:C₆₀ AHJ morphology consists of a stack of multiple continuous films thin enough for the charges to tunnel through⁵⁹, or of an interpenetrated network of dispersed island-type nanocrystals formed after the deposition of the individual sub-layers^{57, 60}. Further investigation would be needed to illuminate the relationship between performance and morphology.

5.8 Conclusions

Vacuum-deposited PTh:C₆₀ bulk heterojunctions with different donor-acceptor compositions were fabricated and the effect of post-production thermal annealing on their photovoltaic performance and morphology was studied. Co-deposition of blended mixtures was shown to yield 60% higher photocurrents than in thickness-optimised PTh/C₆₀ planar heterojunction counterparts. Furthermore, the post-production thermal annealing of the devices improved their power conversion efficiency by as much as 80%, achieving performance comparable to PTh:PCBM equivalents processed in solution from thermo-cleavable precursors.

Enhanced photoresponse was found to arise from favourable morphological development of PTh upon annealing. In contrast to small-molecule blends (here represented by the 6T:C₆₀ system), annealing-induced phase separation did not lead to formation of microcrystals but rather to an incremental improvement of the already established donor-acceptor network. As a result, the morphology control in PTh:C₆₀ bulk heterojunctions can be achieved over a wide range of compositions (20-80% PTh content).

5.9 References

1. Heliatek sets new world record efficiency of 10.7% for its organic tandem cell. <http://www.heliatek.com>
2. Green, M. A.; Emery, K.; Hishikawa, Y.; Warta, W.; Dunlop, E. D. *Progress in Photovoltaics* **2012**, 20, (1), 12-20.
3. Service, R. F. *Science* **2011**, 332, (6027), 293-293.

4. McNeill, C. R.; Greenham, N. C. *Advanced Materials* **2009**, 21, (38-39), 3840-3850.
5. Riede, M.; Uhrich, C.; Widmer, J.; Timmreck, R.; Wynands, D.; Schwartz, G.; Gnehr, W. M.; Hildebrandt, D.; Weiss, A.; Hwang, J.; Sundarraj, S.; Erk, P.; Pfeiffer, M.; Leo, K. *Advanced Functional Materials* **2011**, 21, (16), 3019-3028.
6. Bishop, C., *Vacuum Deposition Onto Webs, Films and Foils* William Andrew 2007; p 495
7. Krebs, F. C. *Solar Energy Materials and Solar Cells* **2009**, 93, (4), 394-412.
8. Park, S. H.; Roy, A.; Beaupre, S.; Cho, S.; Coates, N.; Moon, J. S.; Moses, D.; Leclerc, M.; Lee, K.; Heeger, A. J. *Nature Photonics* **2009**, 3, (5), 297-U5.
9. Brabec, C. J.; Gowrisanker, S.; Halls, J. J. M.; Laird, D.; Jia, S. J.; Williams, S. P. *Advanced Materials* **2010**, 22, (34), 3839-3856.
10. Yang, X.; Loos, J. *Macromolecules* **2007**, 40, (5), 1353-1362.
11. Pfuetzner, S.; Meiss, J.; Petrich, A.; Riede, M.; Leo, K. *Applied Physics Letters* **2009**, 94, (25), -.
12. Wynands, D.; Levichkova, M.; Leo, K.; Uhrich, C.; Schwartz, G.; Hildebrandt, D.; Pfeiffer, M.; Riede, M. *Applied Physics Letters* **2010**, 97, (7).
13. Peumans, P.; Uchida, S.; Forrest, S. R. *Nature* **2003**, 425, (6954), 158-162.
14. Sakai, J.; Taima, T.; Yamanari, T.; Saito, K. *Solar Energy Materials and Solar Cells* **2009**, 93, (6-7), 1149-1153.
15. Kaji, T.; Zhang, M. L.; Nakao, S.; Iketaki, K.; Yokoyama, K.; Tang, C. W.; Hiramoto, M. *Advanced Materials* **2011**, 23, (29), 3320-+.
16. Heutz, S.; Sullivan, P.; Sanderson, B. M.; Schultes, S. M.; Jones, T. S. *Solar Energy Materials and Solar Cells* **2004**, 83, (2-3), 229-245.
17. Pandey, R.; Holmes, R. J. *Advanced Materials* **2010**, 22, (46), 5301-5305.
18. Rand, B. P.; Genoe, J.; Heremans, P.; Poortmans, J. *Progress in Photovoltaics* **2007**, 15, (8), 659-676.
19. Dittmer, J. J.; Lazzaroni, R.; Leclere, P.; Moretti, P.; Granstrom, M.; Petritsch, K.; Marseglia, E. A.; Friend, R. H.; Bredas, J. L.; Rost, H.; Holmes, A. B. *Solar Energy Materials and Solar Cells* **2000**, 61, (1), 53-61.
20. Lee, J. U.; Kim, Y. D.; Jo, J. W.; Kim, J. P.; Jo, W. H. *Journal of Materials Chemistry* **2011**, 21, (43).
21. Uchida, S.; Xue, J. G.; Rand, B. P.; Forrest, S. R. *Applied Physics Letters* **2004**, 84, (21), 4218-4220.
22. Peumans, P.; Yakimov, A.; Forrest, S. R. *Journal of Applied Physics* **2003**, 93, (7), 3693-3723.
23. Steinberger, S.; Mishra, A.; Reinold, E.; Levichkov, J.; Uhrich, C.; Pfeiffer, M.; Bauerle, P. *Chemical Communications* **2011**, 47, (7), 1982-1984.
24. Hiramoto, M.; Fukusumi, H.; Yokoyama, M. *Applied Physics Letters* **1992**, 61, (21), 2580-2582.
25. Chen, S. A.; Ni, J. M. *Macromolecules* **1992**, 25, (23), 6081-6089.
26. Lilliu, S.; Agostinelli, T.; Pires, E.; Hampton, M.; Nelson, J.; Macdonald, J. E. *Macromolecules* **2011**, 44, (8), 2725-2734.

27. Xue, J. G.; Rand, B. P.; Uchida, S.; Forrest, S. R. *Journal of Applied Physics* **2005**, 98, (12).
28. Chirvase, D.; Parisi, J.; Hummelen, J. C.; Dyakonov, V. *Nanotechnology* **2004**, 15, (9), 1317-1323.
29. Mihailetchi, V. D.; Koster, L. J. A.; Blom, P. W. M.; Melzer, C.; de Boer, B.; van Duren, J. K. J.; Janssen, R. A. J. *Advanced Functional Materials* **2005**, 15, (5), 795-801.
30. Scharber, M. C.; Wuhlbacher, D.; Koppe, M.; Denk, P.; Waldauf, C.; Heeger, A. J.; Brabec, C. L. *Advanced Materials* **2006**, 18, (6), 789-+.
31. Mihailetchi, V. D.; Blom, P. W. M.; Hummelen, J. C.; Rispens, M. T. *Journal of Applied Physics* **2003**, 94, (10), 6849-6854.
32. van Bavel, S. S.; Barenklau, M.; de With, G.; Hoppe, H.; Loos, J. *Advanced Functional Materials* **2010**, 20, (9), 1458-1463.
33. Sakai, J.; Taima, T.; Saito, K. *Organic Electronics* **2008**, 9, (5), 582-590.
34. Mayer, A. C.; Lloyd, M. T.; Herman, D. J.; Kasen, T. G.; Malliaras, G. G. *Applied Physics Letters* **2004**, 85, (25), 6272-6274.
35. Lee, C. K.; Pao, C. W.; Chu, C. W. *Energy & Environmental Science* **2011**, 4, (10), 4124-4132.
36. Gevorgyan, S. A.; Krebs, F. C. *Chemistry of Materials* **2008**, 20, (13), 4386-4390.
37. Dang, M. T.; Hirsch, L.; Wantz, G. *Advanced Materials* **2011**, 23, (31), 3597-3602.
38. Mihailetchi, V. D.; Wildeman, J.; Blom, P. W. M. *Physical Review Letters* **2005**, 94, (12).
39. Koster, L. J. A.; Kemerink, M.; Wienk, M. M.; Maturova, K.; Janssen, R. A. J. *Advanced Materials* **2011**, 23, (14), 1670-+.
40. Kim, J. Y.; Kim, S. H.; Lee, H. H.; Lee, K.; Ma, W. L.; Gong, X.; Heeger, A. J. *Advanced Materials* **2006**, 18, (5), 572-+.
41. Chu, C. W.; Yang, H. C.; Hou, W. J.; Huang, J. S.; Li, G.; Yang, Y. *Applied Physics Letters* **2008**, 92, (10).
42. Chen, F. C.; Ko, C. J.; Wu, J. L.; Chen, W. C. *Solar Energy Materials and Solar Cells* **2010**, 94, (12), 2426-2430.
43. Liang, C. W.; Su, W. F.; Wang, L. *Applied Physics Letters* **2009**, 95, (21).
44. Dennler, G.; Scharber, M. C.; Brabec, C. J. *Advanced Materials* **2009**, 21, (13), 1323-1338.
45. Mihailetchi, V. D.; Xie, H. X.; de Boer, B.; Koster, L. J. A.; Blom, P. W. M. *Advanced Functional Materials* **2006**, 16, (5), 699-708.
46. Mo, Z.; Lee, K. B.; Moon, Y. B.; Kobayashi, M.; Heeger, A. J.; Wudl, F. *Macromolecules* **1985**, 18, (10), 1972-1977.
47. Hermet, P.; Bantignies, J. L.; Almairac, R.; Sauvajol, J. L.; Serein, F.; Lere-Porte, J. P. *Journal of Physical Chemistry B* **2008**, 112, (40), 12662-12665.
48. Gong, J. L.; Ma, G. B.; Chen, G. H. *Journal of Materials Research* **1996**, 11, (8), 2071-2075.
49. Wei, G. D.; Lunt, R. R.; Sun, K.; Wang, S. Y.; Thompson, M. E.; Forrest, S. R. *Nano Letters* **2010**, 10, (9), 3555-3559.

50. Xue, J. G.; Rand, B. P.; Uchida, S.; Forrest, S. R. *Advanced Materials* **2005**, 17, (1), 66-+.
51. Pellegrino, O.; Vilar, M. R.; Horowitz, G.; Kouki, F.; Garnier, F.; da Silva, J. D. L.; do Rego, A. M. B. *Thin Solid Films* **1998**, 327, 291-294.
52. Salzner, U.; Lagowski, J. B.; Pickup, P. G.; Poirier, R. A. *Synthetic Metals* **1998**, 96, (3), 177-189.
53. Fichou, D.; Teulade-Fichou, M. P.; Horowitz, G.; Demanze, F. *Advanced Materials* **1997**, 9, (1), 75.
54. Servet, B.; Ries, S.; Trotel, M.; Alnot, P.; Horowitz, G.; Garneir, F. *Advanced Materials* **1993**, 5, (6), 461-464.
55. Garnier, F.; Yassar, A.; Hajlaoui, R.; Horowitz, G.; Deloffre, F.; Servet, B.; Ries, S.; Alnot, P. *Journal of the American Chemical Society* **1993**, 115, (19), 8716-8721.
56. Kozub, D. R.; Vakhshouri, K.; Orme, L. M.; Wang, C.; Hexemer, A.; Gomez, E. D. *Macromolecules* **2011**, 44, (14), 5722-5726.
57. Yang, F.; Sun, K.; Forrest, S. R. *Advanced Materials* **2007**, 19, (23), 4166-+.
58. Hong, Z. R.; Maennig, B.; Lessmann, R.; Pfeiffer, M.; Leo, K.; Simon, P. *Applied Physics Letters* **2007**, 90, (20).
59. Sakai, J.; Taima, T.; Yamanari, T.; Yoshida, Y.; Fujii, A.; Ozaki, M. *Japanese Journal of Applied Physics* **2010**, 49, (3).
60. Kim, J. W.; Kim, H. J.; Lee, H. H.; Kim, T.; Kim, J. J. *Advanced Functional Materials* **2011**, 21, (11), 2067-2071.

CONCLUSIONS

This work has demonstrated vacuum thermal deposition of conjugated polymers for organic photovoltaics. Poly(3-hexylthiophene) (P3HT) and poly(thiophene) (PTh) semiconducting polymers with and without side groups were investigated. Structural studies of the polymers before and after evaporation showed that while the chemical structure is largely retained, their molecular weight decreases as a result of thermal heating. Additionally, cleavage of alkyl side groups from the conjugated backbone takes place in P3HT. Due to the lack of side groups, a higher degree of conjugation can be obtained for evaporated PTh which presents suitability of the method for the deposition of low solubility polymers.

The study has shown that polymer side groups have a strong influence on molecular packing and charge extraction in vacuum-deposited polymer thin films. Unlike P3HT, evaporated PTh forms highly crystalline films as illustrated in Figure 1. This results in enhanced charge transport properties with hole mobility two orders of magnitude higher ($10^{-4} \text{ cm}^2\text{V}^{-1}\text{s}^{-1}$) than that in P3HT. The effect of molecular order was demonstrated on polymer/fullerene planar heterojunction solar cells. PTh-based devices have significantly better current and recombination characteristics, leading to improved overall PCE by 70% as compared to P3HT.

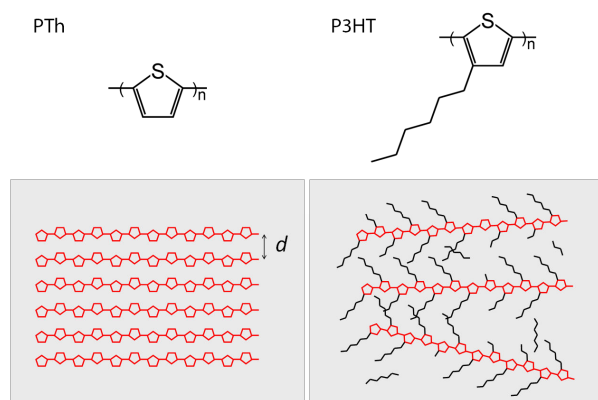


Figure 1. Molecular structure of P3HT and PTh with a simple model of their molecular packing. PTh chains are more ordered than P3HT mainly due to the lack of side groups.

This showed that the chemical structure of the molecule is a crucial parameter in vacuum-deposition of large organic semiconductors. The method is compatible with roll-to-roll processes and thus has good potential for low-cost production of highly ordered polymer thin films relevant to a plethora of electronic and optoelectronic applications.

Finally, vacuum-deposited PTh:C₆₀ bulk heterojunctions with different donor-acceptor compositions were fabricated and the effect of post-production thermal annealing on their photovoltaic performance and morphology was studied. Co-deposition of blended mixtures led to 60% higher photocurrents than in thickness-optimized PTh/C₆₀ planar heterojunction counterparts. Furthermore, by annealing the devices post-situ the PCE was improved by as much as 80%, achieving performance comparable to PTh:PCBM equivalents processed in solution from thermo-cleavable precursors (~0.7%).

The enhanced photo-response is a result of favourable morphological development of PTh upon annealing. In contrast to small-molecule blends, annealing-induced phase separation does not lead to formation of microcrystals but rather to an incremental improvement of the already established donor-acceptor network, as shown in Figure 2. More appropriate

phase-separation behaviour might be achieved by co-depositing less miscible materials, such as a polymeric acceptor with the polymeric donor. Polymer-polymer blends may produce preferable morphology with more continuous phase domains and well-balanced charge carrier mobilities. Study of the phase behaviour of PTh and other acceptors would inform such materials selection.

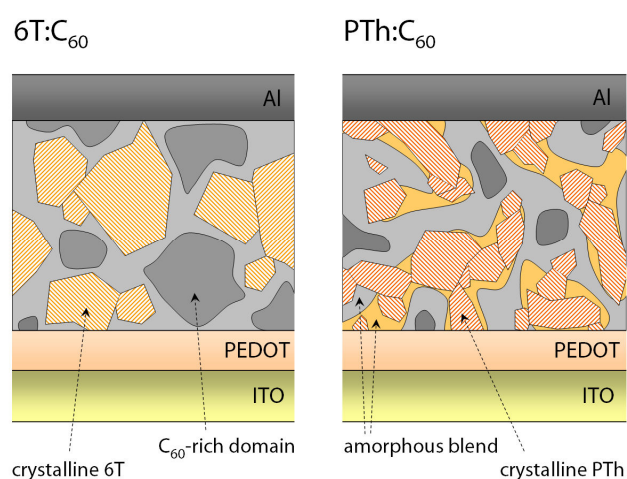


Figure 2. Morphological comparison of oligomer and polymer bulk heterojunction systems.

In summary, the photovoltaic response of the devices underlines the potential to fabricate complex multilayered structures with enhanced performance. The deposition method allows manipulation of horizontal as well as vertical donor-acceptor blend composition, achieving morphology control difficult to realize by the use of solvents. As an example, a device architecture consisting of multiple alternating PTh/C₆₀ thin films was presented here with performance exceeding that of its equivalent co-deposited bulk heterojunction. Further improvements can be made by introducing gradient compositions or sandwiching the blend between the donor and the acceptor layers in form of a *p-i-n* junction.

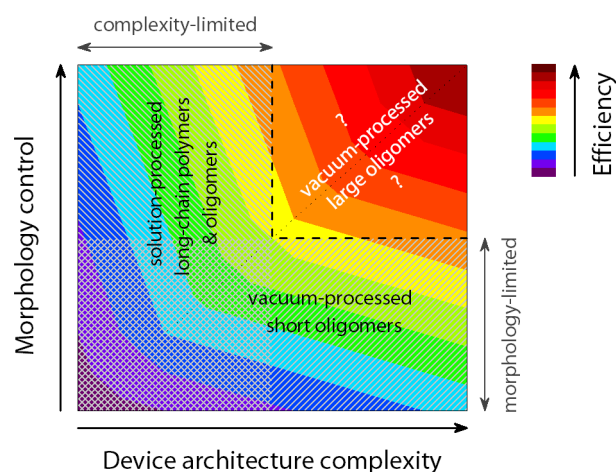


Figure 3. The two potential ways of improving device efficiency - morphology of the active layer and complexity of the device architecture. The patterned areas represent confinement of small molecules (bottom quadrangles) and long-chain polymers (left quadrangles). Suggested is a position of vacuum-processed large oligomers (upper right quadrangle).

Vacuum thermal deposition of conjugated polymers could be a promising alternative to coating and printing methods, however, further work needs to be done especially in the area of synthesising the best vacuum-processable polymers (e.g. with the right M_w , and energy levels for improved E_g and V_{oc}). Figure 3 highlights the role of the morphology control and device architecture complexity in improving efficiency of organic solar cells. To date only vacuum-deposited oligomers, with only a few repeating monomeric units, and solution-processed long-chain polymers, typically consisting of hundreds of monomers, have been investigated. They are limited to reaching high-efficiencies by control over the active layer morphology and complexity of the device architecture, respectively. Low molecular weight polymers or large oligomers with a linear quasi long-chain character and vacuum-processing advantages have the potential to combine both these elements and drive organic photovoltaic efficiencies up.

FUTURE WORK

- Synthesise polymers with shorter conjugation length and study their decomposition due to thermal heating. Estimate the “optimal” polymer size for vacuum thermal evaporation method and see if the lower amount of impurities has an influence on charge transport.
- Study diffusion of C₆₀ into PTh during annealing of planar heterojunction devices. Identify whether post-annealing leads to formation and interpenetration of PTh and C₆₀ crystals, or diffusion of C₆₀ between the PTh domains. Find optimal annealing parameters and compare the devices with co-evaporated bulk heterojunctions.
- Employ TEM imaging to study morphology in co-evaporated BHJs, analyse extent of crystallisation/phase separation and identify individual phases within the system. Look at the in-situ development of morphology during annealing.
- Apply in-situ thermal annealing and compare the results with post-annealing treatment.
- Investigate morphological development in PTh:C₆₀ blends as a function of the polymer conjugation length. Study relationship between polymer size and phase separation.
- Fabricate co-deposited polymer:polymer bulk heterojunction and study morphology of such system. Look if better morphology control can be achieved than in PTh:C₆₀ BHJs.
- Determine the phase morphology in alternating bulk heterojunctions (e.g. by cross-section TEM). Study parameters determining the bulk morphology, such as thickness of the individual thin films or post-production thermal annealing.
- Substitute spin-cast PEDOT:PSS for vacuum-deposited MoO₃. Apply additional interface layers (e.g. BCP) to improve device performance. Proceed to more advanced device architectures, such as *p-i-n* or tandem cells, to illustrate benefits of vacuum deposition.